Measurement of Differential Cross Section of $^{12}C(d,p)$ Reaction at E_d = 160 to 300 keV

by

Abdul Aziz Mohammed Al-Jalal

A Thesis Presented to the

FACULTY OF THE COLLEGE OF GRADUATE STUDIES

KING FAHD UNIVERSITY OF PETROLEUM & MINERALS

DHAHRAN, SAUDI ARABIA

In Partial Fulfillment of the
Requirements for the Degree of

MASTER OF SCIENCE

In

PHYSICS

August, 1991

Order Number 1354108

Measurement of differential cross section of $^{12}C(d,p)$ reaction at E_d = 160 to 300 keV

Al-Jalal, Abdul Aziz Mohammed, M.S.

King Fahd University of Petroleum and Minerals (Saudi Arabia), 1991

U·M·I
300 N. Zeeb Rd.
Ann Arbor, MI 48106

MEASUREMENT OF DIFFERENTIAL CROSS SECTION OF $^{12}C(d,p)$ REACTION AT E_d = 160 TO 300 keV

BY

ABDUL AZIZ MOHAMMED AL-JALAL

A Thesis Presented to the

FACULTY OF THE COLLEGE OF GRADUATE STUDIES

KING FAHD UNIVERSITY OF PETROLEUM & MINERALS

DHAHRAN, SAUDI ARABIA

In Partial Fulfillment of the
Requirements for the Degree of

MASTER OF SCIENCE

In

PHYSICS

AUGUST 1991

KING FAHD UNIVERSITY OF PETROLEUM AND MINERALS
DHAHRAN 31261, SAUDI ARABIA

COLLEGE OF GRADUATE STUDIES

This thesis, written by ***ABDUL AZIZ MOHAMMED AL-JALAL*** under the direction of his Thesis Advisor and approved by his Thesis Committee, has been presented to and accepted by the Dean of the College of Graduate Studies, in partial fulfillment of the requirements for the degree of ***MASTER OF SCIENCE*** in ***PHYSICS***.

THESIS COMMITTEE

Dr. H. A. Al-Juwair (Thesis Advisor)

Dr. A. Al Naqvi (Thesis Co-Advisor)

Dr. H. A. Mavromatis (Member)

Department Chairman

Dean, College of Graduate Studies

TO MY MOTHER
AND TO THE MEMORY
OF MY FATHER

ACKNOWLEDGMENT

I would like to acknowledge King Fahd University of Petroleum and Minerals for its support of this research.

Special thanks are due to the Physics Department and the Energy Research Laboratory for making all their facilities available to me.

I would like to express my gratefulness to all my thesis committee members : Dr.Hussain Al-Juwair, Dr.Akhtar Naqvi and Prof. Harry Mavromatis for their kind support and precious remarks. In particular, I would like to express my deep appreciation to Dr.Akhtar Naqvi, my thesis co-advisor, who spent a lot of his valuable time helping me preparing the experimental setup, collecting and analyzing the experimental data. I will be always in his debt.

Also, I like extend my appreciation to Mr. Muhammid Raashid for operating the accelerator, to Dr. Ali Coban and Dr. Fatah Khiari for their assistance in some stages of the experiment and to Mr. Mohammed Daous and Mr. Majed Al-Ashram for their valuable discussions.

Finally, I would like to sincerely thank all the members of my family for their valuable supports, in particular, to my dear wife whose constant encouragement made the completion of this work possible.

ملخص الرسالة

اسم الطالب : عبد العزيز بن محمد الجلال

عنوان الرسالة : قياس المقطع العرضي التفاضلي للتفاعل $^{12}C(d,p)$ لطاقات الديوتيرون بين ١٦٠ و ٣٠٠ كيلو إلكترون ڤولت

التخصص : فيزياء

تاريخ الرسالة : محرم ١٤١٢ هـ

لقد تم قياس المقطع العرضي التفاضلي المطلق للتفاعل $^{12}C(d,p)$ للطاقات الديوتيرون ٢٠٠ و٢٢٠ و ٢٥٠ و ٢٨٠ و ٣٠٠ كيلو إلكترون ڤولت عند زوايا التفاعل بين ٢٥ و ١٦٠ درجة كل ١٠ درجات . و كذلك تم قياس علاقة الإثارة للتفاعل نفسه عند زوايا التفاعل ٢٥ و ٣٥ و ٩٠ و ١٤٠ درجة لطاقات الديوتيرون بين ١٦٠ و ٣٠٠ كيلو إلكترون ڤولت كل ١٠ كيلو إلكترون ڤولت . لقد قيست المقاطع العرضية بدقة ٥ ٪ . لوحظ أن علاقة الإثارة تزداد بسلاسة و باضطراد مع زيادة طاقة الديوتيرون وأن التوزيع الزاوي يعلو في الزوايا الخلفية . يمكن أن نستنتج من هذه النتائج أن التفاعل تم عن طريق قناة النزع للتفاعل المباشر .

لقد صممت و صنعت غرفة التفاعل كجزء من هذا البحث . هذه الغرفة يمكن استخدامها كذلك كجهاز لقياس استقطاب شعاع الديوتيرون .

درجة الماجستير في العلوم

جامعة الملك فهد للبترول و المعادن

الظهران – المملكة العربية السعودية

محرم ١٤١٢هـ

ABSTRACT

Title : **DIFFERENTIAL CROSS SECTION MEASUREMENT OF $^{12}C(d,p)$ REACTION AT E_d = 160 - 300 keV**

By : **ABDUL AZIZ MOHAMMED AL-JALAL**

Major : **PHYSICS**

Date : **AUGUST 1991**

Absolute differential cross sections of $^{12}C(d,p)$ reaction were measured at E_d = 200, 220, 250, 280 and 300 keV for reaction angles between 25 and 160 degrees in steps of 10 degrees. Also excitation functions for the same reaction were measured at 25, 35, 90 and 140 degrees for deuteron energies between 160 and 300 keV in steps of 10 keV. The cross sections were measured with 5% uncertainty. It was noticed that the excitation functions increase smoothly with the deuteron energy and the angular distribution peaked backward. One may conclude from these trends that the reaction proceeds through stripping channel of direct reaction mechanism.

A scattering chamber was designed and fabricated as a part of this project. The chamber can be used also as a deuteron beam polarimeter.

MASTER OF SCIENCE

KING FAHD UNIVERSITY OF PETROLEUM AND MINERALS

DHAHRAN 21361, SAUDI ARABIA

TABLE OF CONTENTS

LIST OF FIGURES

Figure

Figure

Figure

Figure

LIST OF TABLES

Table

Table

LIST OF NOTATIONS

^{12}C	Carbon 12.
d or D	Deuteron.
p	Proton.
E_d	Deuteron lab energy.
E_p	Proton lab energy.
γ	Gamma ray.
ℓ	Angular momentum of a nuclear state.
DWBA	Distored Wave Born Approximation.
ERL	Energy Research Laboratory.
KFUPM	King Fahd University of Petroluem and Minerals.
mster	millisteradian.
ΔE	Total Energy loss.
x	Depth in a material.
$\frac{dE}{dx}$	Specific energy loss.
Trim-87	Software to calculate specific energy loss.
SSB detector	Semiconductor Surface Barreir Detector.

SCA	Signal Channel Analyser.
ADC	Analog to Digital Convertor.
MBD	Microprogrammable Branch Driver.
XSYS	Software which aquires and analizes data.
DAP	Data aquizition program.
EVL	Event analysis language.
COM	File containing executable commands.
$Y(E, \theta, i)$	Yield at reaction angle θ with incident deuteron energy E and run number i.
$C(E, \theta, i)$	Carbon buildup corrected yield at reaction angle θ with incident deuteron energy E and run number i.
R(i-1)	Carbon buildup correction factor for run i.
$C_A(E, \theta, ij)$	Adjusted yield, at reaction angle θ with incident deuteron energy E and run number i, using run j.
$C_{AC}(E, \theta, ij)$	Adjusted and corrected carbon buildup yield, at reaction angle θ with incident deuteron energy E and run number i, using run j.
$\frac{d\sigma(E,\theta)}{d\Omega}$	Differential cross section at reaction angle θ at incident deuteron energy E .
I	Total number of incident particles.
n t	number of target nuclei per unit area.

$\Delta\Omega$	solid angle suspended by the detector.
$\Delta C(E, \phi, i)$	Statistical erorr in $C(E, \phi, i)$.
$\Delta C_{AC}(E, \theta, ij)$	Statistical erorr in $C_{AC}(E, \theta, ij)$.
σ_m	Standard deviation of four fresh target yields.
σ_{sys}	Systematic erorr due to charge integration and target thickness.
σ_{stat}	Statistical error in the average of four fresh target yields.

CHAPTER 1

INTRODUCTION

The differential cross sections of $^{12}C(d,p)$ reaction were measured at deuteron energies between 160 and 300 keV. As a part of this project, a scattering chamber was designed and fabricated at Energy Research Lab (ERL). This chamber is a part of charge particle spectroscopy setup. While designing this chamber, provisions were also incorporated to use it as a beam polarimeter.

In this chapter, gross features of the nuclear reactions will be highlighted. Then, (d,p) reaction will be discussed and a model,which can explain the shape of angular distribution of (d,p) reaction, will be described briefly. Finally, the present status of low energy data of $^{12}C(d,p)$ reaction will be reviewed.

1.1 Compound and Direct Nuclear Reactions

Nuclear reactions may be divided into two broad categories, compound nucleus reaction and direct reaction. In compound nucleus reaction, a highly excited system is formed whose life is long enough for its excitation energy to be shared by all its constituent nucleons. The compound nucleus decays by emitting one or more nucleon such that its decay mode is

independent of the mode of formation.[1] The other extreme case is the direct reaction in which target and projectile make a glancing contact and immediately separate. In this type, only a few degrees of freedom of many body system are excited whereas other degrees of freedom remain effectively passive.[2]

Direct as well as compound nucleus may contribute to a given reaction. Their relative contribution depends upon the reaction energy. At the lowest energies the compound nucleus dominates while at the energies above 10 MeV the reaction proceed through direct mechanism. The direct reactions and the compound nucleus reactions are the extreme cases. The intermediate processes falling between these extremes are called pre-equilibrium reaction.[3]

Compound nucleus reactions and direct reactions can be identified from their own characteristic angular distributions. Compound nucleus angular distribution shows backward and forward symmetry about 90 degree which results from the correlation of angular momentum in the entrance and in the exit channel of the reaction. On the other hand, in direct reactions, the angular distribution are strongly forward peaked because the projectile continues to move forward after making glancing collision with the target. Excitation functions may also be used to identify the nuclear process involved. For compound nucleus formation the excitation function shows sharp resonances.[4]

There are three important types of direct reactions, inelastic scattering, stripping/pick-up reaction and knock-out reaction. In the inelastic scattering, projectile or target or both may be excited by the glancing contact whereas in stripping/pick-up reaction (also called transfer reaction) one or few nucleons may be exchanged between the projectile and the target. In knock-out reactions, the projectile knocks out one or more nucleons from the target. In the final phase of knock-out reaction, the projectile, the knocked-out nucleon and the residual target continue to move freely. This reaction is also called quasi-free scattering.[3]

1.2 (d,p) Reaction

The (d,p) reaction is the simplest reaction among the transfer reactions whuch involves the transfer of one nucleon. The energy distribution of the proton from (d,p) reaction is characteristic of the nuclear process involved - a direct reaction or compound reaction. Fig. 1.1 shows energy distribution of proton in (d,p) reaction. The figure shows a continuous energy distribution at the lower energy of the spectrum. If the corresponding angular distributions of these protons are almost isotropic and symmetric about 90 degree, then these protons are due to compound nucleus process. The more energetic protons which have discrete energies do not show symmetry about 90 degree and often have angular distribution peaking in forward direction at high energy and in backward direction at low energies of incident deuterons. These protons are from stripping reaction in which the neutron from the incident target is captured by the target leaving the

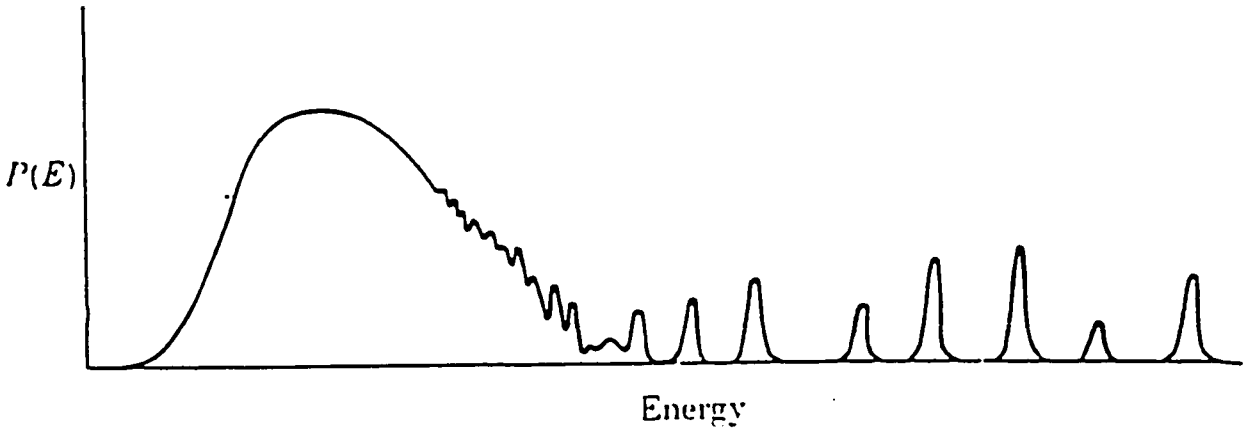

7926

Fig. 1.1. Energy Distribution of protons from (d,p) reaction.

proton to go on alone. Fig. 1.2 shows the deuteron stripping at high and low energy. Oppenheimer and Phillips[5] had explained the backward peaking of angular distribution of (d,p) reaction at low energy. According to them, only those deuterons with very small impact parameters penetrate far enough through the coulomb field. The neutron is detached from the deuteron and is captured by the nucleus while the remaining proton is then repelled back in the direction from which they came. Therefore the repelled proton has backward peaking. This is clearly shown in fig. 1.2. As the energy increases the repelled proton will continue moving in the forward direction while detached neutron is captured by the nucleus. This explains the forward peaking of angular distribution of emitted protons. It is also possible for the deuteron to be broken up without capture. Therefore the continuous distribution of energy in fig. 1.2 at low energy is due to protons emitted from the compound nucleus or from the deuteron break-up while the discrete peak at higher energies corresponds to protons emitted in a stripping reaction. Each discrete peak in the proton energy spectrum corresponds to a reaction in which the residual nucleus is left in its ground or in one of its excited states. The reaction may be thought of as a deuteron depositing its neutron in one of the states of the residual nucleus leaving the proton to go on alone, as shown in fig. 1.3. The angular distribution of the emitted protons in a particular (d,p) reaction is a characteristic of the state to which the neutron is captured. Hence the reaction can be used to determine some of the properties of the nuclear state.[4]

Knock-out reaction and heavy-particle stripping also contribute

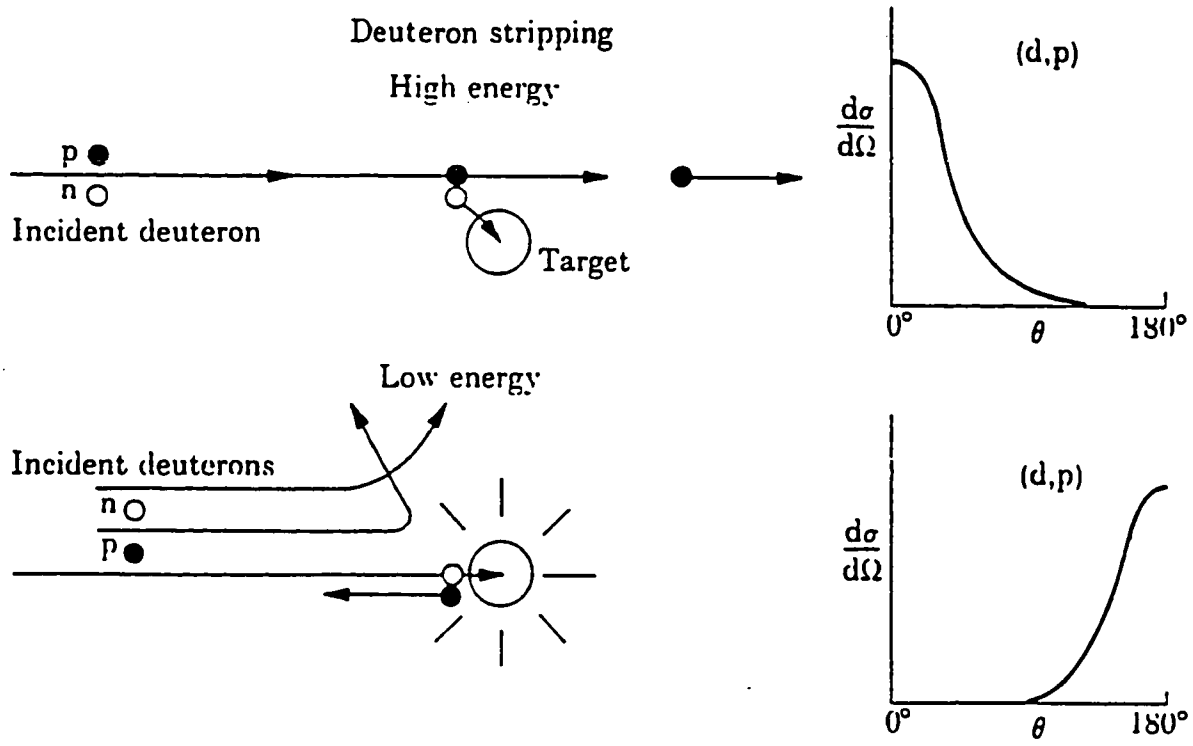

Fig. 1.2. Deuteron stripping at high and low energy.

towards (d,p) reaction. In a knock-out reaction, the incident deuteron nuclear. In heavy-particle stripping process, which is best pictured in the center of mass system, an incident deuteron and target nucleus approach each other till the deuteron coalesces with the target, except for one proton in the target, forming a residual nucleus moving in the direction of incident deuteron. The remaining proton continues in its original direction of motion and thus is emitted in backward direction. Backward peaking is particularly associated with heavy-ion stripping but there are other reaction which may contribute to backward peaking. Fig. 1.4 shows the Feynman diagrams for dominant (d,p) reaction mechanisms.[4]

Butler[6] had suggested that the forward peaked angular distribution of (d,p) reaction can be fitted by the square of the spherical Bessel function of order ℓ, where ℓ is the angular momentum of the state in which neutron (in case of (d,p) reaction) or proton (for the (d,n) reaction) is captured. In the early development stages of (d,p) theory, the reaction mechanism was treated using a plane wave approximation. This approximation did not described the process accurately. Later on, it was realized that the incident wave was indeed distorted by the nuclear interaction. This led to the development of direct nuclear theory based upon the distorted-wave Born approximation (DWBA). DWBA gives good description of angular distributions and absolute cross sections for direct reactions such as stripping process, pick-up process, inelastic scattering ... etc.[4] DWBA calculations require the use of optical model potential for all particles involved in the nuclear reaction including deuteron, proton, alpha particles ... etc. Optical model potential

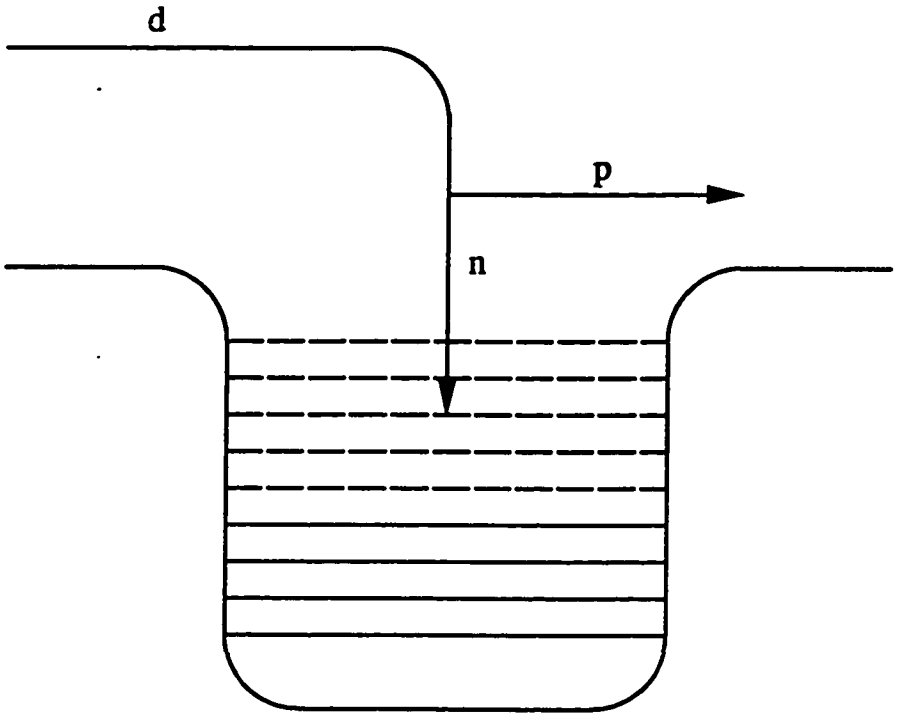

Fig. 1.3. Schematic energy diagram of (d,p) reaction.

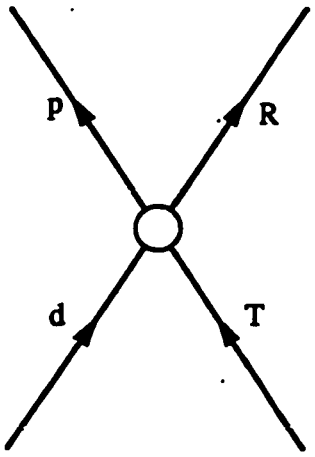

(1) Compound nucleus

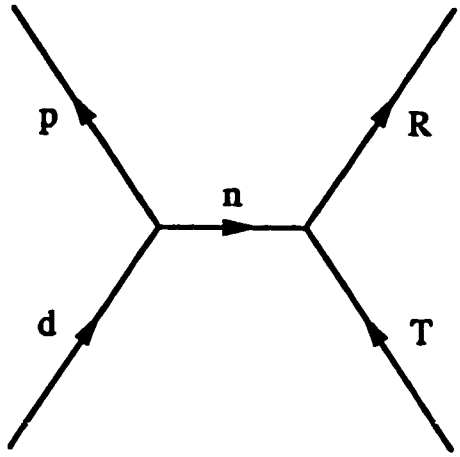

(2) Stripping

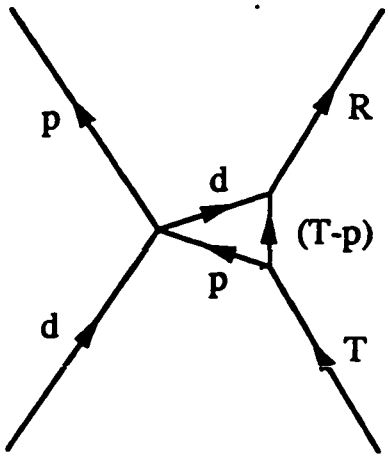

(3) Knock-out

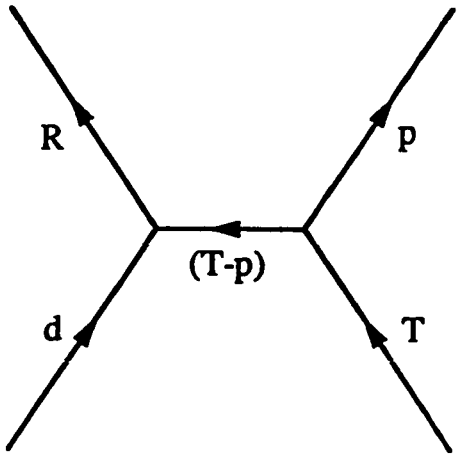

(4) Heavy-particle stripping

Fig. 1.4. Feynman diagrams for dominant (d,p) mechanisims.

has been developed for these particles by measuring the elastic scattering data collides with the proton in the target, ejects it and takes its place in the of the respective particle from the nuclei.[7]

DWBA was successfully applied by G. D. Putt[8] to analysis the angular distribution from $^{12}C(d,p)$ reaction for 0.41 and 0.51 MeV deuterons using single and two nucleon transfer DWBA calculations.

1.3 $^{12}C(d,p)$ Low Energy Data

$^{12}C(d,p)$ reaction is one of the very frequently studied reaction. Literature survey reveals that $^{12}C(d,p)$ reaction has been studied over the deuteron energy range from 0.4 to 80.2 MeV.[9] Since we are interested in reactions with energies below 0.4 MeV deuterons, literature search was done selectively for data below 4 MeV only. Phillips[10] measured the excitation functions and angular distributions for $^{12}C(d,p)$ reaction for deuteron energy range between 0.78 and 1.55 MeV. He observed from the excitation curves the effect of large amounts of interference. Holmgren et al[11] also measured differential cross section of $^{12}C(d,p)$ reaction for 3.29 MeV deuteron. From the forward peaks of the distribution they have inferred the angular momentum of the nuclear state of the residual nucleus using Butler theory. McEllistrem et al[12] have also measured the differential cross section for $^{12}C(d,p)$ reaction in the deuteron energy range of 1.9 to 3.4 MeV. They also observed the interference between the stripping and compound nucleus contributions to the $^{12}C(d,p)$ reaction. The angular distribution of $^{12}C(d,p)$

reaction was measured by Williamson[13] over the deuteron energy range of 0.7 to 1.74 MeV. He explained the results in terms of overlapping compound nucleus levels. The only data below 0.5 Mev is reported by Putt[8]. He has measured the angular distribution at 0.41 and 0.51 MeV deuteron energy. He explained the trend of the angular distribution using DWBA calculation without absorptive potential for the distorted wave.

Due to the lack of $^{12}C(d,p)$ data below 0.41 MeV energy, $^{12}C(d,p)$ reaction was a suitable candidate for reaction study in the energy range of 50 to 350 keV. Experiments in this energy range can be performed with deuteron beam at Energy Research Lab (ERL) accelerator. Another advantage of selecting this reaction was the availability of pure carbon foils commercially. It was decided to measure differential cross section of $^{12}C(d,p)$ reaction at 0.2 to 0.3 MeV to supplement Putt's data.

Chapter 2 deals with experimental setup while chapter 3 deals with data reduction. In the last chapter, results are presented and discussed.

CHAPTER 2

EXPERIMENTAL

The $^{12}C(d,p)$ experiment was carried out on 80 degree beam line of the 350 kV light ion accelerator of the Energy Research Laboratory (ERL) at King Fahd University of Petroleum and Minerals (KFUPM). The accelerator, the scattering chamber along with its accessories, the target, the detectors, the signal processing electronics and the data acquisition system form the core of the experimental hardware for this experiment and they will be described in the following. Since the design of the scattering chamber and its accessories was part of this study, it will be discussed in detail.

2.1 350 kV Light Ion Accelerator

The 350 kV accelerator of the ERL is described in detail elsewhere[14]. For the sake of continuity, a brief summary of the accelerator facility will be given in the following. A layout of the accelerator system is shown in fig. 2.1. The accelerator with three beam lines is located in a concrete hall as shown in the figure. Two of the beam lines, 0 and 45 degree lines, are used to produce 14 MeV neutrons, while the 80 degree beam line is reserved for experiments using charge particle beams. Sinceneutrons are produced in the

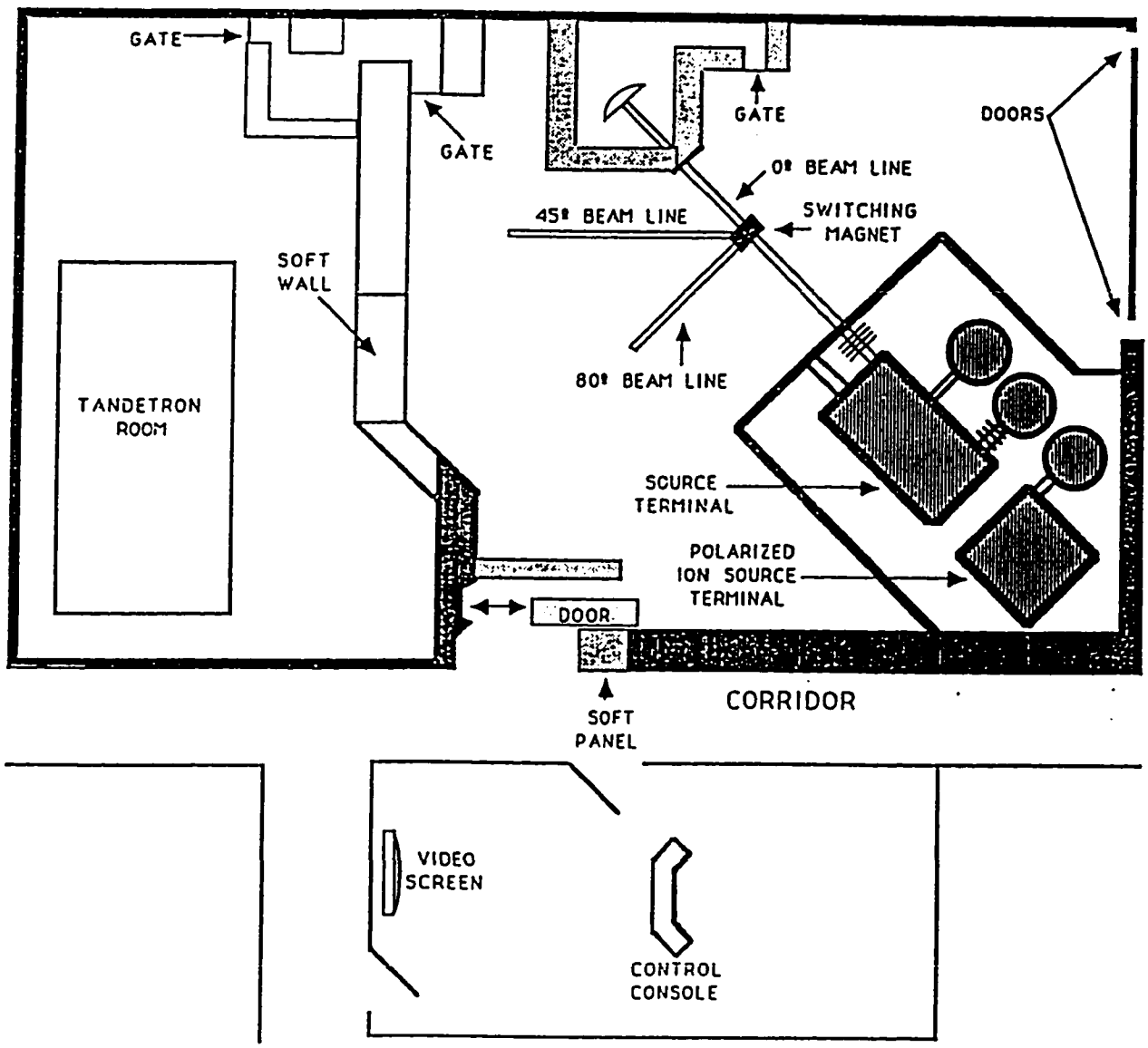

Fig. 2.1. Layout of accelerator system at ERL, KFUPM.

accelerator hall, it has thick shielding walls to reduce the radiation dose outside the hall bellow the permissible limits. The control console of the accelerator is located in a room outside the hall.

The accelerator has three ion sources : two Duoplasmatron sources, models 740 and 820, and one Atomic Beam Polarized-Ion Source. The 740 is a high current source with maximum current of 25 mA while the 820 is a low current source with maximum current of 5 mA. In this experiment, the 820 source was used.

2.1.1 Duoplasmatron Ion Source

In a Duoplasmatron ion source, ions are produced by dissociating gas molecules and then ionizing them by an electron plasma produced by an arc discharge between a hot filament cathode and an anode plate surface. To enhance ionization, the electron plasma is confined by both an axial magnetic field and an electrode, which is maintained at a potential between the cathode and anode potentials. The resulting ion plasma flows out of a an aperture in the anode plate because of the pressure differential. Then, a positive ion beam is extracted by a suitable potential difference between an extraction electrode and the anode plate. Fig. 2.2 shows a sketch of a typical Duoplasmatron ion source.[15,16]

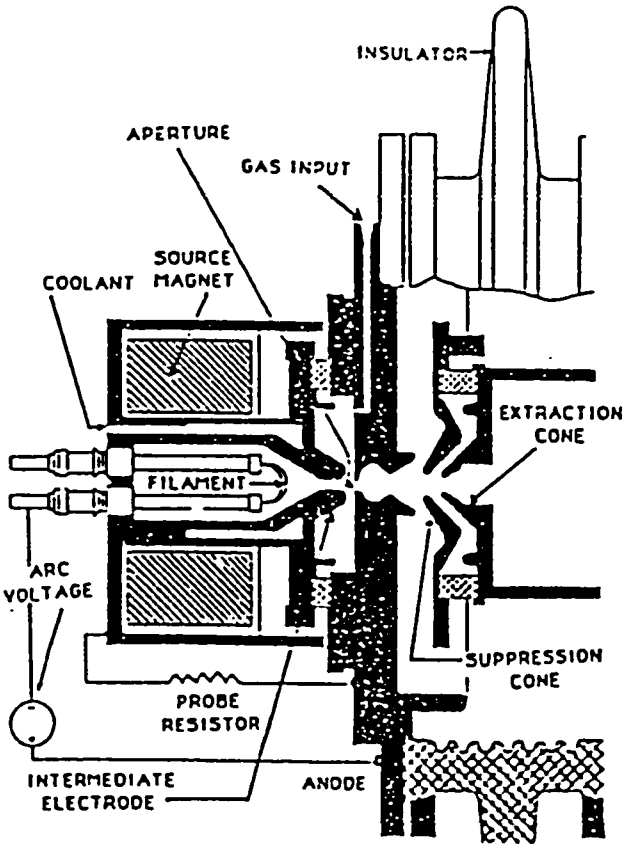

Fig. 2.2. Duoplasmatron ion source.

2.1.2 Accelerator System

A positive ion beam with a maximum energy of 35 keV is extracted from the 820 source and is analyzed and bent through a 90 degree magnet. The low energy beam is then transported through an electrostatic lens, a solenoid lens and retractable aperture to the entrance of the accelerator tube.

The accelerator tube is an air insulated, high field gradient type, designed to operate over the range of 50 kV to 320 kV without substantial changes in the optical properties of the tube. The potential difference between the accelerator electrodes is provided by a water-cooled bleeder resistor column. The resistors used in the column are standard 2 W carbon resistor. The terminal voltage deviation band of the accelerating power supply was measured and found to be less than ± 100 V at 100 KV and ± 200 V at 300 KV. The ripple in the terminal voltage was measured to be 250 V peak to peak at 300 kV.[14]

With the help of a magnetic quadrupole triplet and a magnetic steerer, the beam is transported from the accelerator to the switching magnet where it is deflected to the 80 degree beam line. In the 80 degree beam line, two magnetic quadrupole triplets and horizontal-vertical magnetic steerers are employed to focus the beam on the target which is located inside the scattering chamber fixed at the end of the beam line.

2.2 Scattering Chamber

For the $^{12}C(d,p)$ cross section measurements, a scattering chamber was designed and fabricated in the ERL.at KFUPM. This chamber was installed at the end of the 80 degree beam line. It consists of five components : a rectangular chamber, four detector holders, angular calibrated table, target holder and a beam collimator. All components of the scattering chamber are made of aluminum except the beam collimator which is made of copper. In the following, each component will be discussed separately.

2.2.1 The Rectangular Chamber

The rectangular chamber is 27 cm high, 35 cm long and 35 cm wide. As shown in fig. 2.3, the chamber has four ports. Two opposite ports are used for beam entrance and a faraday cup, while the other two may be used as pumping port and vacuum measuring port. In order to provide an access to inside of scattering chamber, a 33 cm diameter opening is made on the top of the rectangular chamber. This opening is large enough to allow not only changing the detector angles, but also taking the detector table out of the chamber. The chamber can also be rotated about the beam axis providing various inclination angles with respect to horizontal plane.

2.2.2 The Detector Mount

Fig. 2.4 shows the detector mount, the holder and the collimator. The

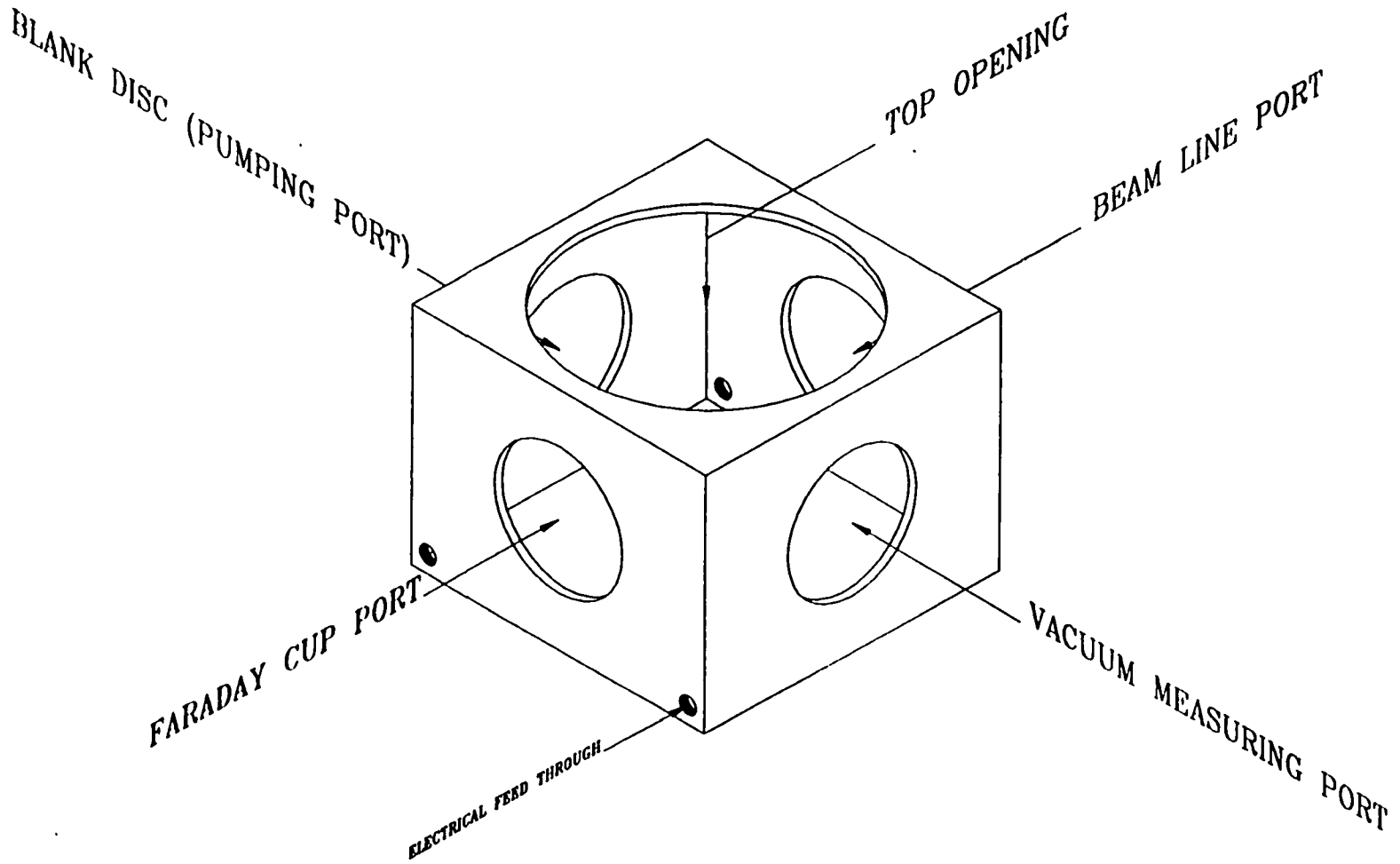

Fig. 2.3. A schematic diagram of the rectangular chamber.

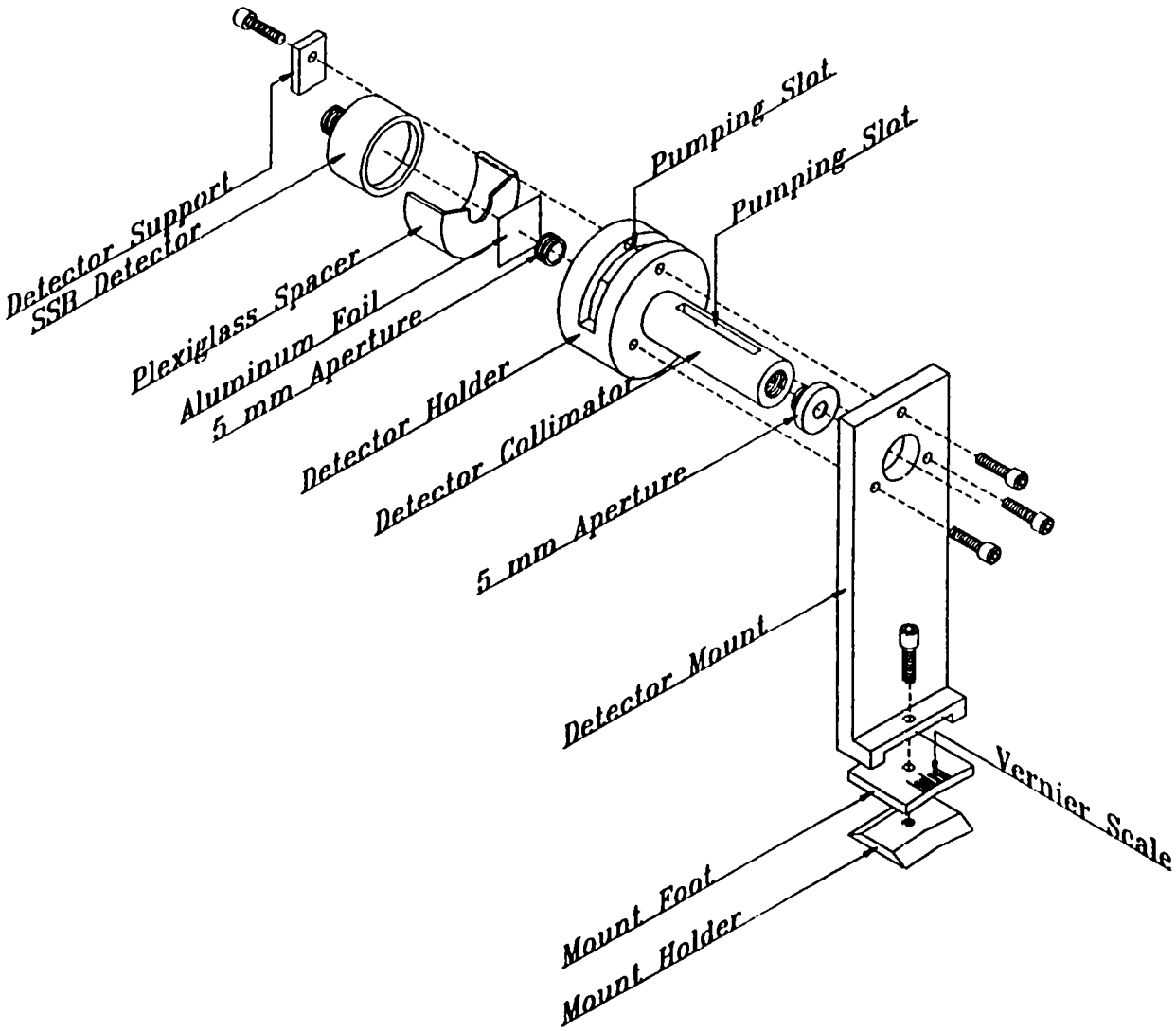

Fig. 2.4. A schematic diagram of the detector mount, holder and collimator.

detector holder and the collimator are made from one piece and are fixed to the mount with the help of three screws. In order to provide electrical isolation between the detector and its aluminum holder, a plexiglass spacer is inserted between the detector and its holder. The region in front of the detector is evacuated through pumping slots cut in the detector holder and the plexiglass spacer. The detector is pressed against the holder by a plexiglass piece, bolted to the edge of the holder. The cylindrical collimator in front of the holder, is also provided with pumping slots. Two circular aperture discs, separated by 40 mm are screwed to the front and to the back of its collimator. By choosing different aperture diameters of the discs, one can choose the desired detector solid angle. In this experiment, the diameter of both apertures are 5 mm. The 5 mm aperture, just in front of the detector, is at a distance of 131 mm from the center of the target. Thus, the effective solid angle of the detector is 1.14 mster.

2.2.3 The Detector Table

The detector holder is mounted on the angular calibrated circular table which is bolted to the base of the scattering chamber. The main scale is marked on the table while vernier angular scale is made at the foot of each detector mount. With this vernier angular scale an accuracy of 0.1 degree can be achieved in positioning the detector mounts. For changing the detector angle, the detector mount is slid in a circular groove in the table. This groove forces the detector to point always towards the center of target about which the detector rotates. After changing the angle, the detector

mount is bolted again to the groove. The hole, through which the table is fixed to the chamber floor, is large enough to allow side shifting of the table during alignment of the table. Three screws fixed to the table are used to level the table horizontally. Fig 2.5 shows the angular calibrated table.

2.2.4 The Target Mount

The target mount is fixed at the center of the table. As shown in Fig. 2.6 the target holder can be rotated in various angles of inclination with respect to the beam axis. The target foil is mounted on a frame which is fixed to the target holder.

2.2.5 The Beam Collimator

The beam collimator is extended from the beam tube into the scattering chamber. The beam collimator has two parts. The longer part is 35 cm in length and 1.8 cm internal diameter. Most of it is located inside the beam tube before the scattering chamber. The shorter part is 6.0 cm long and has 0.5 cm internal diameter. Both parts are screwed together and are located inside the scattering chamber at a distance of 3.0 cm from the target. The shorter collimator which is closer to the target, has two circular aperture discs on both ends. These apertures define the beam diameter at the target. Both collimator parts are provided with pumping slots. The collimator is centered inside the beam tube with the help of two copper centering discs. In order to pump the beam line efficiently, the centering

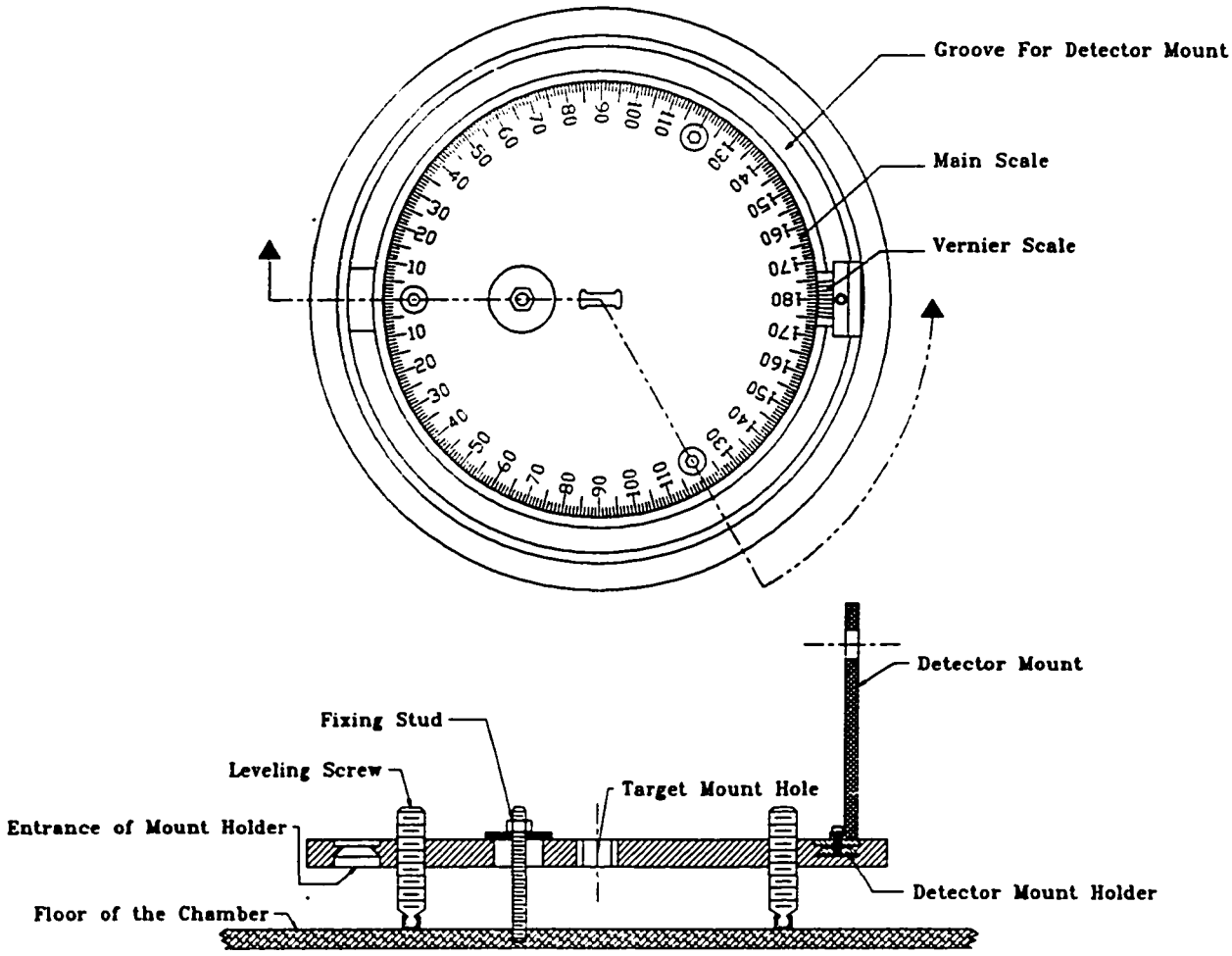

Fig. 2.5. A schematic diagram of the angular calibrated table.

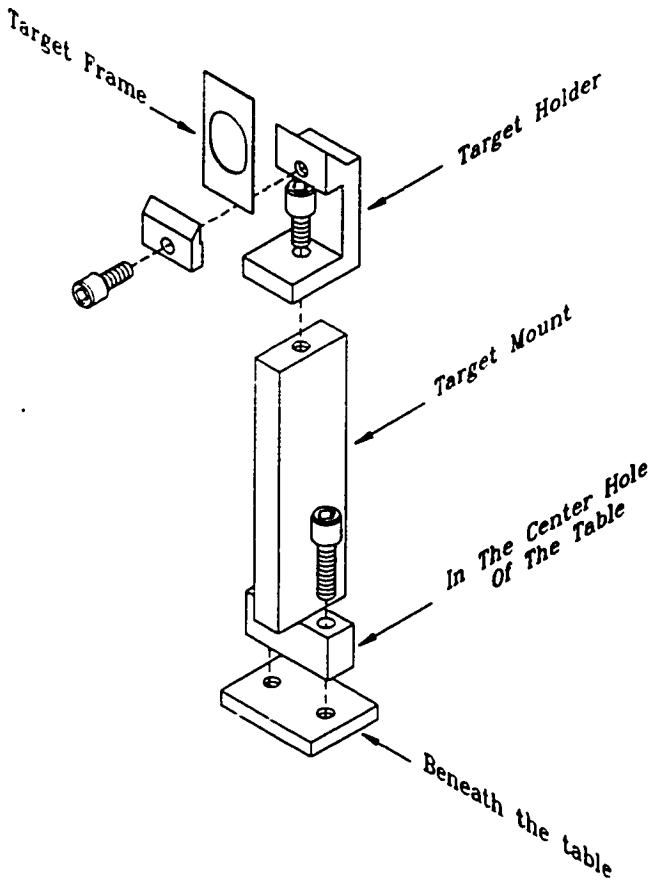

Fig. 2.6. A schematic diagram of the target mount and holder.

disc has three 50 degree alternate segments cut out of the disc. To shield the interior of the scattering chamber from the incident beam, both discs are rotated such that the void segments from one disc overlaps the metal segment of the other disc. In this way, no beam enters the scattering chamber except the one passing through the collimator. The centering of the beam collimator is very critical in this experiment because it defines the beam axis. The alignment of the table and the detectors was done with reference to the collimator axis. A sketch of the beam collimator is shown in fig. 2.7.

2.2.6 Alignment of Detectors

The reaction plane is the plane formed by the beam axis and detector collimator axis. Here, the beam axis is defined by the beam collimator axis. Therefore the detector collimator has to be aligned with respect to beam collimator axis. This is done by an optical alignment using a telescope. At first, the telescope axis is aligned to the beam axis using two 1-mm-diameter apertures in the beam collimator. With the help of three leveling screws of the table, the detector table is adjusted such that the axis of the detector collimator placed at 0 degree as well as 180 degree coincides with the telescope axis. The axes of the other three detector collimators when placed at 0 and 180 degrees are found to be within ± 0.2 mm with respect to the telescope axis. Fig. 2.8 shows a schematic view of the alignment setup. It is assumed that the detector collimators at angles other than 0 and 180 degrees are in the same plane since they are slid in the planar groove in the thick aluminum table. Due to the ± 0.2 mm uncertainty in the detector collimator

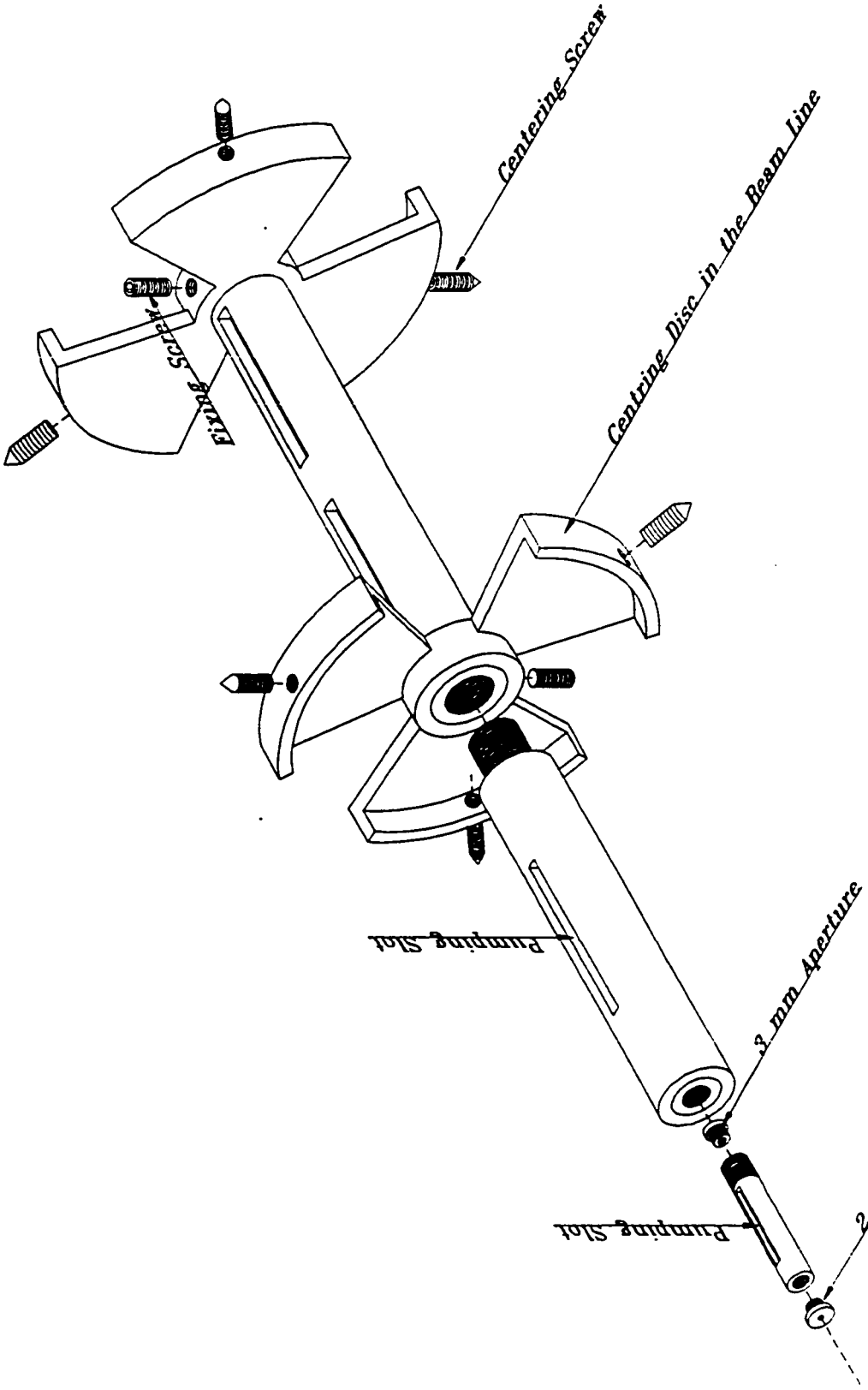

Fig. 2.7. A schematic diagram of the beam collimator.

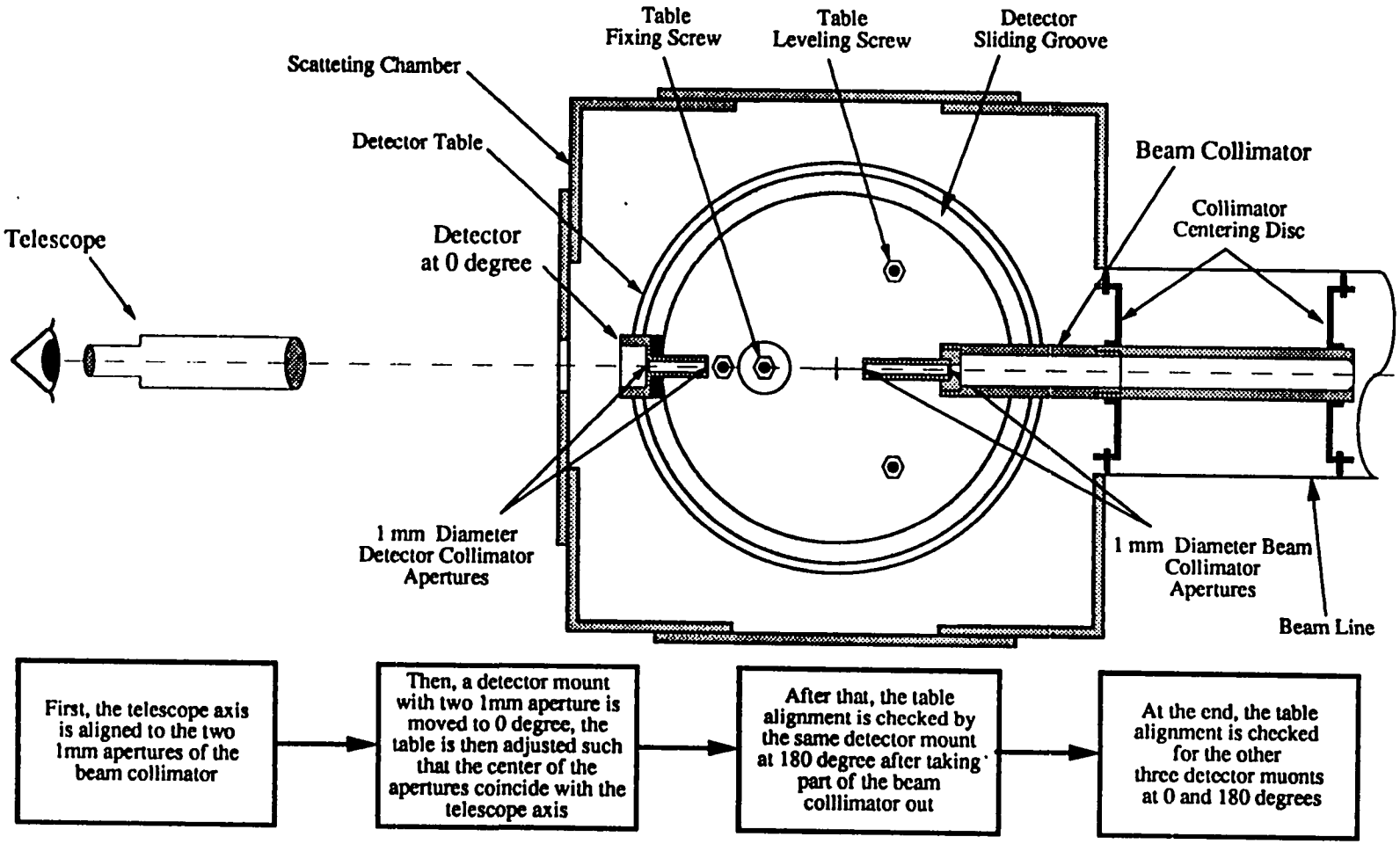

Fig. 2.8. Schematic view of the detector alignment Setup.

alignment, the first aperture of the detector collimator was made large enough such that the aperture just before the detector view the target without any obstruction.

2.3 The Carbon Targets

Since it was desired to minimize the energy loss of the incident beam in the target and to measure the current of incident beam from the transmitted beam, very thin carbon targets were used. The carbon target is in the form of a self supporting foil, supplied by Arizona Carbon Foil Company, Arizona, USA. Since the thin carbon foils are fragile and can not be transferred directly to the target frame, they are first floated on the water surface and are then lifted on the target frame.

The thickness of the carbon foil was chosen after calculating total energy loss of deuteron in the foil. The total energy loss ΔE of deuteron is calculated using the expression

$$\Delta E = \int \frac{dE}{dx}\, dx \qquad (2.1)$$

where $\frac{dE}{dx}$ is the specific energy loss of deuterons in carbon and x is the thickness through which deuterons traverse in carbon. The values of $\frac{dE}{dx}$ are calculated using the energy loss calculation computer code TRIM-87 on an IBM compatible PC. The program uses the corrected Bethe-

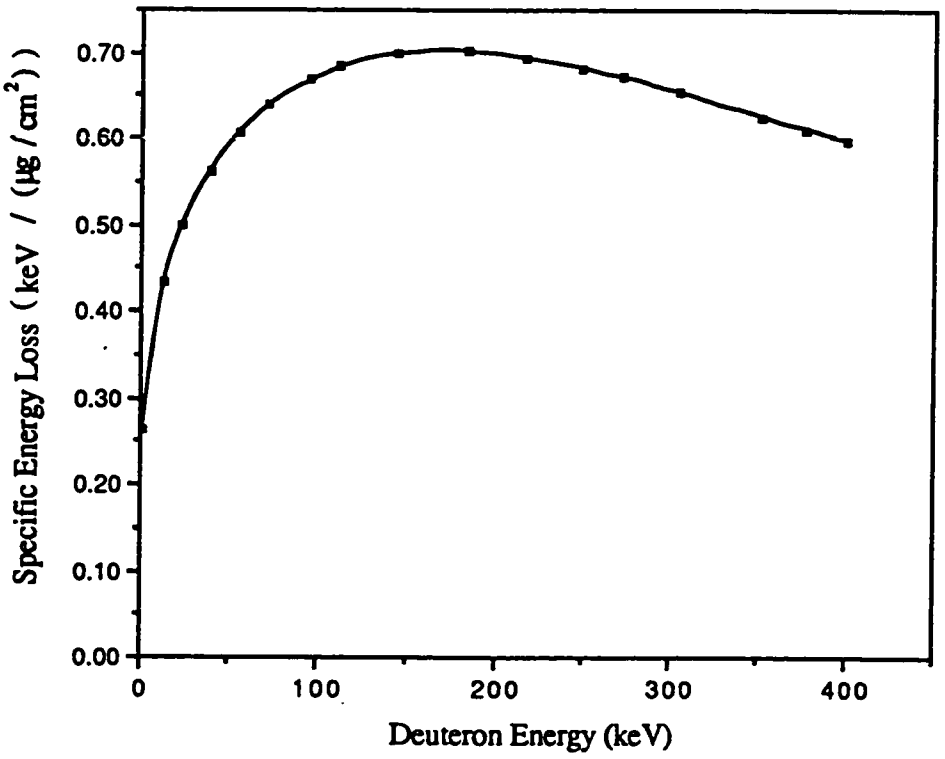

Fig. 2.9. Specific energy loss of deuterons in carbon calculated by TRIM-87 program.

Bloch formula[18] to calculate the energy loss of charge particles. Fig. 2.9 shows specific energy loss of deuteron in a carbon foil up to 400 keV deuteron energy. The energy loss curve shows a maxima around 150 to 180 keV deuteron energy. In our region of interest, i.e. 150 to 300 keV, the energy loss varies between 0.65 to 0.70 keV/($\mu g/cm^2$).

The energy loss calculations have shown that deuterons with energies from 160 to 300 keV suffers an energy loss of 13.2 to 14.0 keV in a 20 $\mu g/cm^2$ thick carbon foil. The calculation procedure of the total energy loss is given in Appendix E. The foils thicker as well as thinner than 20 $\mu g/cm^2$ were not considered because thicker foils introduce large errors in the incident beam energy while thinner foils are too difficult to mount on the target frame.

2.4 The Semiconductor Surface Barrier Detectors

Due to their excellent energy resolution, Semiconductor Surface Barrier (SSB) detector are widely used in charge particle spectroscopy[17]. In this experiment protons from $^{12}C(d,p)$ reaction were detected using SSB detectors. These detectors rely on the junction formed between a semiconductor and certain metals. Usually n-type silicon is used with gold, while p-type silicon is used with aluminum. Because of the high conductivity of metals, the depletion zone extends entirely into the semiconductor[18]. The detector used in this experiment, which is shown in fig. 2.10, is a diode with 40 $\mu g/cm^2$ evaporated gold contact on an etched n-type silicon wafer. A 40

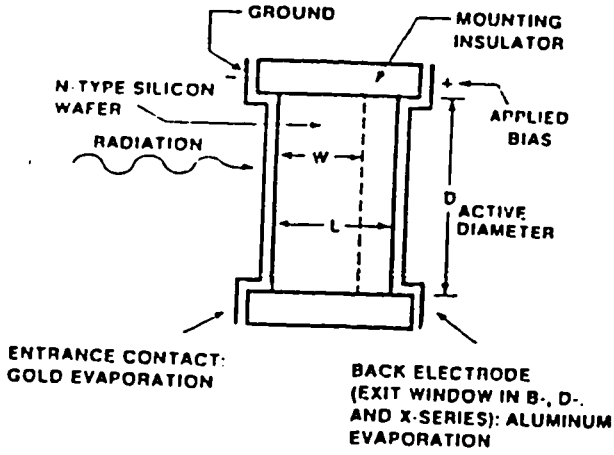

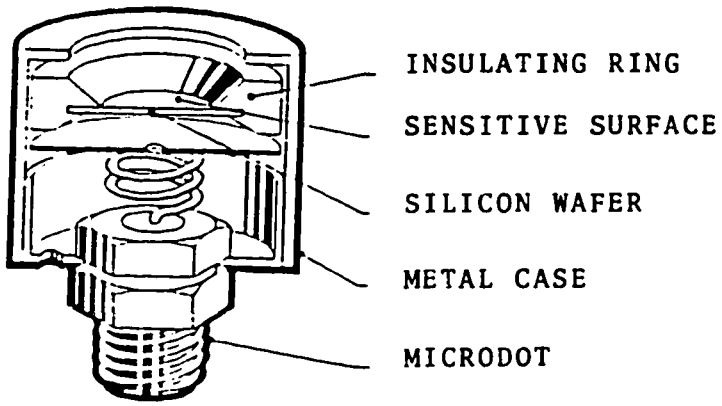

Fig. 2.10. Cross section and configuration of the SSB detector used in this experiment.

reverse-bias voltage, that is the positive polarity on aluminum contact, is applied to the diode, an electric field is created in the depletion region. The radiation incident in the depletion region releases free charge carriers which are collected by the electric field, thus a signal is produced.[19]

Since the energy of the protons from the $^{12}C(d,p)$ reaction at 160 to 300 keV deuteron energies varies from 2.5 to 3.8 MeV, an SSB detector with 100 μm depletion layer depth can stop these protons[20]. In order to choose smaller solid angle, 5 mm diameter aperture is placed in front of the detector which resulted in a solid angle of 1.14 mster. Therefore any detector having an active area larger than 20 mm^2 can be used in this experiment. EG&G Ortec SSB detectors model A-016-100-100 meet the previous requirements and are used in the present experiment. Each of the detectors is operated at 100 volts positive bias voltage.

The SSB detector is sensitive to light. Since the energy of the visible light ranges from 2 to 4 eV which exceeds 1.1 eV energy gap in silicon, the detector generates large noise when exposed to light. The thin gold coating is insufficient to stop ambient light. So, it is recommended to operate the SSB detector in light tight chambers [18]

2.4.1 Deuteron Stopping Foil

In the reaction under study, the detector detects protons as well as the elastically scattered deuterons. The intensity of the scattered deuterons is very high compared to that of protons. As an example, from the Rutherford

formula for coulomb scattering[3], it can be shown that a 100 keV deuteron beam of 1 μA current can scatter 10^7 deuterons/sec from 20 μg/cm^2 carbon foil into a detector with 1.14 mster solid angle placed at an angle of 30 degree with respect to the beam axis. On the other hand, the intensity of the protons from the ^{12}C(d,p) reaction is of the order of 1 count/sec. As per the manufacturer manual, the SSB detector is sensitive to radiation damage and its performance deteriorates significantly after detecting 10^{12} deuterons/cm^2. If 10^7 deuterons/sec are detected by the detector, the radiation dose limit of 10^{12} deuteron/cm^2 will be reached in a short time of about 5.5 hours[20]. Usually a foil, thick enough to stop the deuterons and thin enough to allow the protons to pass through, is placed in front of a detector.[8,12,21] In this experiment, a 5 μm aluminum foil is inserted just in front of each detector. As it is clear from figs. 2.11 and 2.12, a thickness of 5 μm is enough to stop deuterons with energy between 50 to 350 keV while it is transparent for protons having energy between 2.5 to 3.8 MeV. The energy loss of 2.5 to 3.0 Mev protons in 5 μm aluminum foil is calculated by the TRIM-87 program to be 131 to 115 keV

2.5 The Faraday Cup

The faraday cup is used to measure the incident beam charge. In this experiment, the thin target allows most of the beam to be transmitted to the faraday cup. Therefore, charge collected by the faraday cup can be used to calculate the flux of the incident beam which is required for reaction cross section calculations. Fig. 2.13 shows a diagram of the faraday cup.

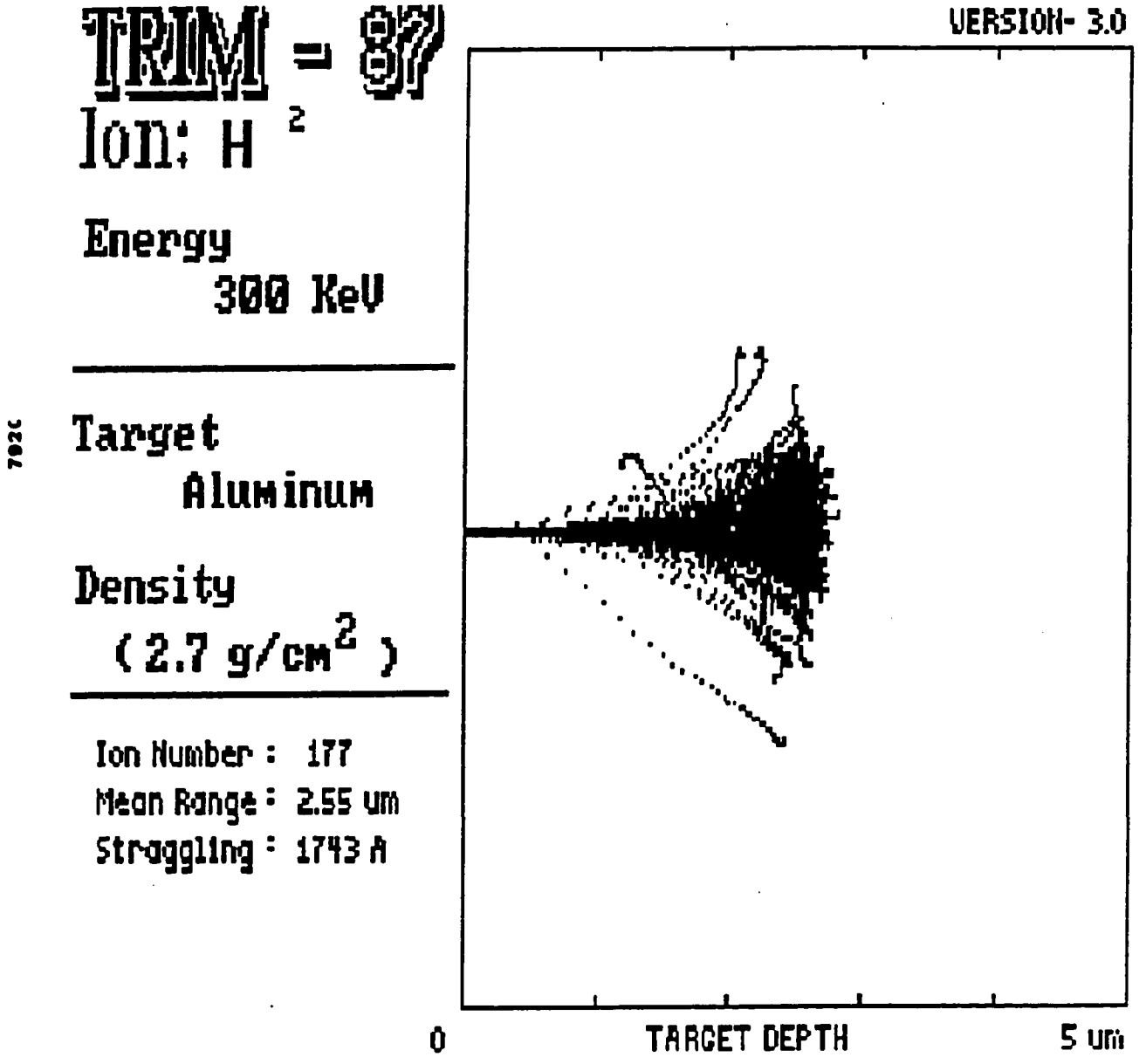

Fig. 2.11. Range of 350 keV deuterons in 5 μm aluminum foil.

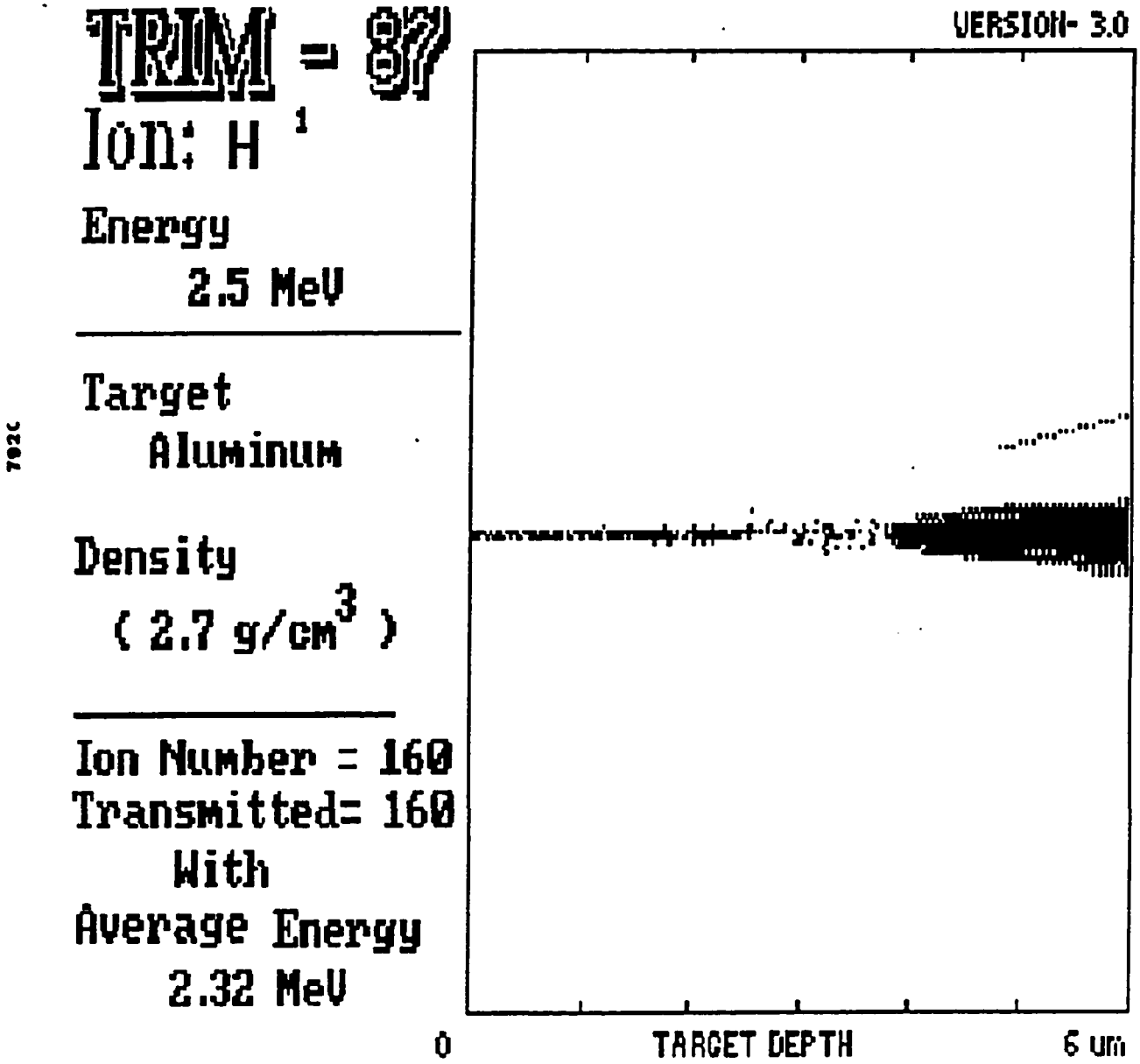

Fig. 2.12. Range of 2.5 MeV protons in 5 μm aluminum foil.

The faraday cup consists of an electrically isolated electrode which is connected to a charge measuring device. When a positively charged beam hits the electrode, it knocks out electrons which cause an additional current to flow through the measuring device. This results in a false current measurement. In order to suppress the knocked out electrons, a suppressor ring is kept in front of the electrode. The suppressor ring is kept at a negative potential with respect to the electrode. To prevent the incident beam from hitting the suppressor ring, an aperture, with diameter smaller than the inner diameter of the ring, is placed in front of the suppressor ring. The faraday cup is mounted on the scattering chamber.

Fig. 2.14 shows the experimental setup used for the $^{12}C(d,p)$ experiment. Individual components of this setup were described earlier.

2.6 Electronics

In this experiment identical standard NIM electronics is used to acquire data from four detectors. Fig. 2.15 shows the block diagram used for one detector.

Bias voltage of the SSB detector is supplied by a power supply hooked to a Canberra charge sensitive preamplifier Model 2003PT. The preamplifier is externally connected to the SSB detector feedthrough at the scattering chamber. The energy signal from the preamplifier is transported to patch panel for further transportation to signal processing electronics

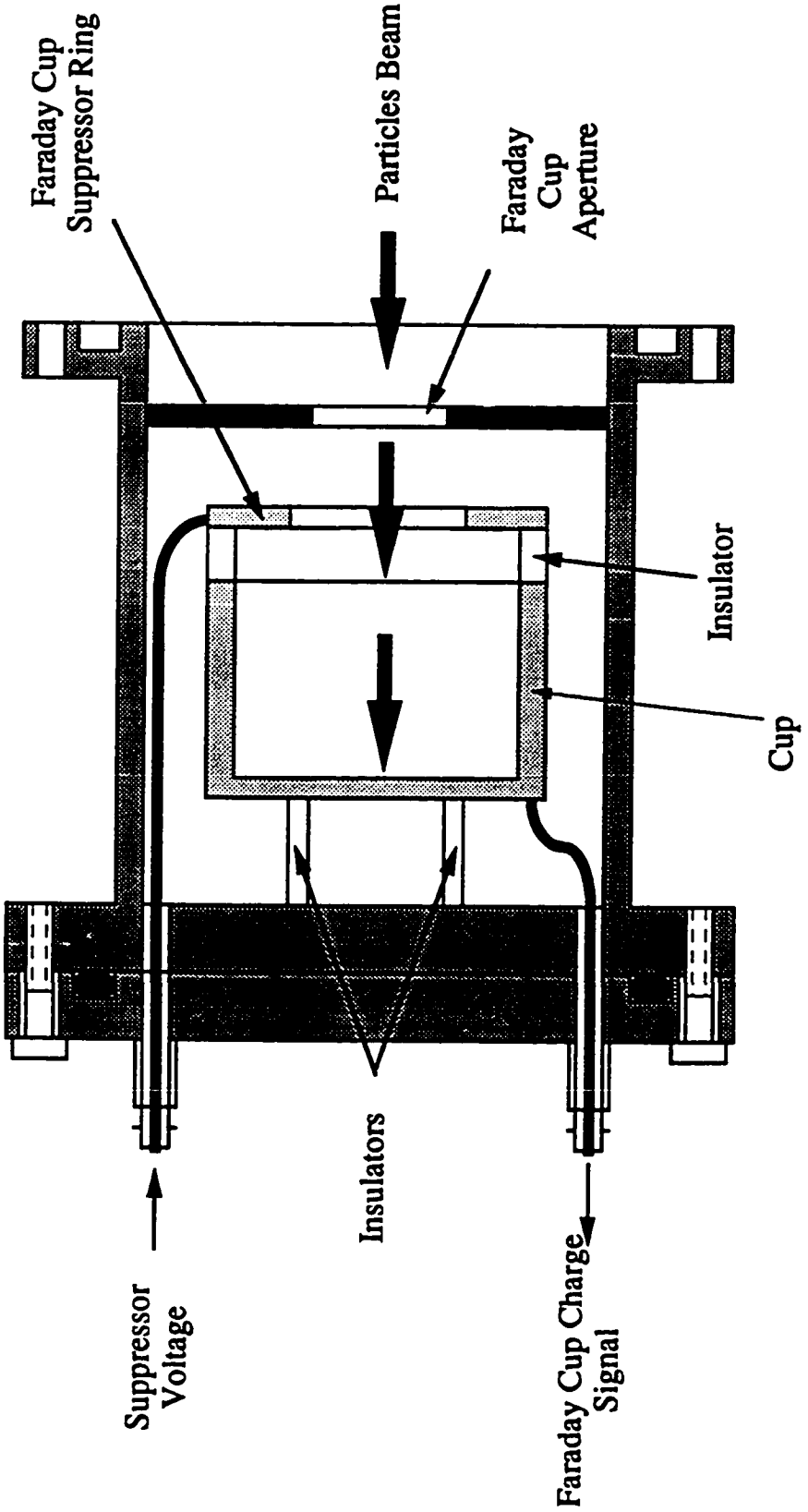

Fig. 2.13. Schematic diagram of the faraday cup.

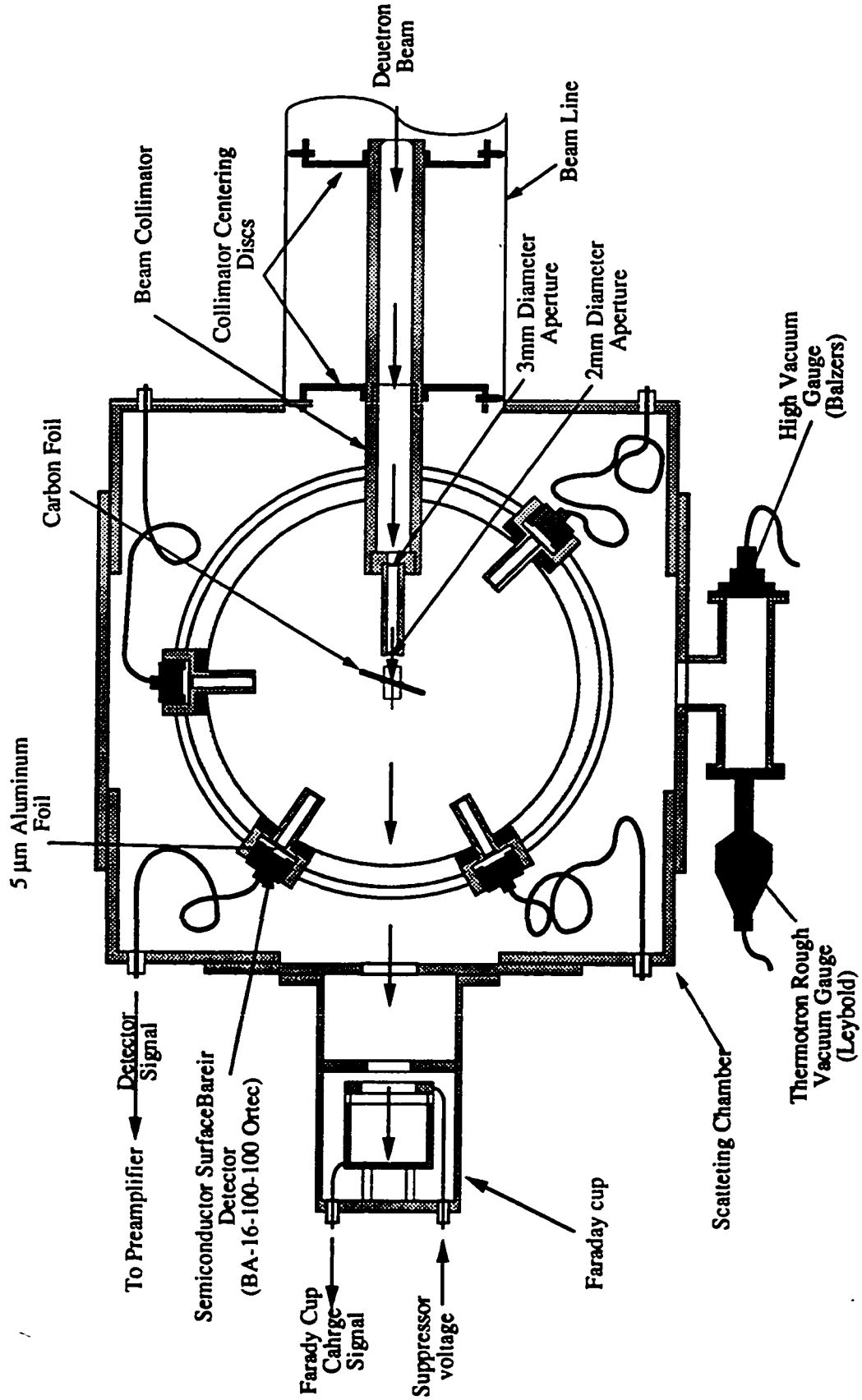

Fig. 2.14. Experimental setup for the $^{12}C(d,p)$ reaction.

ocated in the accelerator control room. The detector signal is then shaped and amplified by an EG&G Ortec spectroscopy amplifier Model 572. The unipolar output is fed to a LeCroy Analog to Digital Converter (ADC) Model 3511 for pulse height analysis, while the bipolar output is connected to an EG&G Ortec Single Channel Analyzer (SCA) Model 550 to generate a trigger signal for pulses of interest. The output of the SCA is connected to an EG&G Ortec Gate and Delay Generator Model 416A. One output of the gate and delay generator is connected to the gate input of the LeCroy ADC. The delay in the gate and delay generator is adjusted such that the gate signal arrives at the ADC earlier than the amplifier signal. The other output of the gate and delay generator is counted by LeCroy CAMAC Scaler Model 2551 for dead time calculations. The dead time is calculated by dividing the total numers of gates with the total number of events digitized by correspongin ADC

Data are acquired for a fixed number of charge, collected by the faraday cup. For an accurate measurement of the charge, it is required to convert the charge signals into pulses which can be later on counted by a scaler. Here the faraday cup charge signal is connected to an EG&G Ortec Digital Current Integrator Model 439 which digitizes it into pulses. The digitized output of the current integrator is fed to the Borer CAMAC Preset Counter/Timer Model 1008. The preset scaler accepts only NIM signals but the output of the digital current integrator is TTL. This requires a conversion of the TTL signal to a NIM signal which is achieved by a LeCroy Level Adaptor Model 688 AL. The outputs from the rear panel of the

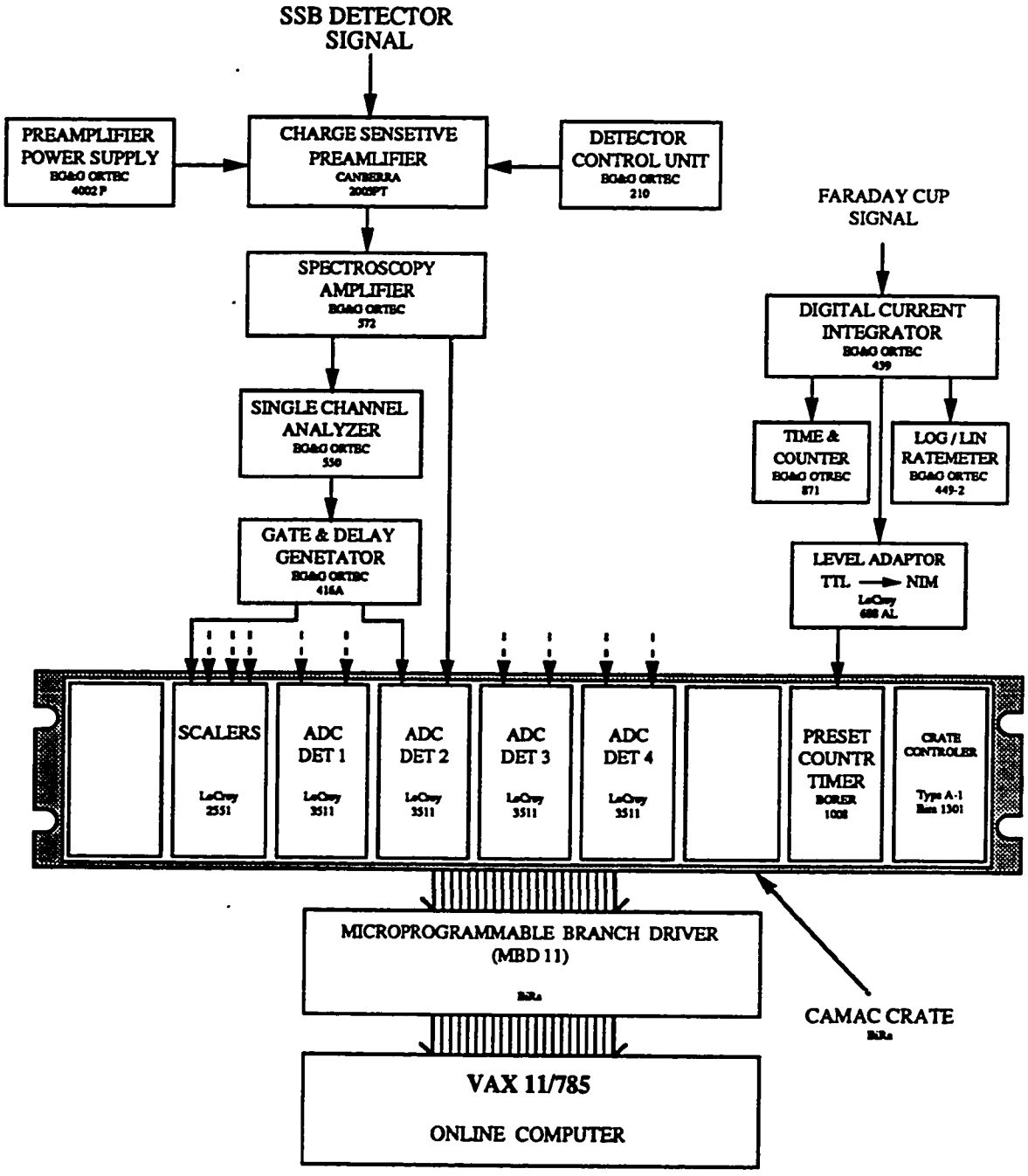

Fig. 2.15. Bolck diagram of the data acquisition electronics.

current integrator are connected to an EG&G Ortec Timer Counter Model 871 and an Ortec Log/Lin Ratemeter Model 449-2. The timer counter is used as a frequency meter and it monitors the beam current while the ratemeter is used as audible alarm for beam current.

A description of the electronics NIM modules used in this experiment is given in Appendix B for further reference.

The LeCroy CAMAC ADC's, LeCroy CAMAC Scalers and Borer Preset Scalers are mounted in a BiRa CAMAC crate which is an integral part of ERL data acquisition system to be discussed later.

2.6.1 Calibration of Current Integrator

The current integrator is used for precise measurement of charge. This requires calibration of the integrator. A variable current source was used to calibrate the integrator usin the setup as shown in fig. 2.16. the current, supplied by a Quik-E Calibrator Pioneer/Instrumentation power supply model 450A and a standard resistor, was first measued by a keithely Picoammeter model 485 and then is was fed to the digital current integrator. The digitized output of the current integrator was counted by an EG&G Ortec frequency counter model 871. The current through the integrator can be calculated from its preset charge per pulse and readout of the frequency counter. The current though the integrator was compared with the current measured by the picoammeter. Fig. 2.17 shows the intergrator current

Fig. 2.16. Electronics block diagram for the calibration of the current integrator.

plotted as a funtion of the picoammeter readout. The slope of the line is 0.975 which shows 2.5% deviation of integrator readout from the picoammeter readout.

2.7 Data acquisition and Analysis System

The data acquisition and analysis facility at ERL is built around 2-node single-CPU VAX 11/785 cluster. It uses a CAMAC/Microprogrammable Branch Driver (MBD) hardware. An overview of the ERL system can be found somewhere else[22,23,24].

The data acquisition hardware consists of two separate and identical parallel CAMAC branches, each controlled by a Microprogrammable Branch Driver (MBD) which acts as an 8-channel Direct Memory Access (DMA) interface between the CAMAC branch and the VAX unibus. Experimental data is acquired using number of LeCroy 3511 fast CAMAC Analog to Digital Converter (ADC) modules. The Tektronics color display terminals are used to display the detector spectra. A Borer Model 1008 preset scaler is used to stop the data acquisition process. The detector signals can also be counted using LeCroy CAMAC Scalers Model 2551 for dead time correction for each MBD channel.

The data acquisition system uses XSYS software package which was developed in Triangle Universities Nuclear Lab, USA for VAX computers[25]. The data acquisition program consists of three files. These are COM, DAP

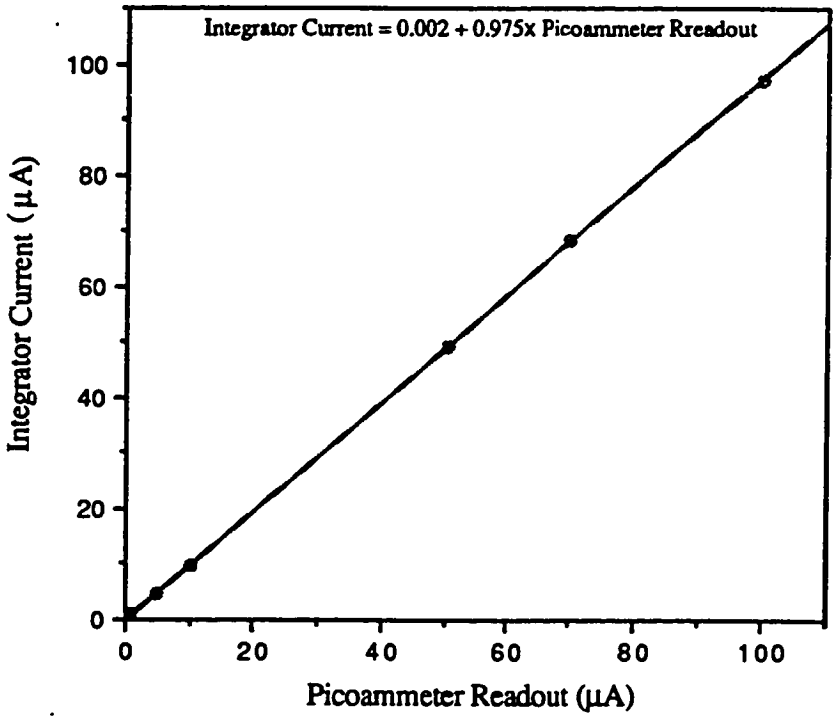

Fig. 2.17. Calibration Graph for the Ortec 439 current integrator.

and EVL files.

The COM file contains XSYS commands which are executed at various stages of the experiment. The DAP file is CAMAC and subprocess control files. It contains CNAF commands for CAMAC crate configuration and information on the VAX data buffer size. Each active MBD channel requires a separate DAP file. DAP files are also used for general subprocess control information such as the scaler-timer preset or the scaler display. These files are very hardware specific. The EVL file contains sorting algorithms for individual ADC and its MBD channel. Each active MBD channel requires its own EVL sort program. Therefore each MBD Channel requires one DAP and one EVL file for data acquisition. If the data acquisition is controlled by a preset scaler, it needs only one more DAP file to read the preset scaler.

In this experiment, data from four detectors were acquired through four ADCs with gain of 1024 channels each. Four sets of DAP and EVL files were written for the data acquisition program. Data are acquired for a fixed number of counts of the digital current integrator counted by a preset scaler which is basically a down counter. Apart from this, each MBD channel requires a scaler for dead time correction. The preset scaler and the remaining four scalers are read by the VAX through another DAP file.

XSYS offers the facility to display the content of the preset scaler/timer and the scalers on a terminal using Fortran subroutine

BOXUSR.FOR. The box display contains 36 boxes to display information about the preset scaler, LeCroy scalers and XSYS data areas sorted by EVL files. Fig. 2.18 shows a typical box display used in this experiment. First four boxes are reserved for the MBD scalers which shows the accumulated counts from the corresponding detector gates. Boxes 5 and 6 are allocated for the values of the remaining preset and the total preset counts. A gate is set on the proton peak in each detector spectrum. The counts in the gates of detector 1 to 4 are displayed in boxes 9 to 12 while the lower and the upper channels of corresponding gate are displayed in boxes 17 to 20. Using the instantaneous accumulative values of gate counts and the digital current integrator counts the expected yield of each detector for a given preset counts is calculated and displayed in boxes 21 to 24.

The listing of data acquisition codes is given in Appendix C

2.8 Accelerator Beam Energy Measurement

Usually the beam particle energy is measured using a nuclear reaction with known resonances or threshold energies. For a low energy accelerator Al(p,γ) reaction along with four resonances at 203, 223, 293 and 327 keV offers a convenient calibrating nuclear reaction. Fig. 2.19 shows a thick target yield curves near these resonance energies.[26] The ERL accelerator voltage readout was checked for one resonance only. Out of these four resonances, two higher energy resonances at 293 and 327 keVwere not considered because they required the accelerator to be operated at the upper

DET1. 76744		DET2. 115324		DET3. 108955		DET4. 123586	
CUR.PER. 0	PRESET 500000			AREA1 7769.000	AREA2 9227.000	AREA3 8131.000	AREA4 8714.000
TOT.BCI 500000	0			GATAREA1 458.5120	GATAREA2 439.4740	GATAREA3 431.4740	GATAREA4 403.4530
NOR.DET1 7769.000	NOR.DET2 9227.000	NOR.DET2 9227.000	NOR.DET4 8714.000	DTC1 1.000218	DTC2 1.000356	DTC3 1.000432	DET4 1.000456
_____DATA ACQ. OFF_____							

Fig. 2.18. Box display of the data acquisition system.

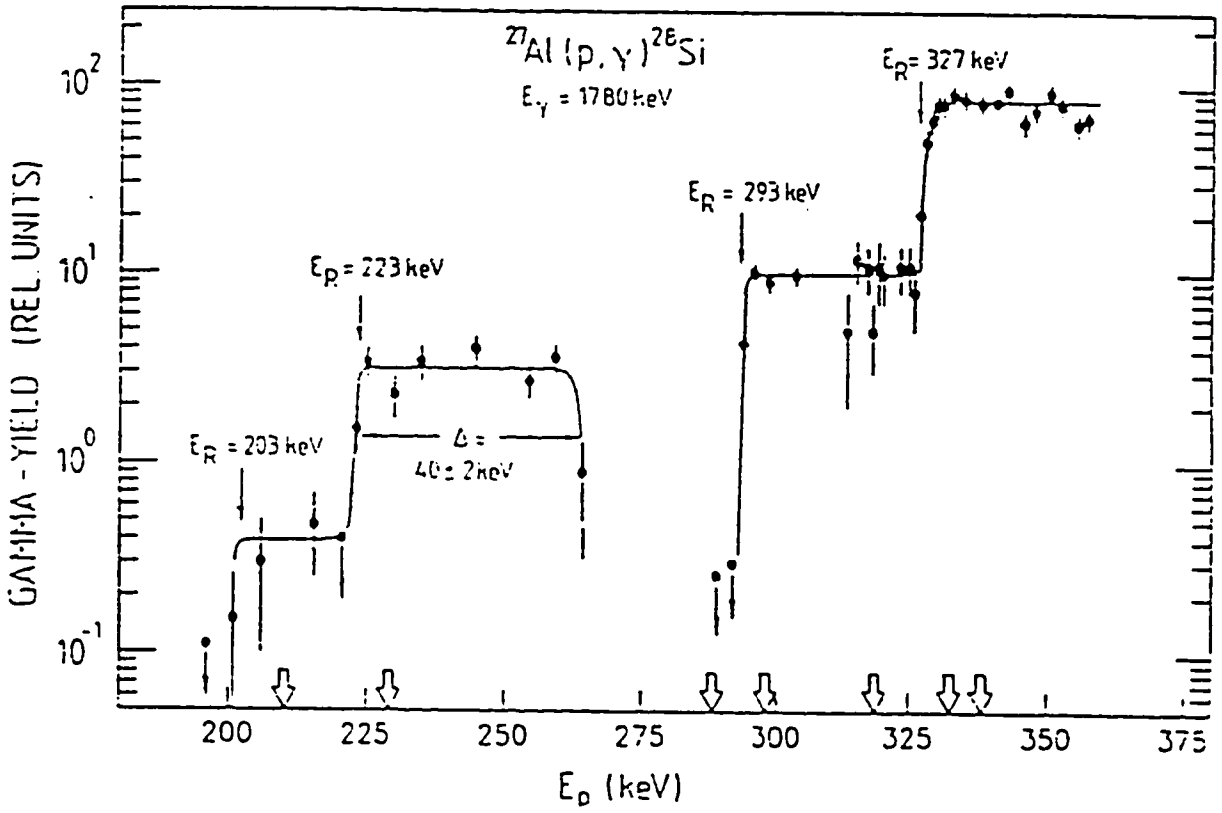

Fig. 2.19. Thick-target yield curves of Al(p,γ) reaction near 203, 223, 292 and 327 keV resonances.

limit of the power supply which may cause breakdown of the accelerator. As the yield of 203 keV resonance is less than that of 223 keV by an order of magnitude, practically it is quite difficult to study the 203 keV resonance with good statistics[27]. Due to this reason, the accelerator energy was checked around 223 keV resonance. The Al(p,γ) reaction was studied with proton energies ranging from 200 to 225 keV.

The Al(p,γ) reaction yields 1.78 MeV gamma rays which were detected by an EG&G Ortec Hyper Pure Germanium detector Model GAMMAX using the electronics and data acquisition system mentioned in the previous section. Fig 2.20 shows the experimental setup for Al(p,γ) reaction study. The aluminum disc target was mounted in the faraday cup. In the test runs of the experiment, carbon buildup on the target was noticed. This buildup was due to vacuum system and drive-in deuterons from the accelerator[27]. It was noticed that the carbon buildup was a function of total number of incident beam particles. In order to minimize the carbon buildup, the yield of gamma rays for each proton energy was measured for a fix duration of 30 minutes with a beam current of 100 to 120 μA. The fix duration of run time kept a constant background under the gamma peak. The target surface was cleaned before the beginning of each run. Fig 2.21 shows a typical gamma rays spectrum of Al(p,γ) reaction at 220 keV proton energy. In order to identify the peak, the gamma spectrum was calibrated using standard ^{22}Na and ^{137}Cs gamma ray sources. The 1.780 MeV gamma rays yield was measured for proton energies ranging from 200 to 225 keV. Fig. 2.22 shows gamma rays spectra for 200 and 225 keV superimposed on

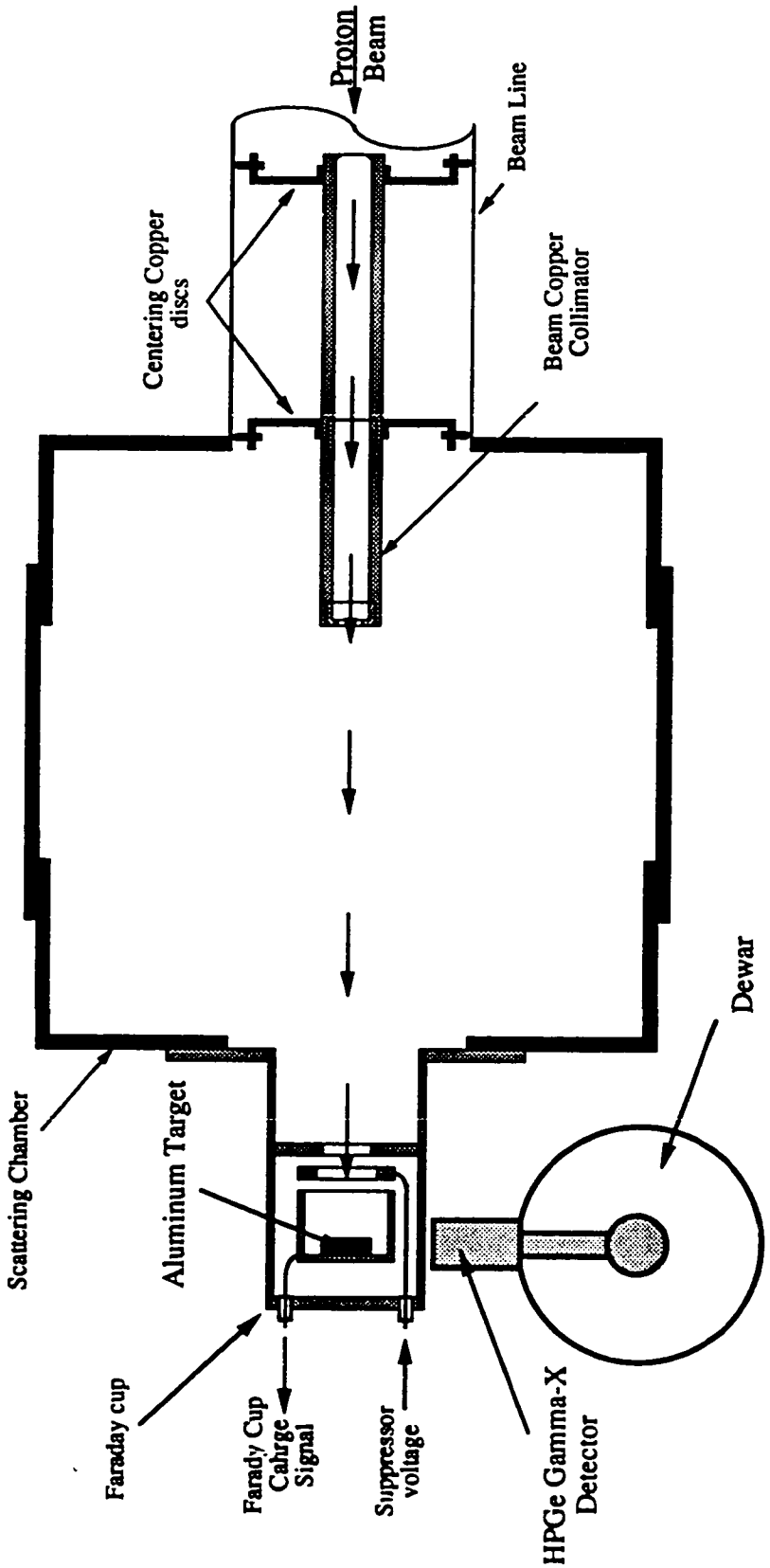

Fig. 2.20. Experimental setup for Al(p,γ) reaction study.

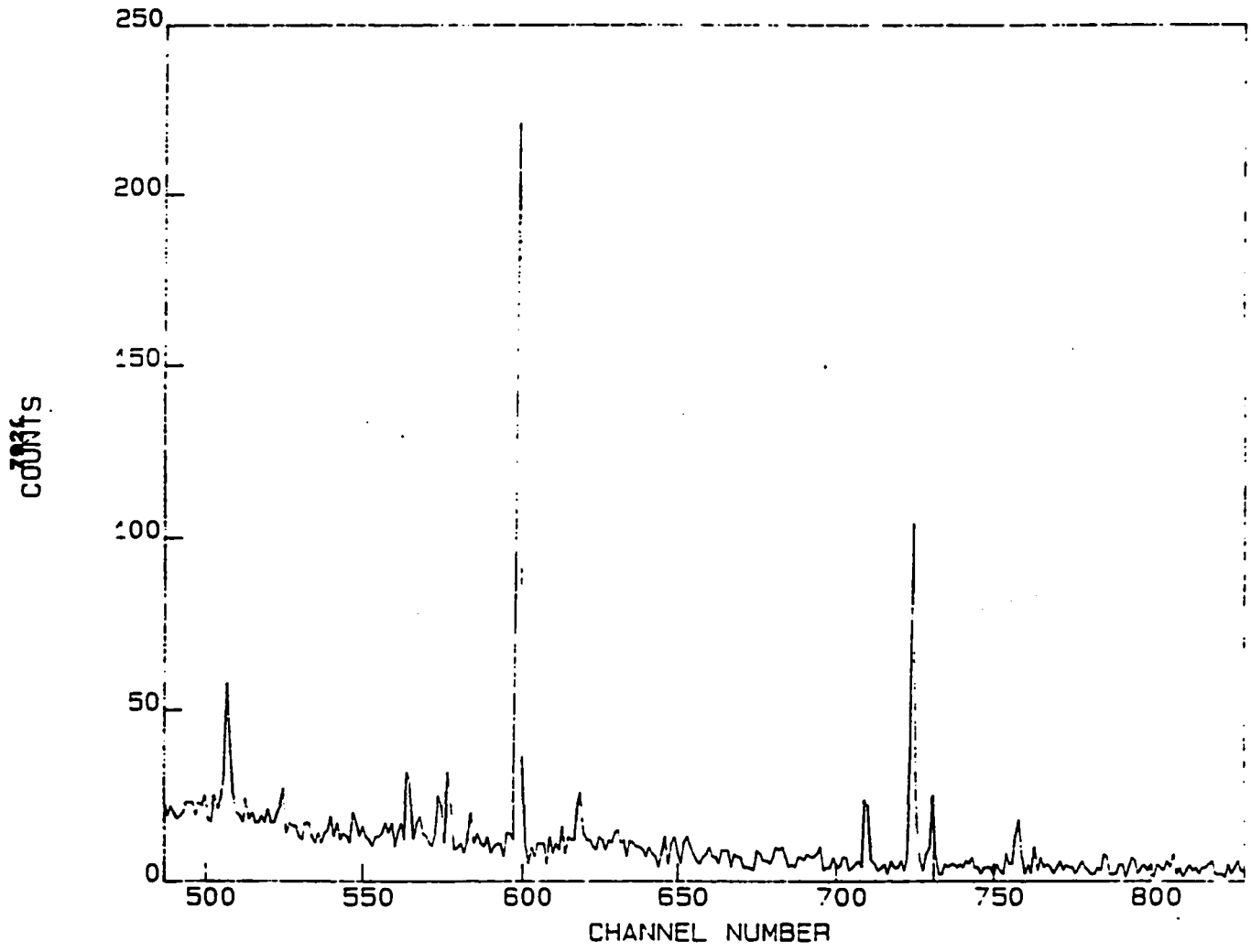

Fig. 2.21. Gamma rays yield spectrum for Al(p,γ) reaction at E_p = 220 keV.

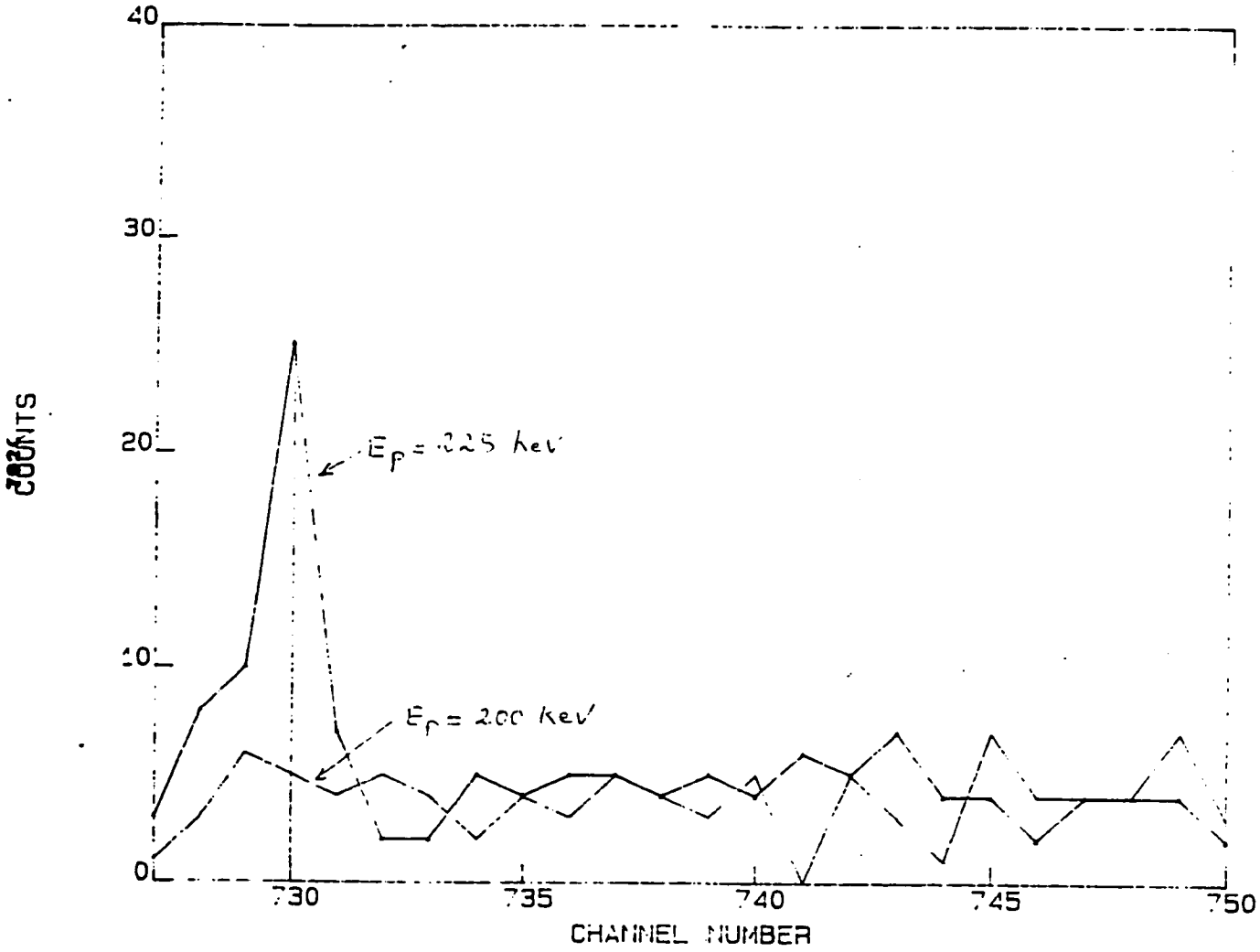

Fig. 2.22. Gamma rays spectra for 200 and 225 keV proton energies.

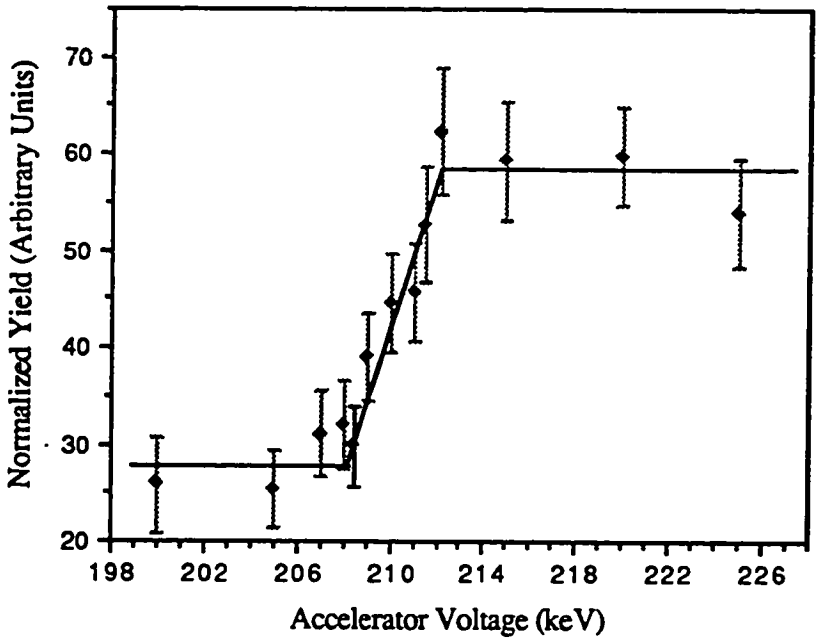

Fig. 2.23. Gamma rays yields for 200 to 225 keV protons.

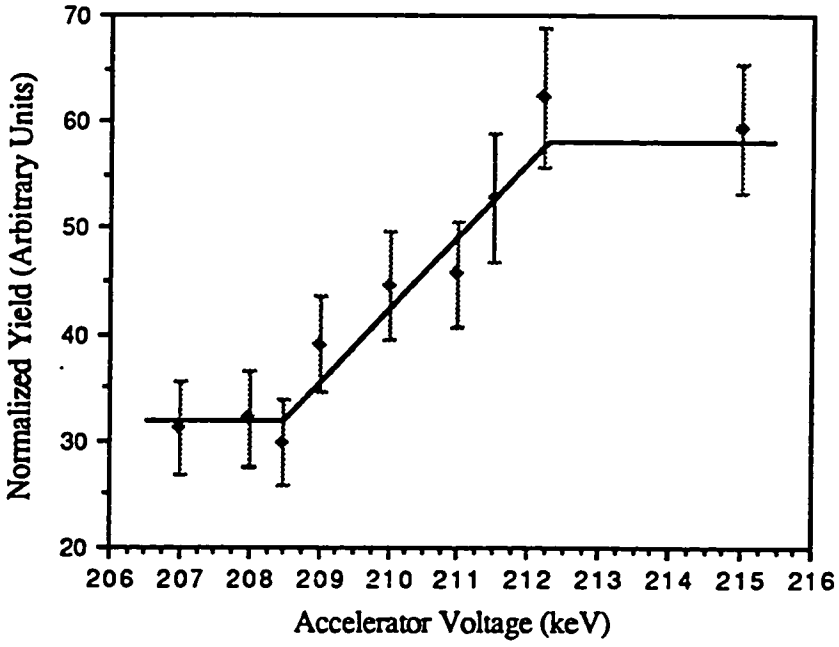

Fig. 2.24. Gamma rays yields for 207 to 215 keV protons.

each other. This figure shows higher yield of gamma rays at 225 keV.

Gamma rays yield per micro coulomb was calculated for all proton energies. Fig. 2.23 shows normalized yield as a function of proton energy ranging from 200 to 225 keV. This figure shows two plateu regions one above 212 keV and the other below 208 keV. Between 208 and 212 keV, yield increases showing a resonace. In fig. 2.24 the normalized yield is shown on enlarged scale for 207 to 215 keV protons. From there, it is quite obvious that 223 keV resonance occurs at 210.5±1.0 keV reading of the accelerator voltmeter. This study shows that voltmeter reading at 210 keV is 12.5 keV higher than the actual beam energy. In order to have accelerator energy calibration scheme, one needs to check the accelerator energy at one more energy point. Therefore in the following, the deuteron energy is assumed to be the readout of the accelerator voltmeter.

2.9 Energy Calibration of the SSB Detectors

For light ions such as protons or alpha particles, the pulse height of SSB detector is linearly proportional to the total energy deposited in the detector. The energy calibration obtained from protons is very close (less than 1%) to that obtained from alpha particles. Usually, SSB detectors are calibrated using alpha particle sources. It is desired to have an alpha source with two or more discrete energy for energy calibration of SSB detector[17].

2.9.1 Energy Calibration Source

A Mixed Alpha Source containing ^{239}Pu ,^{241}Am and ^{244}Cm was used to calibrate the detectors. Table 2.1 shows energies and relative intensity of alpha lines.

Table 2.1. The energies and intensities of the alpha particles calibration source.[28]

Element	Alpha particle energies (MeV)	Relative intensity
^{239}Pu	5.156	0.73
	5.143	0.15
	5.105	0.12
^{241}Am	5.486	0.86
	5.443	0.13
^{244}Cm	5.806	0.77
	5.783	0.23

The energy differences between the intense lines from ^{239}Pu ,^{241}Am and ^{244}Cm are 0.43 and 0.32 MeV respectively. The channel separation between these peaks can also be used for energy calibration. The mixed nuclei source was evaporated on a stainless steel disc.

2.9.2 Detector Bias Voltage

As per manufacturer manual, an EG&G Ortec Silicon Surface Barrier Detector Model BA-16-100-100 needs to be operated at a bias of 100 volts across the detector. The voltage is applied by a detector control unit through the preamplifier. The voltage readout at the control unit is the sum of the potential drop across the preamplifier and the detector. The resistance of the preamplifier is about 100 MΩ and even a small leakage current of 0.1 μA results in a potential drop of about 10 V across the preamplifier. It is desired to measure the preamplifier resistance accurately so that the 100 V bias may be applied across the detector. In order to measure the preamplifier resistance, the signal input of the preamplifier was terminated with a 50 Ω terminator. Then the leakage current of the detector control unit was read as a function of bias voltage. The slope of the plot of the bias voltage versus leakage current gave the resistance of the preamplifier. Fig 2.26 shows the bias voltage versus the leakage current for all four preamplifiers. The measured resistances of the preamplifiers were found to be 131, 133, 134 and 138 MΩ

2.9.3 Pulse Height Calibration

In order to calibrate the detector the alpha source disc was directly mounted on the detector collimator. Fig. 2.25 shows an alpha energy calibration spectrum of a SSB detector. The detector has such an excellent resolution that it can resolve the low intensity line from the high intensity

line of ^{244}Cm which has an energy difference of 23 keV only. As per manufacturer, the quoted energy resolution (FWHM) of SSB detector is 16 keV for 5.49 MeV alphas from ^{241}Am. The measured 17±3 keV energy resolution (FWHM) for 5.486 MeV alpha line is in agreement with the quoted value.

As mentioned in the previous section, a 5 μm aluminum foil is inserted in front of each detector to suppress elastically scattered deuterons. Fig. 2.27 shows energy calibration spectrum with and without aluminum foil. Due to the energy loss of the alpha particles, the three alpha lines have shifted towards lower energies. The energy shift in each line, which is proportional to the energy loss of alpha particle, is a good measure of the thickness of the foil. The aluminum foil in front of the detector deteriorates the measured energy resolution of the detector. The energy resolution of the detector with the foil is measured to be 150 keV for 5.49 MeV alphas from ^{241}Am. Since in this experiment, the proton peak is well separated and has almost zero background the poor energy resolution is not critical. Also an accurate detector energy calibration is not needed in this experiment since only a single proton peak appears in the spectrum.

As mentioned earlier, the thickness of the aluminum foil can be calculated from the measured energy loss of the alpha particles in the foil. As shown in table 2.2, the energy loss of the alpha particles with energies 5.156, 5.456 and 5.806 MeV in the aluminum foil is measured to be 1.008, 0.966 and 0.917 MeV respectively. The thickness of the foil was determined

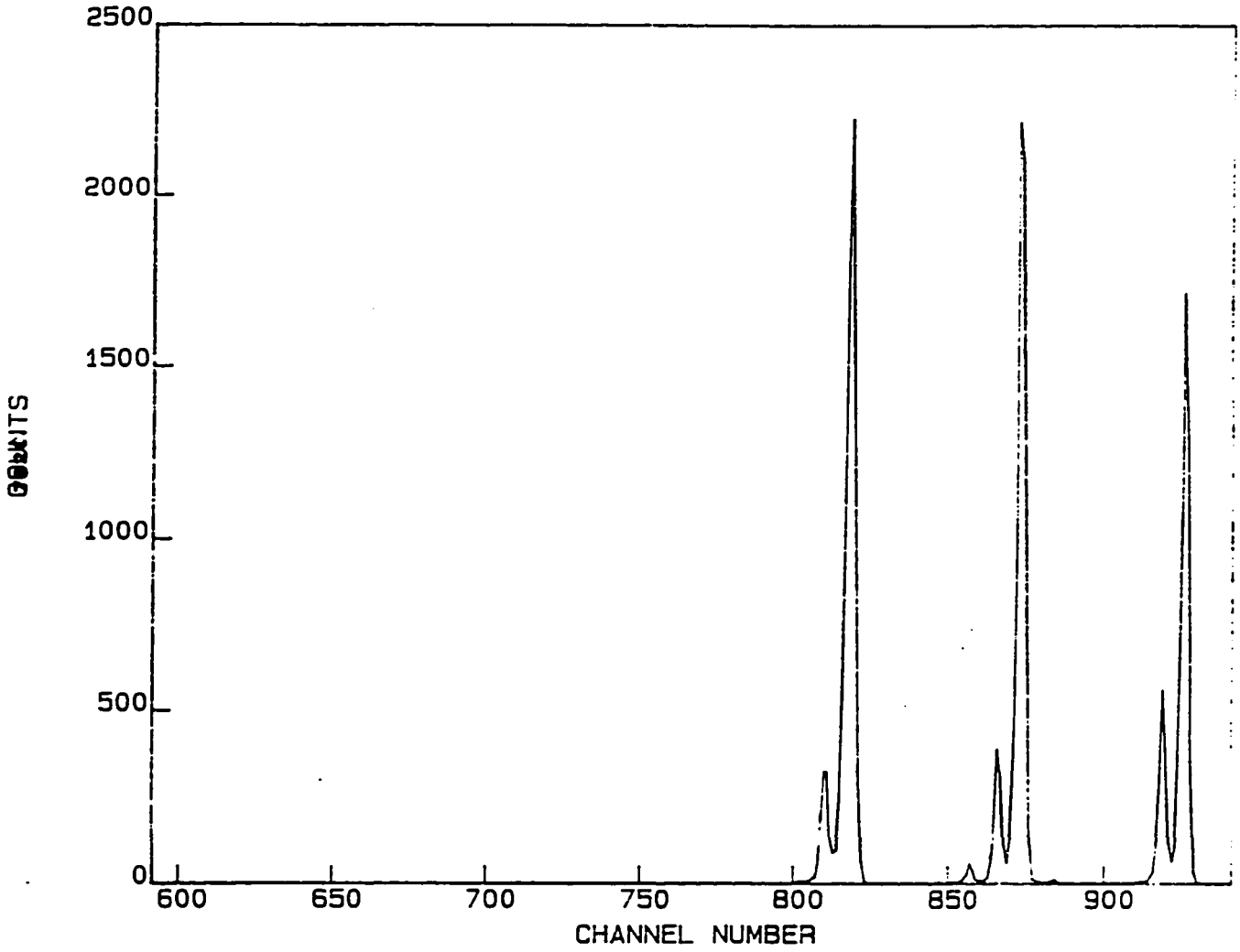

Fig. 2.25. Energy calibration spectrum of a SSB detector.

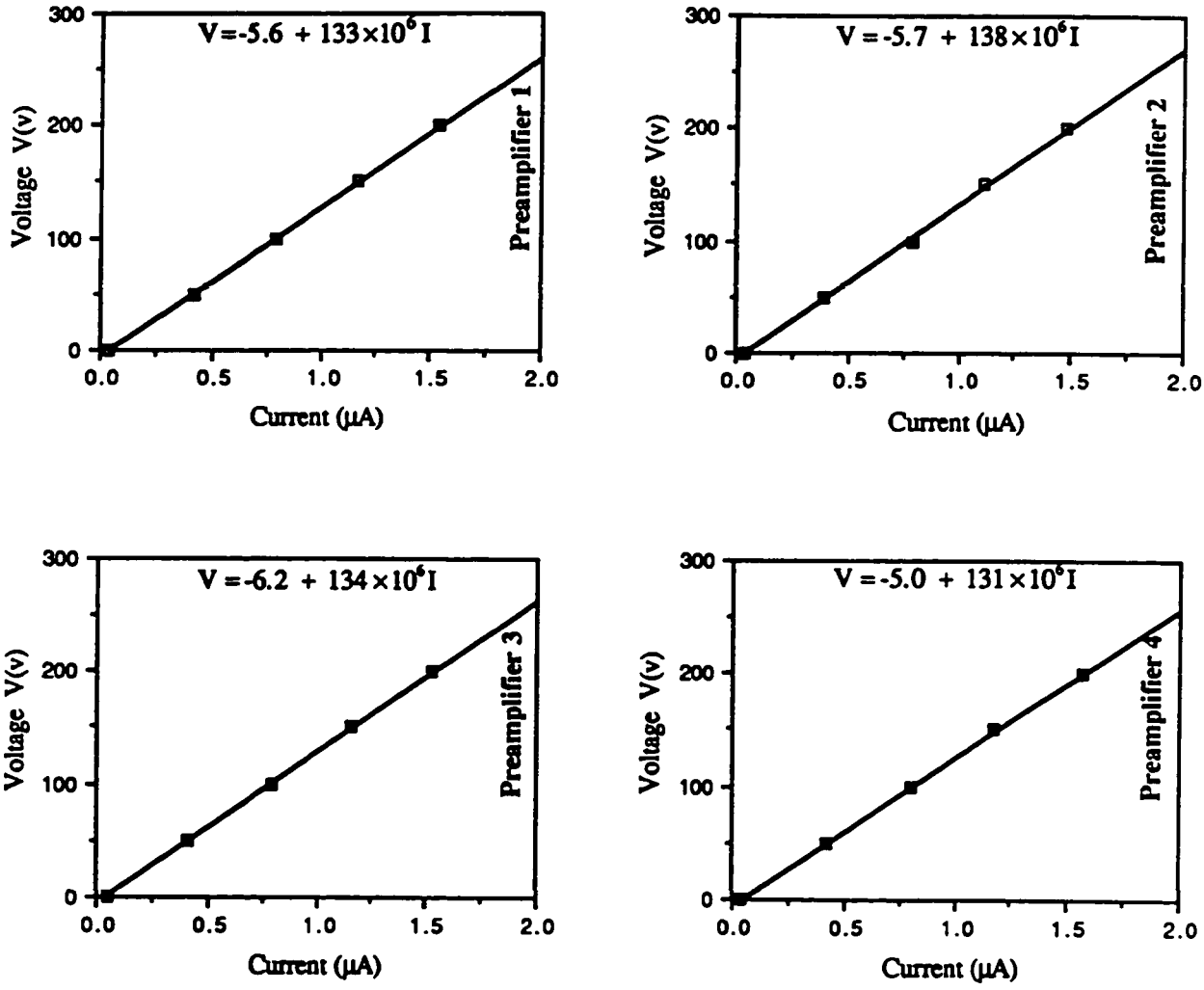

Fig. 2.26. Bias voltage versus leakage current for the four preamplifiers.

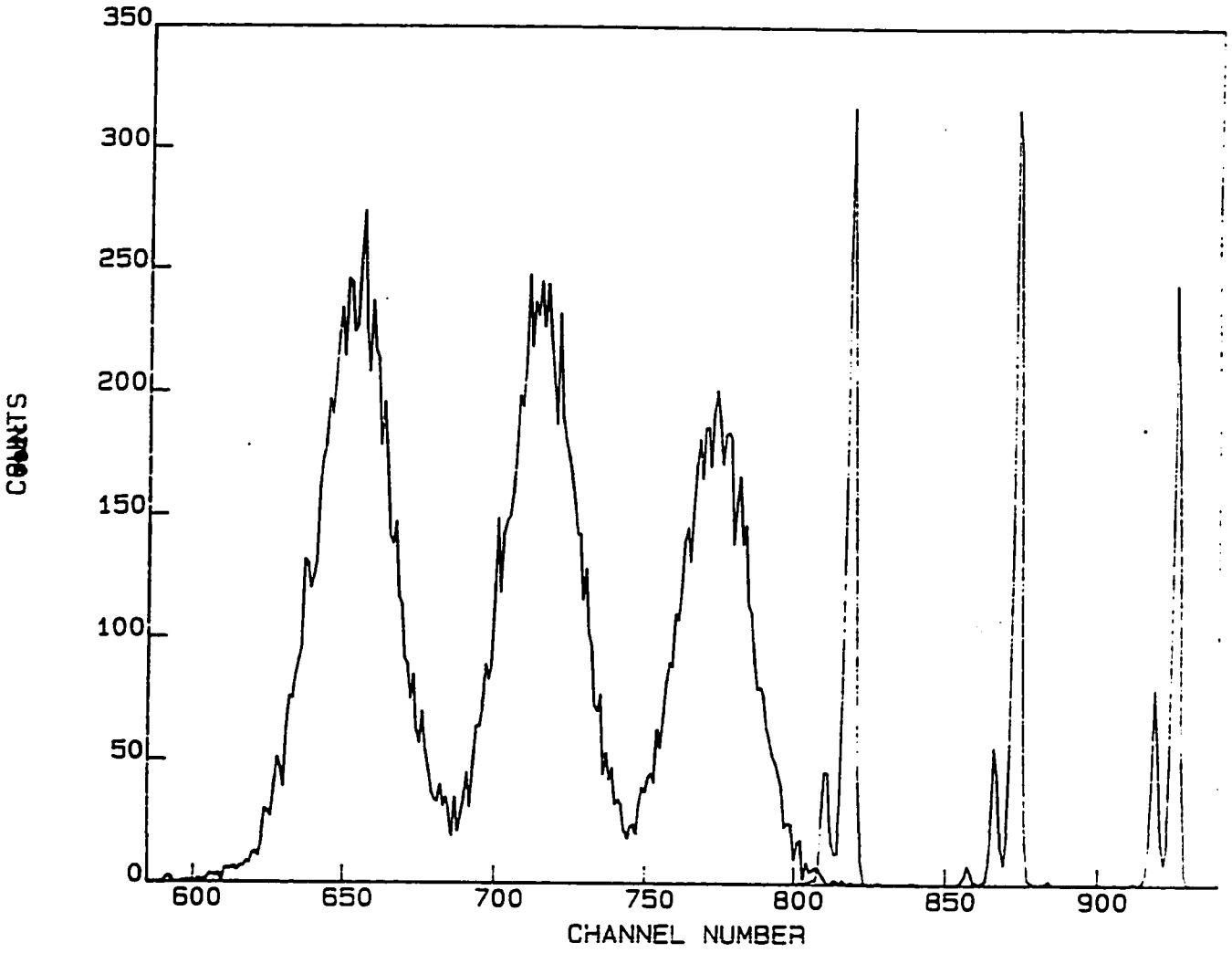

Fig. 2.27. Detector energy spectrum of the mixed alpha source with and without aluminum foil.

by comparing the measured energy loss with the calculated energy loss. The computer code TRIM was used to calculate the energy loss in steps of 0.1 μm for aluminum foils with thickness ranging from 5 to 6 μm. The details of comparison, the calculated energy loss for aluminum foil with thicknesses of 5.7, 5.8, 5.9 and 6.0 μm are included in table 2.2. It is obvious from the table that the measured energy loss agrees, within the experimental uncertainties, with the calculated energy loss of the foil with 5.8 as well as 5.9 μm thickness. The calculated thickness is different than the quoted thickness of 5.0 μm of the aluminum since the uncertainty in our calculation is only 0.1 μm.

Table 2.2. Measured and calculated energy loss of alpha particles in aluminum foil

Alpha particles energy without Al foil (MeV)	5.156	5.486	5.806
Alpha particles energy with Al foil (MeV)	4.148 ±0.012	4.518 ±0.012	4.883 ±0.012
Measured energy loss of alpha particles in the foil (MeV)	1.008 ±0.012	0.968 ±0.012	0.923 ±0.012
Calculated energy loss of alpha particles in 5.7 μm. thick Al foil (MeV)	0.982	0.938	0.890
Calculated energy loss of alpha particles in 5.8 μm. thick Al foil (MeV)	1.000	0.956	0.917
Calculated energy loss of alpha particles in 5.9 μm. thick Al foil (MeV)	1.019	0.973	0.933
Calculated energy loss of alpha particles in 6.0 μm. thick Al foil (MeV)	1.037	0.991	0.950

2.10 The Measurements of Excitation Functions and Angular Distributions of the $^{12}C(d,p)$ Reaction

Excitation functions and angular distributions require measurements of reaction yields at different energies and angles. From the earlier study of Al(p,γ) reaction, carbon buildup was observed. The carbon buildup changes the target thickness in $^{12}C(d,p)$ reaction which results in a false yield. In order to study the carbon buildup, the proton yield of $^{12}C(d,p)$ reaction from 220 keV deuteron was measured repeatedly at 140 degree for a fixed 0.01 coulomb accumulative charge at the faraday cup. The 0.01 coulomb charge corresponds to 6.25×10^{16} incident deuterons on the target. Fig. 2.28 shows proton yield as a function of accumulative charge on the faraday cup. This fixed accumulative charge were chosen to get statistical uncertainty in proton yield at 140 degree less than 3%. The increase in proton yield with number of incident charge is due to carbon buildup. As the longer exposure of thin carbon foil to the beam results in rupture of the foil, it was difficult to estimate the carbon buildup rate which can be used later on for buildup correction. Another way of correcting the carbon buildup is to compare the yield of a fresh target with the yield of the same target with carbon buildup at the same deuteron energy and angle. The ratio of these two yields gives the carbon buildup correction factor for the next run. In this experiment, proton yield was measured at 140 degree with 220 keV deuteron repeatedly in between excitation function and angular distribution measurements for carbon buildup correction.

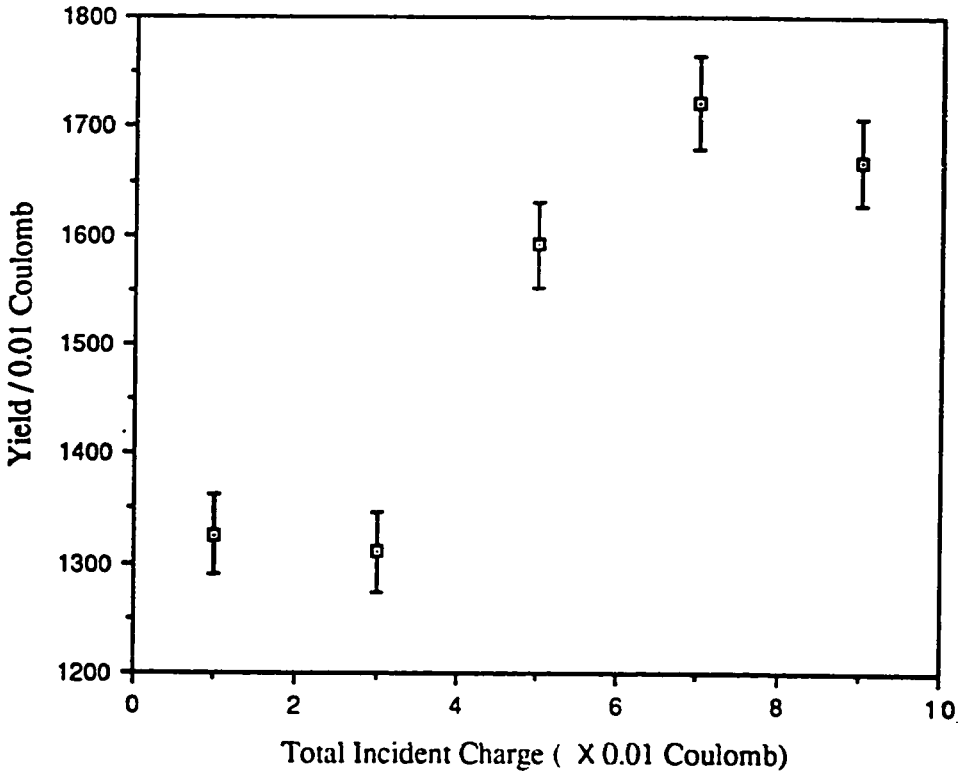

Fig. 2.28. Proton yield as a function of accumulative charge on the faraday cup.

In this experiment, excitation functions were measured at 25, 35, 90 and 140 degrees over deuteron energies ranging from 160 to 300 keV in 10 keV steps for a fixed charge measured at the faraday cup . Due to higher yields at energies above 250 keV, the fixed charge was chosen to be half of that below 260 keV. For deuteron energy 180 to 250 keV, a preset charge of 0.01 coulomb gave proton yield at 140 degree with 12 to 1.6 % statistical uncertainty. For deuteron energies above 250 keV, the proton yield was measured for a preset charge of 0.005 coulomb which resulted in statistical uncertainty of 1.3 to 1.8 % at 140 degree. Proton yield at 220 keV deuteron energy was measured for fresh target and was repeated before every energy change. From this data, fresh target yields for 160 to 300 keV deuterons were calculated.

Angular distributions were measured at 13 angles from 20 to 160 degrees in 10 degrees steps at 200, 220, 250, 280 and 300 keV deuteron energies. Having four detectors only, the 13 angles were covered in four groups in which three of the detectors covered different angles while the fourth was fixed at 140 degree which was later used for normalization. Carbon buildup factor could be obtained by comparing the raw yield at 140 degree with the fresh target yield calculated in excitation function measurement at the same angle and energy. An additional 220 keV yield measurement is not needed before each measurement. For each group of detectors angles, angular distributions were measured for all five energies without opening the chamber and changing the target. In order to view the target by the detectors at various angles, the target was placed at 70, 90 and

110 degrees with respect to beam axis. After each run the spectra of the four detectors were written on a disc on the VAX 11/785 computer for off-line analysis.

CHAPTER 3

DATA REDUCTION

Data analysis was carried out using XSYS system on VAX 11/785 computer. In data analysis, the detector spectra were stripped, corrected for carbon buildup and finally normalized. In the following these steps are described.

3.1 Data Stripping

In data stripping each detector spectrum was analyzed individually. For all angles the proton peak had almost no background. No contribution from D(d,p) reaction protons was observed in the spectrum. Even if it was there, the proton from D(d,p) reaction has higher energy than the proton from $^{12}C(d,p)$ reaction. In Appendix D, the proton energies from $^{12}C(d,p)$ and D(d,p) have been tabulated for deuteron energies ranging from 200 to 300 keV in steps of 20 degrees. Fig. 3.1 and fig. 3.2 show proton yield spectra at 110 and 160 degrees for 200 keV deuterons while fig. 3.3 and fig. 3.4 show proton yield spectra at 100 and 160 degrees for 300 keV deuterons. The spectra for 300 keV were acquired for a preset of 0.005 coulomb while 180 and 250 keV spectra were acquired for 0.01 coulomb. Fig.3.5 shows the proton peak measured at 100 degree for 300 keV deuterons. The width

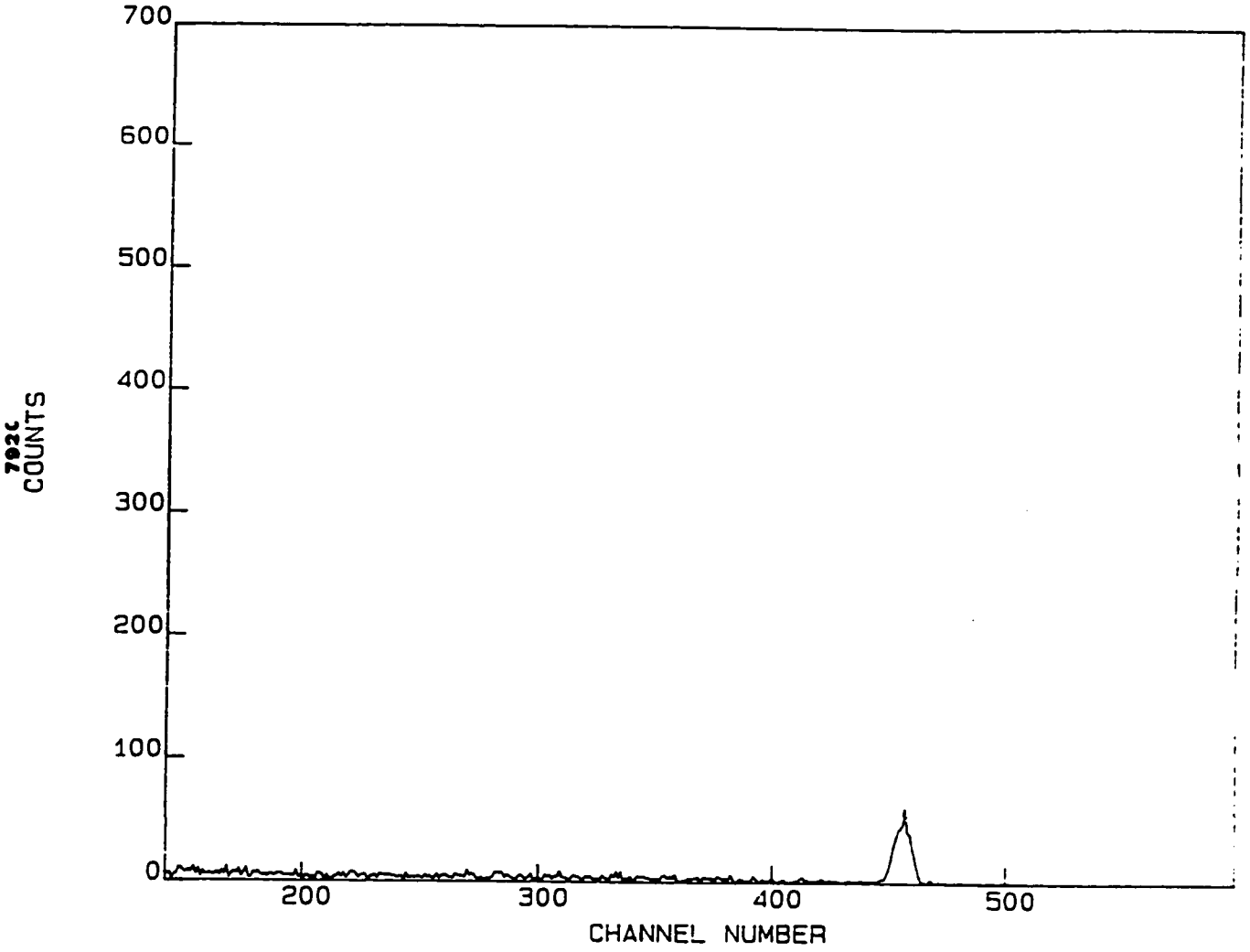

Fig. 3.1. Proton yield spectrum from $^{12}C(d,p)$ reaction with 200 keV deuteron at 110 degree.

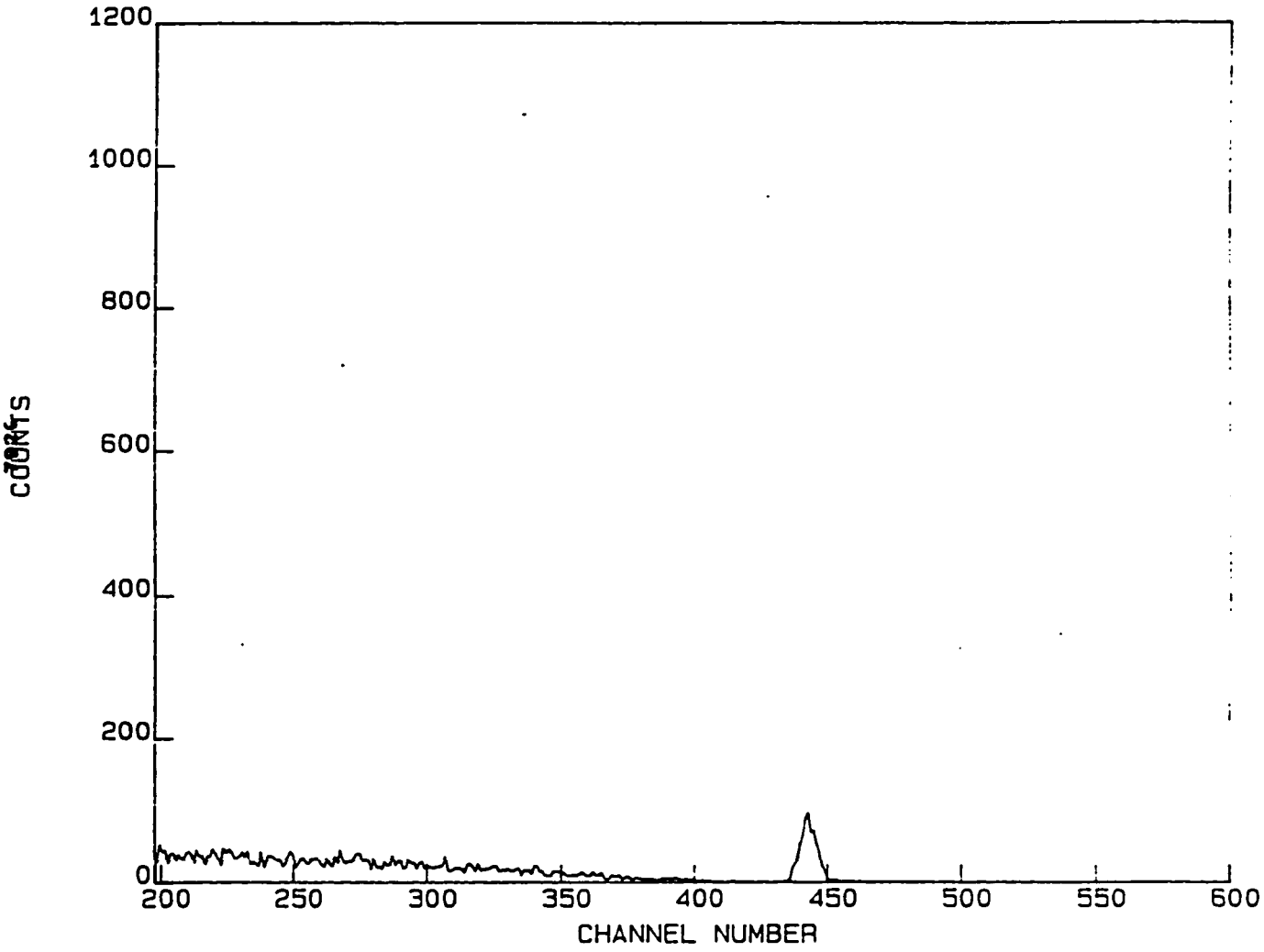

Fig. 3.2. Proton yield spectrum from $^{12}C(d,p)$ reaction with 200 keV deuteron at 160 degree.

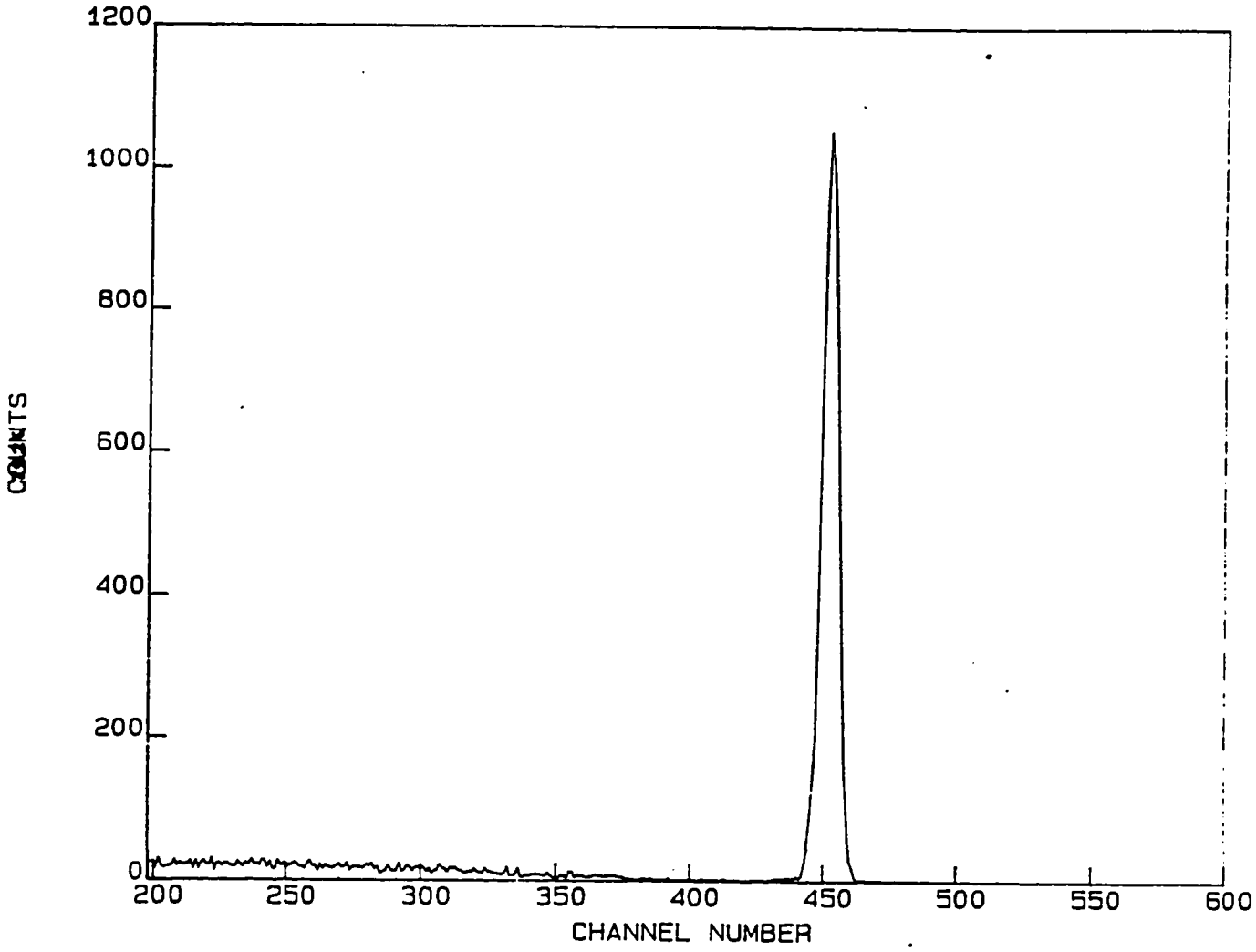

Fig. 3.3. Proton yield spectrum from $^{12}C(d,p)$ reaction with 300 keV deuteron at 100 degree.

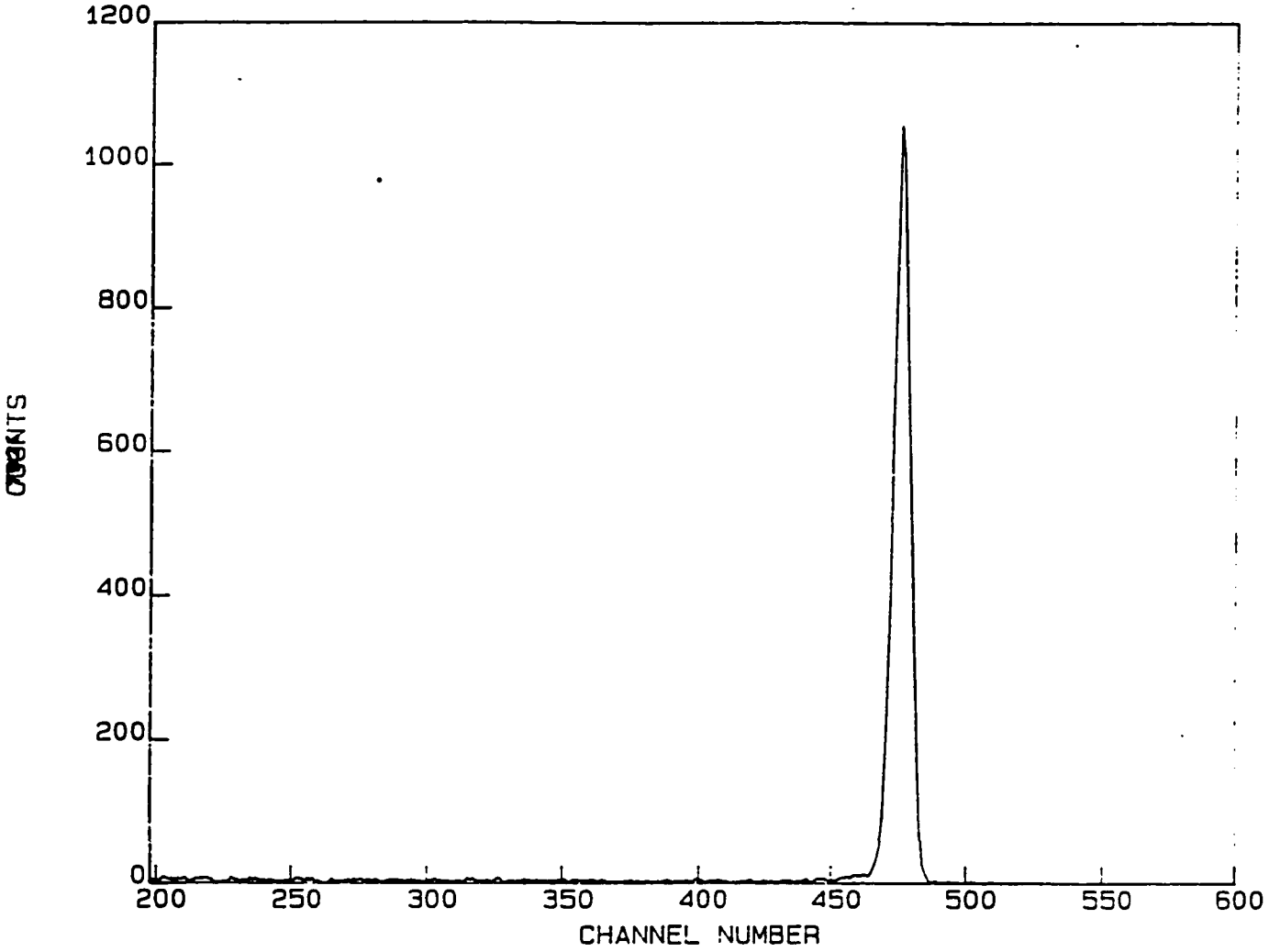

Fig. 3.4. Proton yield spectrum from $^{12}C(d,p)$ reaction with 300 keV deuteron at 160 degree.

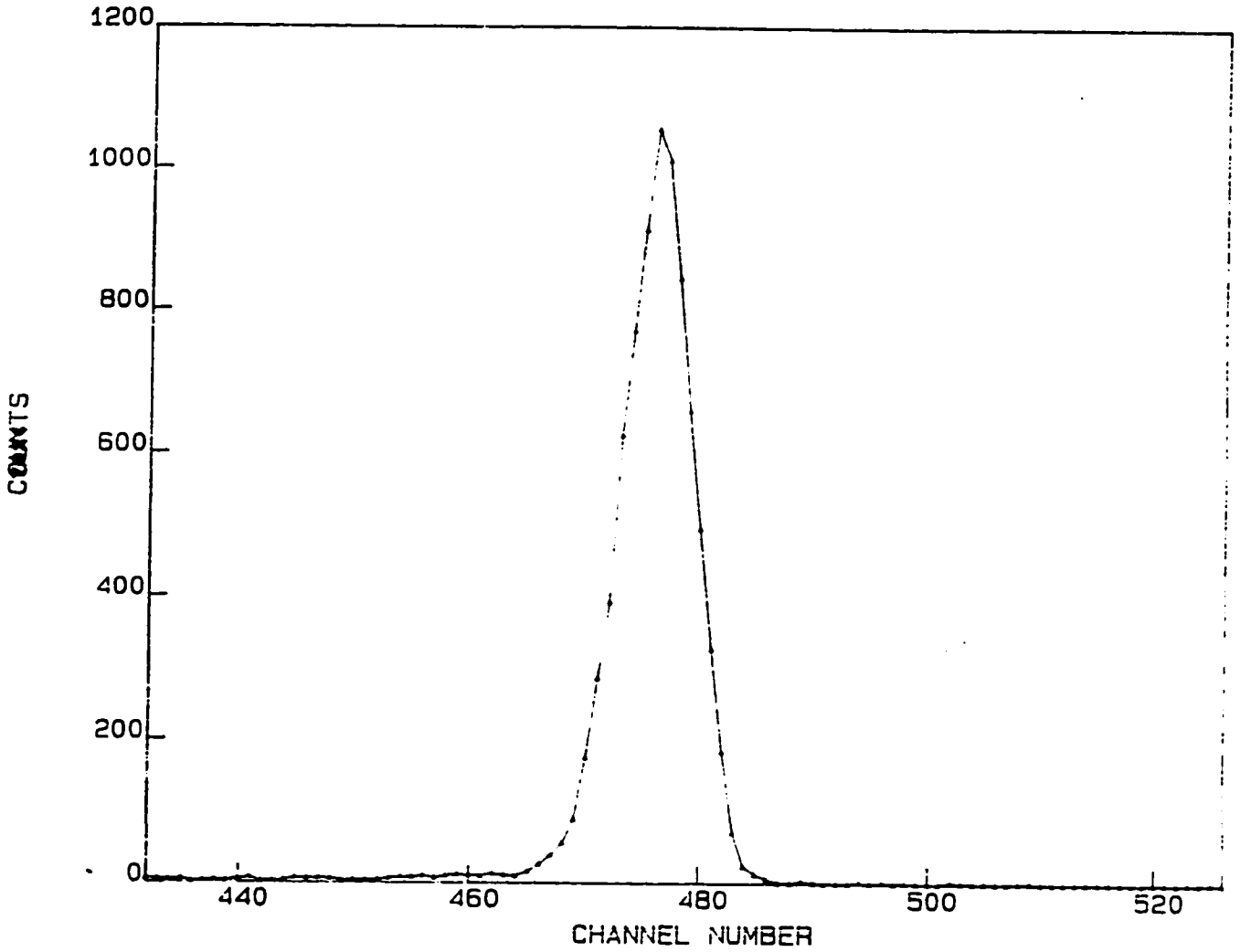

Fig. 3.5. Proton peak from $^{12}C(d,p)$ reaction with 300 keV deuteron at 100 degree.

(FWHM) of this peak was measured to be 40 keV which is consistent with the energy loss calculation in the carbon and in the aluminum foils.

The integrated counts under each proton peak was measured by setting a gate on the peak. As the proton peak had practically no background, the gate limits were not critical. Then the integrated yield was corrected for carbon buildup as described in the following section.

3.2 Carbon Buildup Correction

The integrated proton yields at all angles and energies were corrected for carbon buildup. The carbon buildup on the target, increases effective thickness of the target[28,29,30]. As a result of this, the used target yield at a given deuteron energy is greater than the yield of the fresh at the same energy. The ratio of the two yields gives the carbon buildup correction factor for the used target yield. As mentioned earlier, the 220 keV yield data at 140 degree, which was taken with a fresh target and also before every energy change, can be used to calculate the carbon buildup correction factor. The 140 degree angle was chosen due to its higher yield. This factor was used to normalize the yield to the yield of a target which is not truly fresh but already exposed to 6.25×10^{16} deuterons. This exposure has increased the thickness of the target and has introduced a systematic error in the target thickness which will be discussed later.

If $Y(E, \theta, i)$ is the yield at angle θ with deuteron energy E and run

number i, then carbon buildup correction factor R(i-1) is given by

$$R(i\text{-}1) = \frac{Y(220, 140, \text{fresh})}{Y(220, 140, i\text{-}1)} \qquad (3.1)$$

where Y(220, 140, fresh) is the yield of a fresh target at 140 degree with 220 keV deuterons while Y(220, 140, i-1) is the repeated yield at the same energy and angle before the run i which is needed to be corrected. The corrected yield C(E, θ, i) for the measured yield Y(E, θ, i) is given by

$$C(E, \theta, i) = Y(E, \theta, i)\, R(i\text{-}1) \qquad (3.2).$$

It is assumed that all yields are normalized to the same integrated charge. The Y(220, 140, fresh) was calculated from the average value of 6 fresh target yields.

3.3 Data Normalization

As mentioned in section 2.10, the 13 angles of each angular distribution were covered in four groups. Therefore, detector angles were changed four times for each angular distribution measurement. When the detector angles were changed, the target was also changed due the fact that carbon foils were ruptured during venting the chamber. Since the targets may have different thicknesses within the four groups of an angular distribution measurements, it was required to adjust the yield of all four groups with respect to a fixed detector yield common in all groups. The

yield Y(E, 140, i) was used to adjust the yield of all four groups.

The adjusted yield $C_A(E, \theta, ij)$ was calculated using the following relation

$$C_A(E, \theta, ij) = Y(E, \theta, i)\frac{Y(E, 140, j)}{Y(E, 140, i)} \qquad (3.3)$$

where Y(E, 140, j) was the yield of the 140 degree detector of a group with respect to which the yields of other three groups has to be adjusted. As one group of angles was common in excitation functions and angular distributions measurements, this group was taken as the reference group. If Y(E, 140, j) in eq. 3.3 is replaced by the fresh target yield at the same energy C(E,140, j), one can adjust the yield and correct for carbon buildup in one step. Thus the adjusted and the carbon buildup corrected yield $C_{AC}(E, \theta, ij)$ is given by the following relation

$$C_{AC}(E, \theta, ij) = Y(E, \theta, i)\frac{Y(E, 140, j)}{Y(E, 140, i)}\ \frac{Y(220,140,fresh)}{Y(220,140,j-1)} \qquad (3.4).$$

As explained earlier, the factor $\frac{Y(E, 140, j)}{Y(E, 140, i)}$ adjusts the yield while the factor $\frac{Y(220,140,fresh)}{Y(220,140,j-1)}$ corrects for carbon buildup.

Fig. 3.6 shows excitation functions for the 25, 35, 90 and 140 degrees detectors. The excitation functions at 50, 100 and 160 degrees, which were derived from angular distribution data, are also shown in fig. 3.7. The

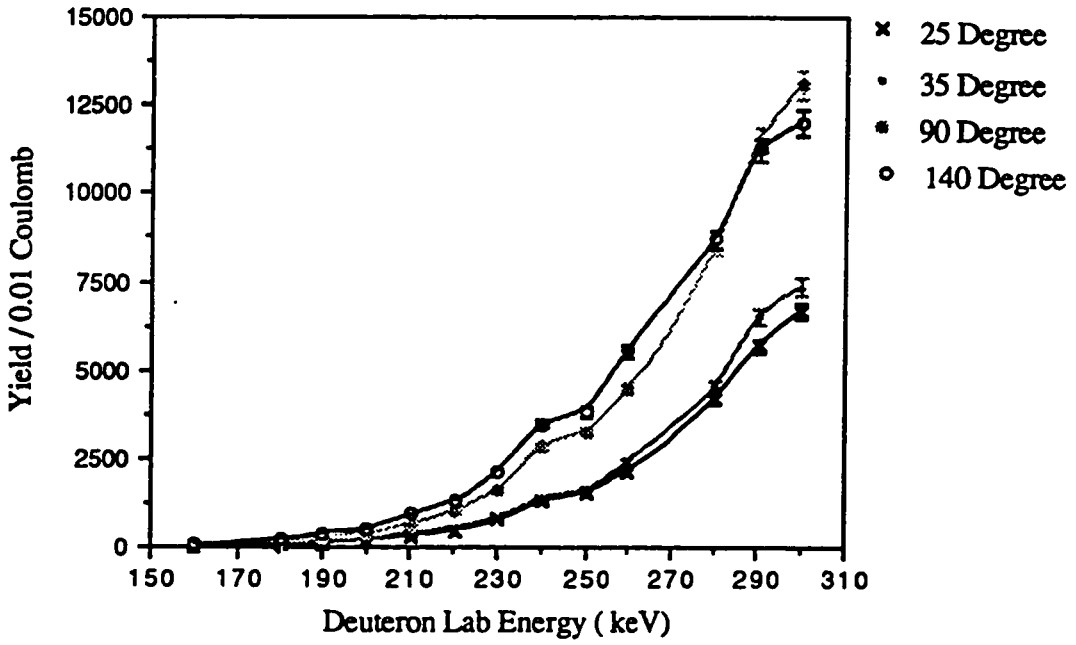

Fig. 3.6. Excitation functions of $^{12}C(d,p)$ reaction at 25, 35, 90 and 140 degrees. Lines are drawn to show the trend of the excitation functions. Only statistical errors are plotted.

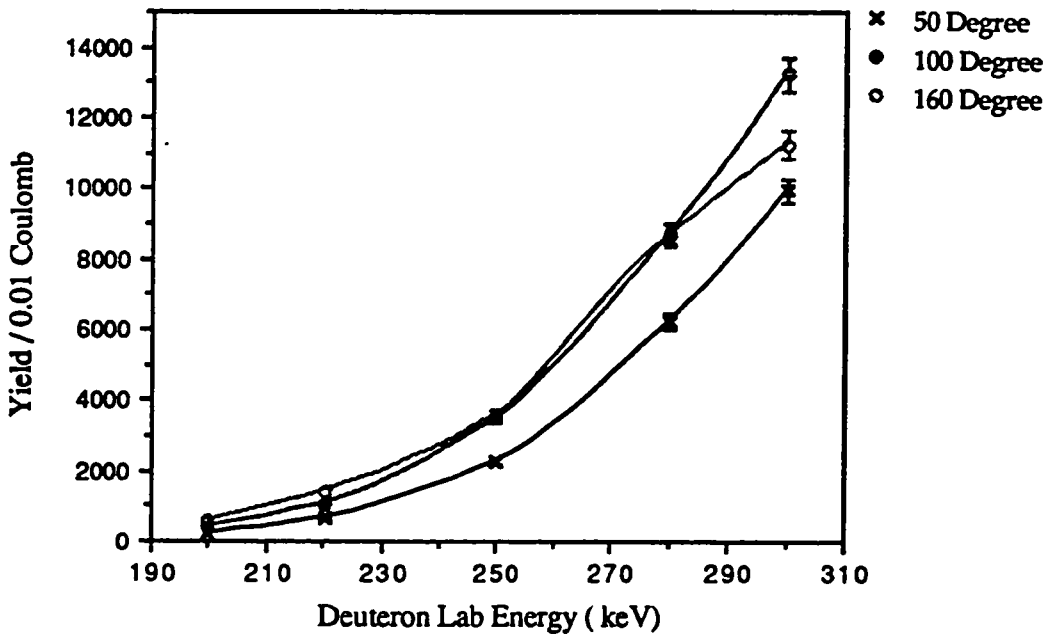

Fig. 3.7. Excitation functions of $^{12}C(d,p)$ reaction at 50, 100 and 160 degrees. Lines are drawn to show the trend of the excitation functions. Only statistical errors are plotted.

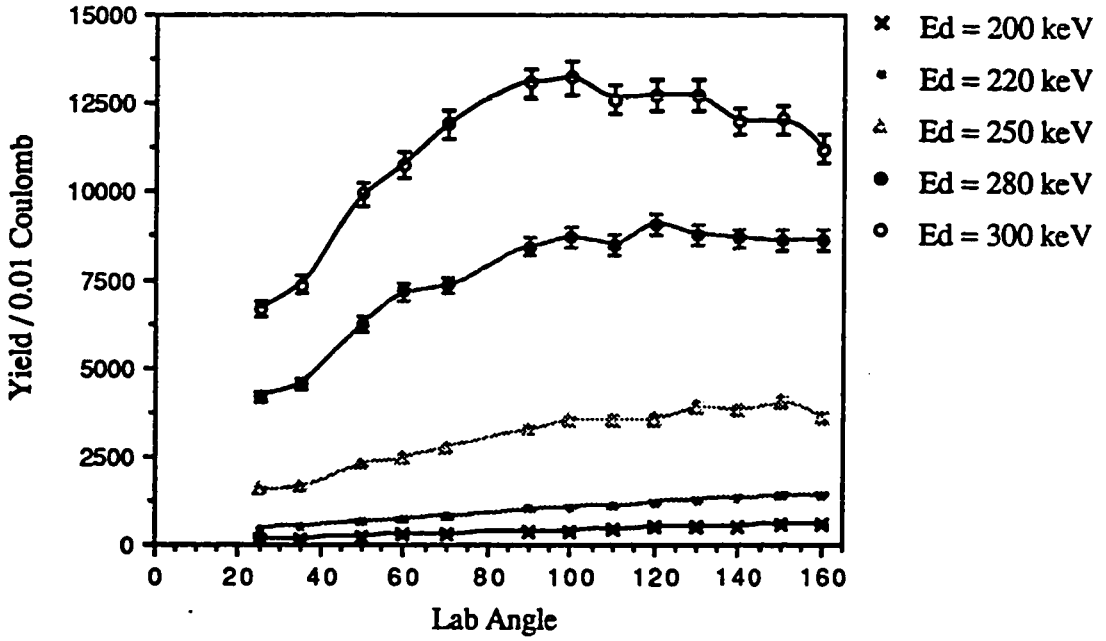

Fig. 3.8. Angular distributions of $^{12}C(d,p)$ reaction at 200, 220, 250, 280 and 300 keV deuteron energies. Lines are drawn to show the trend of the angular distributions. Only statistical errors are plotted.

angular distributions for deuteron energies 200, 220, 250, 280 and 300 keV are shown in fig. 3.8.

Then the differential cross section $\frac{d\sigma(E,\theta)}{d\Omega}$ for $^{12}C(d,p)$ reaction at deuteron energy E and at reaction angle θ, was calculated from the yields $C_{AC}(E, \theta, ij)$ using the following relation[31]

$$\frac{d\sigma(E,\theta)}{d\Omega} = \frac{C_{AC}(E, \theta, ij)}{I\ nt\ \Delta\ \Omega} \qquad (3.5)$$

where I is the total number of incident particles which was 6.25×10^{16} deuterons, nt is the number of target nuclei per unit area which was 1.01×10^{18} carbon nuclei per cm^2 (target thickness was 20.2 $\mu g/cm^2$) and $\Delta\Omega$ is the solid angle suspended by the detector which was 1.14 mster. In appendix A, excitation functions and angular distributions data are listed. It is also listed there the total error associated with these data. Calculations of these errors are described in the following section.

3.5 Error Analysis

The data have statistical as well as systematic errors. In the following, they will be discussed separately.

3.5.1 Statistical Errors

Considering only the statistical error, the fresh target yield C(E, θ, i)

given by eq. 3.2 has uncertainty $\Delta C(E, \theta, ij)$ given by

$$\Delta C(E, \theta, ij) = C(E, \theta, ij) \sqrt{\frac{1}{Y(E, \theta, i)} + \frac{1}{Y(220, 140, fresh)} + \frac{1}{Y(220, 140, i-1)}} \quad (3.6).$$

Similarly, the statistical uncertainty $\Delta C_{AC}(E, \theta, ij)$ associated with the adjusted and corrected yield $C_{AC}(E, \theta, ij)$ can be calculated[17] from eq. 3.4 to be

$$\Delta C_{AC}(E, \theta, i) = C_{AC}(E, \theta, i) \sqrt{\frac{1}{Y(E, \theta, i)} + \frac{1}{Y(E, 140, i)} + \frac{1}{(C(E, 140, j))^2}} \quad (3.7).$$

Tables 3.1 and 3.2 shows calculated statistical uncertainties in excitation functions and angular distributions.

Table 3.1. Statistical uncertainties in excitation functions.

Angle	Uncertainty(%)
25	3-13
35	3-12
90	3-9
140	3-8

Table 3.2. Statistical uncertainties in angular distributions.

E_d(keV)	Uncertainty(%)
200	5-9
220	1-5
250	3-4
280	3
300	3

3.5.2 Systematic Errors

The systematic errors arise from the uncertainties in the charge integration, the fresh target thickness, the finite angular resolution and the carbon buildup correction. The systematic error due to the uncertainties in the charge integration and the target thickness was estimated from the average value and the standard deviation of four repeated measurements with the fresh target at 220 keV deuteron energy. The systematic error σ_{sys} was calculated using this formula

$$\sigma_m^2 = \sqrt{\sigma_{sys}^2 + \sigma_{stat}^2} \tag{3.8}$$

where σ_m is the measured standard deviation of the four measurements while σ_{stat} is the statistical error given by

$$\sigma_{stat} = \sqrt{\frac{\text{average value}}{4}} \tag{3.9}$$

The systematic error due to the charge integration and the fresh target thickness was estimated to be 3%. The spread due to finite aperture of the detector was 0.5 degree. This 0.5 degree may result at the most of 0.5% error in the yield measurement. This error was calculated from the steepest part of the yield curve at 300 keV. Finally the systematic error due to carbon buildup correction was estimated from the average carbon buildup rate per 6.25×10^{16} deuterons from 220 keV data. This average rate was estimated by dividing the difference between the yield of the fresh target and that of the last 220 keV run with the same target by the total number of runs of 6.25×10^{16} incident deuterons. Therefore the fresh target yield has uncertainty by an amount of this average carbon buildup rate per 6.25×10^{16} incident deuterons. The upper limit of this systematic error was calculated to be 3%. The total systematic error is then less than 4%.

Table 3.3. Sources of systematic errors along with their values.

Source of systematic error	Upper Value (%)
Charge integration and target thickness	3
Carbon buildup correction	3
Finite aperture	0.5
Total	**4**

CHAPTER 4

RESULTS AND DISCUSSION

The measured excitation functions and differential cross sections of $^{12}C(d,p)$ reaction will be discussed and later on will be compared with presently available data.

4.1 Excitation Functions

Figs. 4.1 to 4.4 show the excitation functions for $^{12}C(d.p)$ reaction for deuteron energies ranging from 160 to 300 keV in steps of 10 keV. All these figures contains only statistical uncertainties. For 25 and 35 degrees excitation functions, the statistical uncertainties range from 3-13 % while for 90 and 140 degrees it is 3-9 %. Excitation functions at lab angles 25, 35, 90, 140 and 160 degrees are shown in fig. 4.1. The cross section shows a smoothly increasing trend with deuteron energy. The cross section does not show any resonance structure but a broad hump around 240 keV deuteron energy which is more pronounced for 90 and 140 degrees excitation functions. The rate of increase of cross section with deuteron energy is different for different angles. The rate of increase for 90 and 140 degrees is higher than that of 25 and 35 degrees.

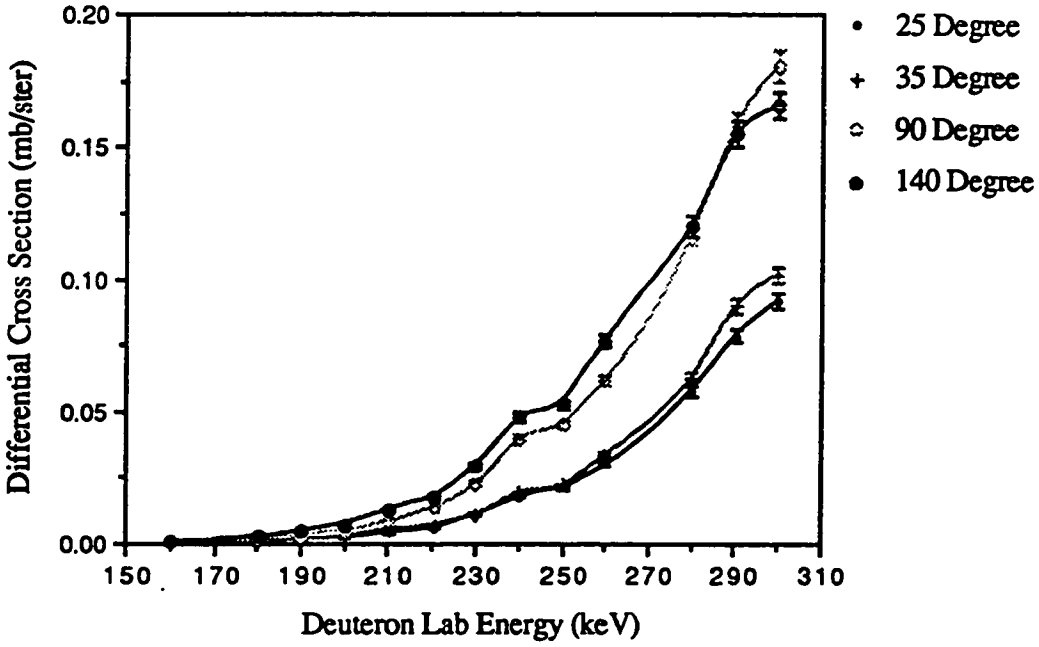

Fig. 4.1. Excitation functions of $^{12}C(d,p)$ reaction at 25, 35, 90 and 140 degrees over 160 to 300 keV deuteron energies. Lines are drawn to show the trend of the excitation functions. Only statistical errors are plotted.

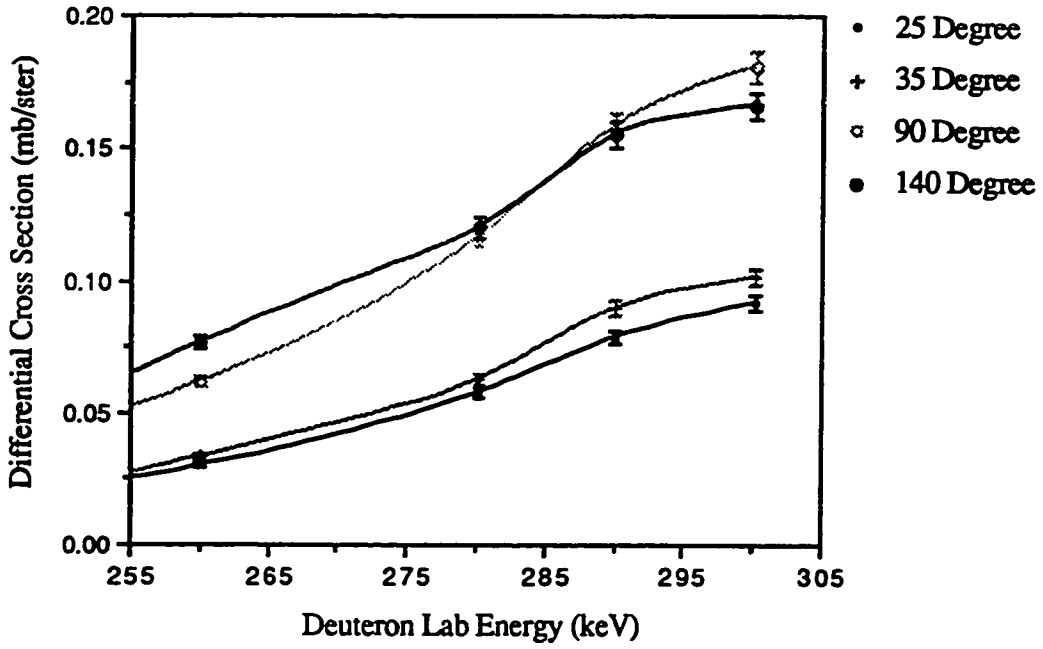

Fig. 4.2. Excitation functions of $^{12}C(d,p)$ reaction at 25, 35, 90 and 140 degrees over 255 to 300 keV deuteron energies. Lines are drawn to show the trend of the excitation functions. Only statistical errors are plotted.

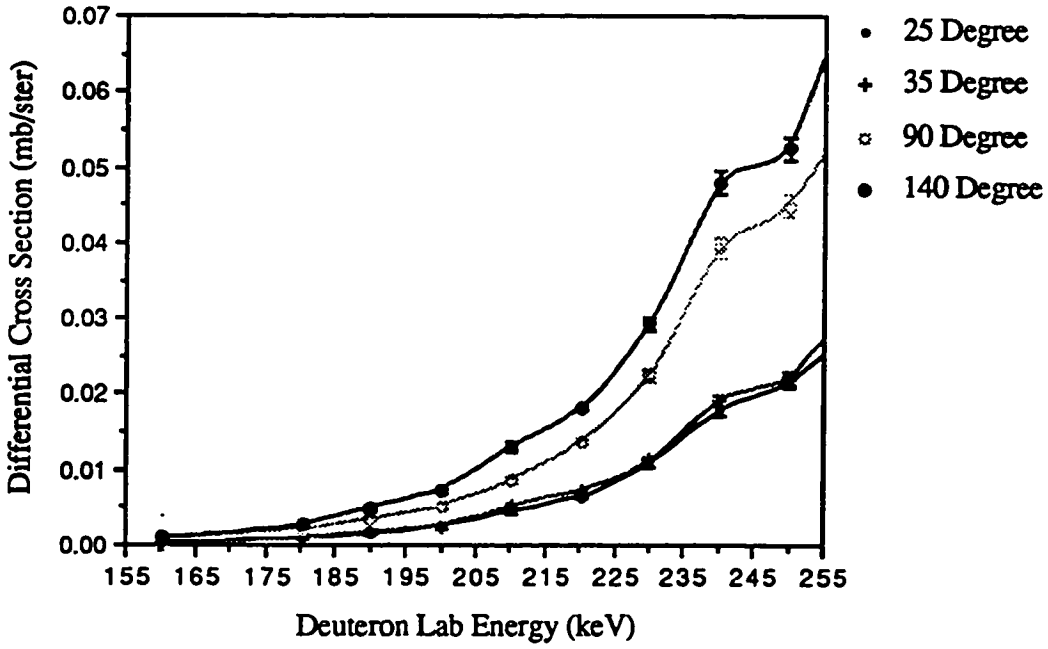

Fig. 4.3. Excitation functions of $^{12}C(d,p)$ reaction at 25, 35, 90 and 140 degrees over 160 to 255 keV deuteron energies. Lines are drawn to show the trend of the excitation functions. Only statistical errors are plotted.

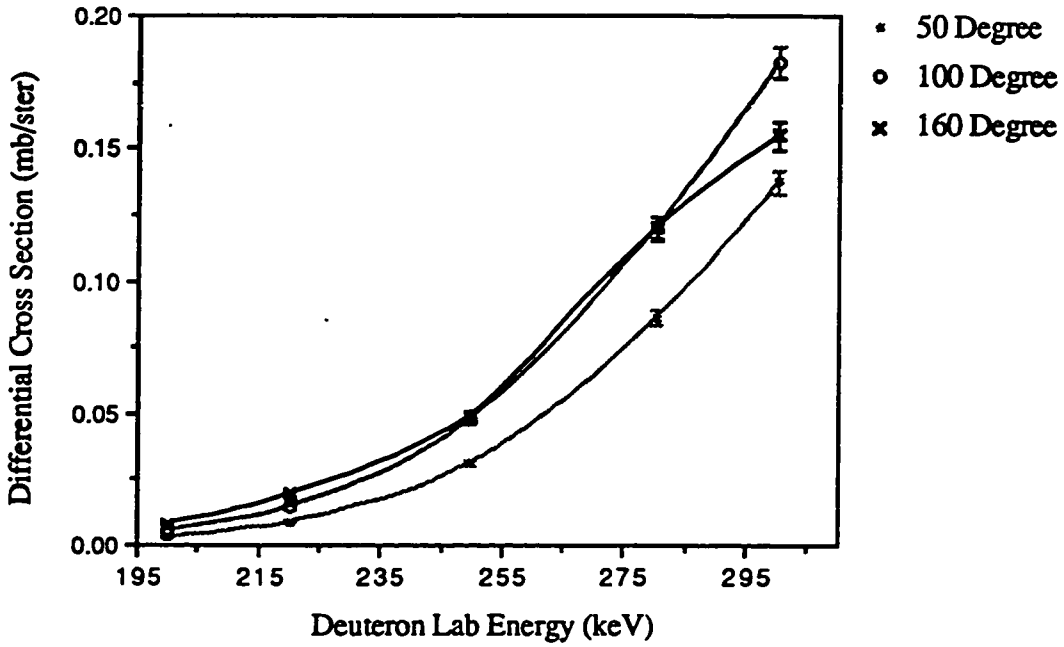

Fig. 4.4. Excitation functions of $^{12}C(d,p)$ reaction at 50, 100 and160 degrees over 200 to 300 keV deuteron energies. Lines are drawn to show the trend of the excitation functions. Only statistical errors are plotted.

It is also noticed that the excitation function curves for 90 and 140 degrees cross each other between 270 and 290 keV. In order to show this behavior clearly, excitation function are plotted in fig. 4.2 over the deuteron range of 255 to 300 keV. From this figure, it is obvious that the cross over is taking place only between 90 and 140 degrees but not between 25 and 35 degrees. In fig. 4.3 the excitation function are shown for the energy range 160 to 255 keV. Within the experimental uncertainties no cross over between excitation functions of any set of angles is observed in this energy range. Also it shown in fig. 4.4 the excitation functions at 50, 100 and 160 degrees over the deuteron energy range 200 to 300 keV. These excitation functions were derived from angular distribution data. The cross over of 100 and 160 degrees excitation functions is very prominent in this figure also. The cross over in excitation functions takes place due to change in cross section with changing incident particle energy. Here the cross over takes place between 90 and 140 degrees as well as between 100 and 160 degrees excitation functions. This means that the increase in cross section with deuteron energy above 270 keV for 140 and 160 degrees is less that for 90 and 100 degrees. This effect is clearly demonstrated in the angular distributions for the corresponding deuteron energies.

4.2 Differential Cross Sections

Fig. 4.5 and 4.6 show the differential cross sections of $^{12}C(d,p)$ reaction. In order to show the trend of the differential cross sections, the data points are connected by a solid line. The differential cross sections were

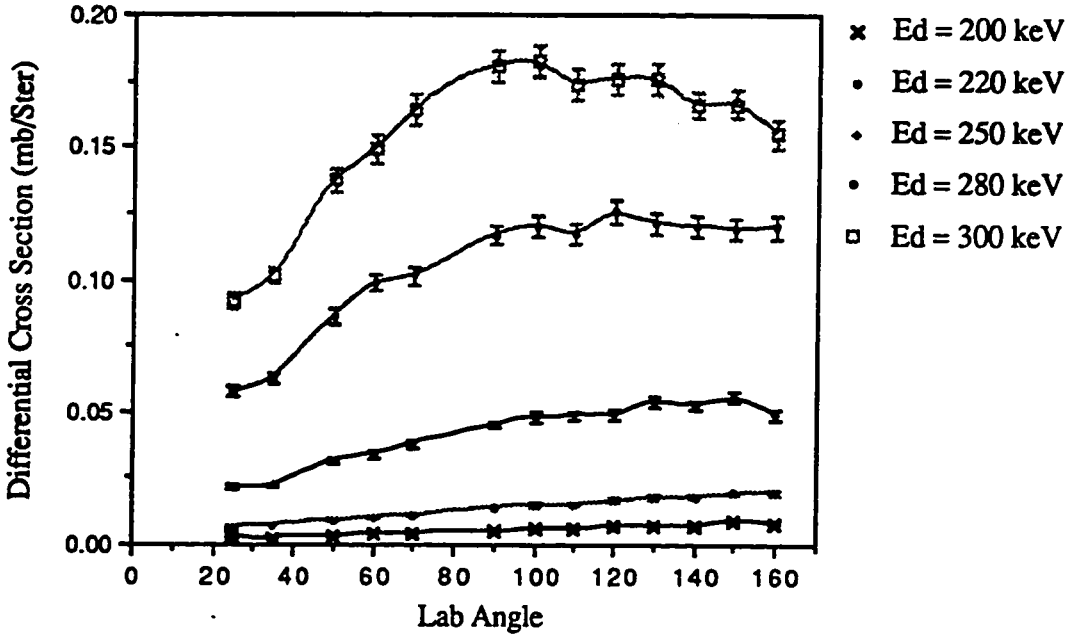

Fig. 4.5. differential cross sections of $^{12}C(d,p)$ reaction at 200, 220, 250, 280 and 300 keV deuteron energies. Lines are drawn to show the trend of the angular distributions. Only statistical errors are plotted.

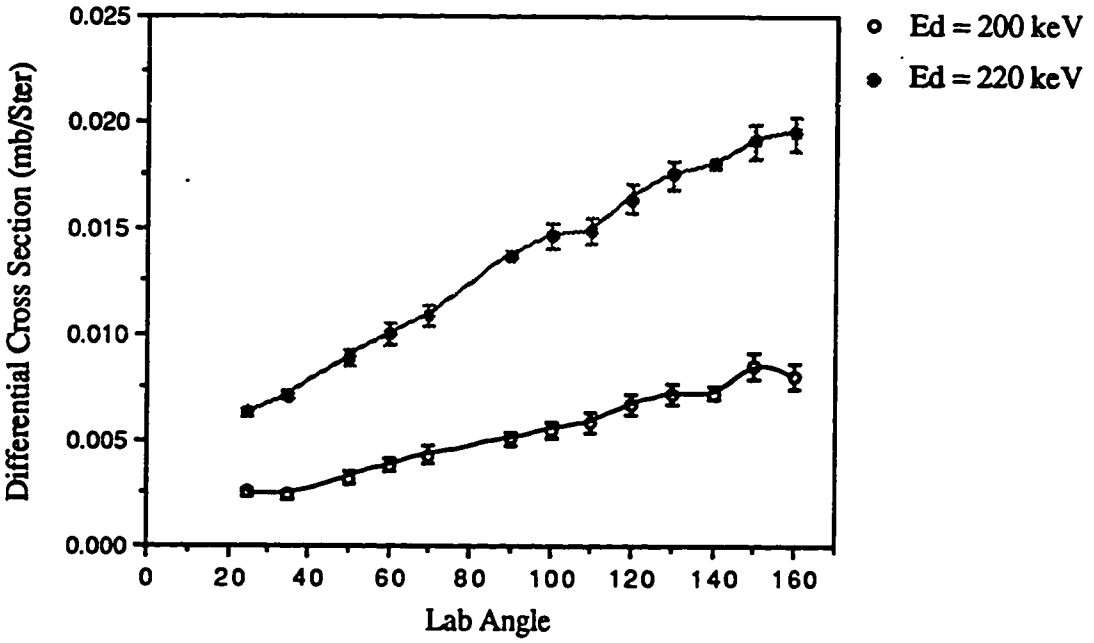

Fig. 4.6. Differential cross sections of $^{12}C(d,p)$ reaction at 200 and 220 keV deuteron energies. Lines are drawn to show the trend of the differential cross sections. Only statistical errors are plotted.

measured from 25 to 160 degrees in 10-degree steps at deuteron energies 200, 220, 250, 280 and 300 keV. Within the statistical uncertainties, all distributions show a smooth trend and have no structure. For all angles, the cross section increases with deuteron energy. Due to lower cross section at 200 and 220 keV, the differential cross sections for 200 and 220 keV are shown separately in fig. 4.6. The errors shown in both figures are statistical. The statistical errors for 250 to 300 keV is 3 to 4 % while for 200 keV, it is 5 to 9 %. As some angles of 220 keV distribution were used for normalization, they have smaller uncertainties. The over all statistical uncertainty of 220 keV data is 2 to5 %.

The differential cross sections show two prominent features, namely, asymmetry and backward peaking. The 200 and 220 keV distribution which are shown in fig. 4.6 have simply increasing trend of cross section with angle. They do not show any cross section maximum. As the deuteron energy increases, the cross section increases and a maximum starts to develop. The rate of increase of cross section is different at different angle. The rate of increase around 90 degree is more than that at backward angles. As a result of this increase, the differential cross sections at 300 keV show asymmetric distribution with a broad maximum around 100 degree. From the shape of the excitation function and angular distribution, one can learn about the mechanism of nuclear process involved in the reaction[32]. The measured excitation functions at 25, 35, 90 and 140 degrees do not show resonance structure. If the nuclear reaction has gone through the nonresonant compound stage, the energy spectra of the detected protons

would be continuous one[3] but discrete energies of proton are detected in $^{12}C(d,p)$. Therefore the nucleus has gone though a direct interaction of (d,p) type. This argument is further strengthened by the asymmetric and backward peaking shape of the angular distribution.

As mentioned in chapter 1, there is a lack of $^{12}C(d,p)$ data below 0.5 MeV deuteron energy. The only data below 0.5 MeV is published by G. D. Putt[8] who has measured the differential cross section of $^{12}C(d,p)$ at 0.41 and 0.51 MeV deuteron energies. Since the deuteron energies of Putt's data is very near to the deuteron energies 0.2 to 0.3 MeV, used in this experiment, a comparison of the two data sets is worthwhile. Fig. 4.7 shows Putt's data along with the 0.25, 0.28 and 0.3 MeV data measured in this experiment. The figure shows similar trends. The rate of change of cross section increases with deuteron energy. The rate of change is maximum around 90 degree. The comparison of shapes of the distributions reveals that as the deuteron energy increases the broad cross section maxima tends to become narrower. In this experiment, the maximum cross section of 0.18 mb/ster is measured around 100 degree for the 300 keV distribution while 0.41 MeV Putt's data has the maximum cross section around 90 degree . This shows a shift of 10 degree in maximum positions in the forward direction between 0.30 and 0.41 MeV. For 0.51 MeV Putt's data the cross section maxima is further shifted by 10 degree to around 80 degree with a value of 1.0 mb/ster. 0.41 MeV data and 0.30 MeV data show more asymmetric behavior than 0.51 MeV data. This trend is clearly shown in fig. 4.8 where 0.41 and 0.30 distribution are plotted separately. Putt has fitted his data using Distorted

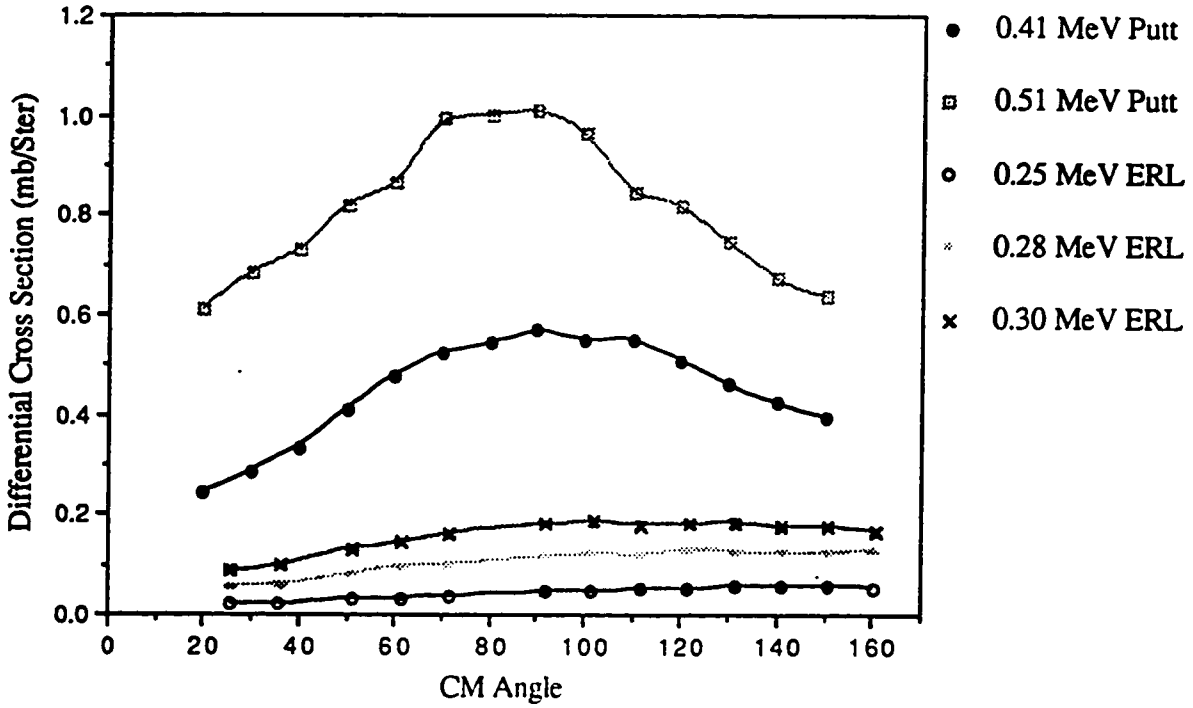

Fig. 4.7. 0.41 and 0.51 MeV differential cross sections of $^{12}C(d,p)$ reaction from Putt Along with 0.25, 0.28 and 0.30 MeV data measured in this experiment. Lines are drawn to show the trend of the differential cross sections. Only statistical errors are plotted.

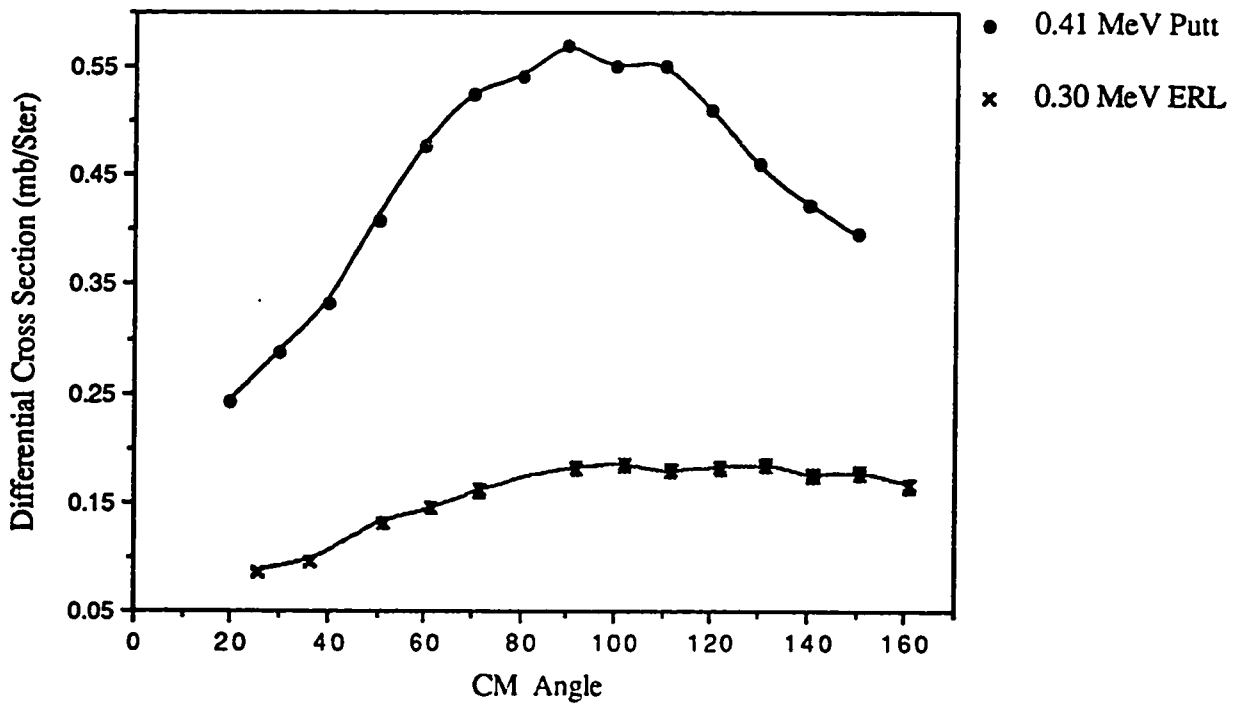

Fig. 4.8. 0.41 MeV differential cross sections of $^{12}C(d,p)$ reaction from Putt Along with 0.30 MeV data measured in this experiment. Lines are drawn to show the trend of the differential cross sections. Only statistical errors are plotted.

Wave Born Approximation (DWBA) with zero absorptive potential for the distorted wave. The calculation provided a good fit to the Putt's data. Therefore, one may expect that the DWBA stripping calculation may also fit to the data measured in this experiment. At present, no DWBA calculation code is available and therefore the calculations will be carried out some time later.

APPENDIX A

TABLES OF EXCITATION FUNCTIONS AND ANGULAR DISTRIBUTIONS DATA

Table A.1. Differential cross sections for $^{12}C(d,p)$ reaction at E_d=200, 220, 250, 280, 300 keV. Total errors consist of statistical and systematic errors. Systematic errors are assumed to be 4%.

θ_{Lab}	E_d=200 keV			E_d=220 keV			E_d=250 keV			E_d=280 keV			E_d=300 keV		
	$\frac{d\sigma(\theta)}{d\Omega}$ (mb)	stat. error (mb)	total error (mb)	$\frac{d\sigma(\theta)}{d\Omega}$ (mb)	stat. error (mb)	total error (mb)	$\frac{d\sigma(\theta)}{d\Omega}$ (mb)	stat. error (mb)	total error (mb)	$\frac{d\sigma(\theta)}{d\Omega}$ (mb)	stat. error (mb)	total error (mb)	$\frac{d\sigma(\theta)}{d\Omega}$ (mb)	stat. error (mb)	total error (mb)
25	0.0025	0.0002	0.0002	0.0063	0.0002	0.0003	0.0214	0.0007	0.0011	0.0577	0.0018	0.0030	0.0915	0.0030	0.0047
35	0.0024	0.0002	0.0002	0.0071	0.0002	0.0003	0.0221	0.0008	0.0012	0.0624	0.0020	0.0032	0.1014	0.0033	0.0052
50	0.0032	0.0003	0.0003	0.0089	0.0004	0.0006	0.0313	0.0012	0.0018	0.0856	0.0029	0.0045	0.1371	0.0047	0.0072
60	0.0038	0.0003	0.0003	0.0100	0.0005	0.0006	0.0337	0.0013	0.0019	0.0986	0.0033	0.0052	0.1488	0.0050	0.0078
70	0.0043	0.0004	0.0004	0.0109	0.0005	0.0007	0.0378	0.0015	0.0021	0.1010	0.0034	0.0053	0.1641	0.0056	0.0086
90	0.0051	0.0003	0.0003	0.0137	0.0002	0.0006	0.0449	0.0014	0.0023	0.1165	0.0035	0.0059	0.1806	0.0057	0.0092
100	0.0055	0.0004	0.0005	0.0146	0.0006	0.0009	0.0480	0.0018	0.0026	0.1201	0.0040	0.0063	0.1823	0.0061	0.0095
110	0.0059	0.0005	0.0005	0.0149	0.0006	0.0009	0.0483	0.0018	0.0027	0.1172	0.0040	0.0061	0.1741	0.0059	0.0092
120	0.0067	0.0005	0.0006	0.0164	0.0007	0.0010	0.0485	0.0018	0.0027	0.1255	0.0042	0.0065	0.1759	0.0059	0.0092
130	0.0072	0.0005	0.0006	0.0175	0.0007	0.0010	0.0538	0.0020	0.0029	0.1212	0.0040	0.0063	0.1757	0.0059	0.0092
140	0.0072	0.0003	0.0006	0.0180	0.0002	0.0010	0.0525	0.0016	0.0029	0.1200	0.0036	0.0063	0.1658	0.0056	0.0087
150	0.0085	0.0006	0.0007	0.0191	0.0008	0.0011	0.0552	0.0020	0.0030	0.1190	0.0040	0.0062	0.1661	0.0056	0.0087
160	0.0080	0.0006	0.0007	0.0195	0.0008	0.0011	0.0492	0.0019	0.0027	0.1196	0.0040	0.0062	0.1549	0.0052	0.0081

Table A.2. Excitation functions of $^{12}C(d,p)$ reaction at $\theta_{Lab}=25^0$, 35^0, 90^0 and 140^0. Total errors consist of statistical and systematic errors. Systematic errors are assumed to be 4%.

E_d Lab	$\theta_{Lab}=25^0$			$\theta_{Lab}=35^0$			$\theta_{Lab}=90^0$			$\theta_{Lab}=140^0$		
(keV)	$\frac{d\sigma(\theta)}{d\Omega}$ (mb)	stat. error (mb)	total error (mb)	$\frac{d\sigma(\theta)}{d\Omega}$ (mb)	stat. error (mb)	total error (mb)	$\frac{d\sigma(\theta)}{d\Omega}$ (mb)	stat. error (mb)	total error (mb)	$\frac{d\sigma(\theta)}{d\Omega}$ (mb)	stat. error (mb)	total error (mb)
160	0.0002	0.0001	0.0001	0.0000	0.0000	0.0000	0.0011	0.0001	0.0001	0.0009	0.0001	0.0001
180	0.0009	0.0001	0.0001	0.0009	0.0001	0.0001	0.0021	0.0002	0.0002	0.0027	0.0002	0.0002
190	0.0015	0.0001	0.0002	0.0017	0.0002	0.0002	0.0034	0.0002	0.0003	0.0049	0.0003	0.0004
200	0.0025	0.0002	0.0002	0.0024	0.0002	0.0002	0.0051	0.0003	0.0003	0.0072	0.0003	0.0004
210	0.0044	0.0003	0.0003	0.0051	0.0003	0.0004	0.0085	0.0004	0.0006	0.0129	0.0006	0.0008
220	0.0063	0.0002	0.0003	0.0071	0.0002	0.0003	0.0137	0.0002	0.0006	0.0180	0.0002	0.0008
230	0.0108	0.0005	0.0006	0.0111	0.0005	0.0006	0.0224	0.0008	0.0012	0.0292	0.0010	0.0015
240	0.0178	0.0007	0.0010	0.0191	0.0008	0.0011	0.0392	0.0014	0.0021	0.0479	0.0016	0.0025
250	0.0214	0.0007	0.0011	0.0220	0.0008	0.0012	0.0449	0.0014	0.0023	0.0525	0.0016	0.0026
260	0.0298	0.0010	0.0016	0.0332	0.0011	0.0017	0.0613	0.0019	0.0031	0.0764	0.0023	0.0038
280	0.0577	0.0019	0.0030	0.0624	0.0020	0.0032	0.1165	0.0035	0.0059	0.1200	0.0036	0.0060
290	0.0784	0.0024	0.0039	0.0897	0.0027	0.0045	0.1588	0.0046	0.0078	0.1552	0.0045	0.0077
300	0.0915	0.0030	0.0047	0.1014	0.0033	0.0052	0.1806	0.0057	0.0092	0.1658	0.0053	0.0085

Table A.3.1 Center of mass differential cross sections for $^{12}C(d,p)$ reaction at 200 keV deuteron lab energy. Total errors consist of statistical and systematic errors. Systematic errors are assumed to be 4%.

	E_d=200 keV			
θ_{Lab} (degree)	θ_{cm} (degree)	$\frac{d\sigma_{cm}(\theta_{cm})}{d\Omega_{cm}}$ (mb)	statistical error (mb)	total error (mb)
25	25.7	0.0024	0.0002	0.0002
35	35.9	0.0023	0.0002	0.0002
50	51.2	0.0031	0.0003	0.0003
60	61.4	0.0037	0.0003	0.0003
70	71.5	0.0042	0.0003	0.0004
90	91.6	0.0051	0.0003	0.0003
100	101.6	0.0056	0.0004	0.0005
110	111.5	0.0060	0.0005	0.0005
120	121.4	0.0069	0.0005	0.0006
130	131.2	0.0075	0.0005	0.0006
140	141.0	0.0075	0.0003	0.0005
150	150.8	0.0089	0.0006	0.0007
160	160.5	0.0084	0.0006	0.0007

Table A.3.2 Center of mass differential cross sections for $^{12}C(d,p)$ reaction at 220 keV deuteron lab energy. Total errors consist of statistical and systematic errors. Systematic errors are assumed to be 4%.

	E_d=220 keV			
θ_{Lab} (degree)	θ_{cm} (degree)	$\frac{d\sigma_{cm}(\theta_{cm})}{d\Omega_{cm}}$ (mb)	statistical error (mb)	total error (mb)
25	25.7	0.0059	0.0001	0.0003
35	36.0	0.0068	0.0001	0.0003
50	51.3	0.0085	0.0004	0.0005
60	61.4	0.0097	0.0005	0.0006
70	71.6	0.0107	0.0005	0.0007
90	91.7	0.0137	0.0002	0.0006
100	101.6	0.0147	0.0006	0.0009
110	111.6	0.0152	0.0006	0.0009
120	121.4	0.0169	0.0007	0.0010
130	131.3	0.0182	0.0007	0.0010
140	141.1	0.0189	0.0002	0.0008
150	150.8	0.0202	0.0008	0.0011
160	160.6	0.0206	0.0008	0.0012

Table A.3.3 Center of mass differential cross sections for $^{12}C(d,p)$ reaction at 250 keV deuteron lab energy. Total errors consist of statistical and systematic errors. Systematic errors are assumed to be 4%.

	E_d=250 keV			
θ_{Lab} (degree)	θ_{cm} (degree)	$\frac{d\sigma_{cm}(\theta_{cm})}{d\Omega_{cm}}$ (mb)	statistical error (mb)	total error (mb)
25	25.7	0.0202	0.0007	0.0011
35	36.0	0.0210	0.0007	0.0011
50	51.4	0.0301	0.0012	0.0017
60	61.5	0.0327	0.0013	0.0018
70	71.7	0.0370	0.0014	0.0021
90	91.8	0.0449	0.0014	0.0023
100	101.7	0.0486	0.0018	0.0027
110	111.7	0.0494	0.0019	0.0027
120	121.5	0.0501	0.0019	0.0028
130	131.4	0.0560	0.0021	0.0031
140	141.1	0.0551	0.0017	0.0028
150	150.9	0.0583	0.0022	0.0032
160	160.6	0.0522	0.0020	0.0029

Table A.3.4 Center of mass differential cross sections for $^{12}C(d,p)$ reaction at 280 keV deuteron lab energy. Total errors consist of statistical and systematic errors. Systematic errors are assumed to be 4%.

	E_d=280 keV			
θ_{Lab} (degree)	θ_{cm} (degree)	$\frac{d\sigma_{cm}(\theta_{cm})}{d\Omega_{cm}}$ (mb)	statistical error (mb)	total error (mb)
25	25.8	0.0544	0.0017	0.0028
35	36.1	0.0592	0.0019	0.0030
50	51.4	0.0821	0.0028	0.0043
60	61.6	0.0955	0.0032	0.0050
70	71.8	0.0989	0.0034	0.0052
90	91.9	0.1165	0.0035	0.0059
100	101.8	0.1216	0.0040	0.0063
110	111.8	0.1200	0.0041	0.0063
120	121.6	0.1298	0.0043	0.0068
130	131.4	0.1265	0.0042	0.0066
140	141.2	0.1263	0.0038	0.0063
150	150.9	0.1260	0.0042	0.0066
160	160.6	0.1273	0.0043	0.0066

Table A.3.5 Center of mass differential cross sections for $^{12}C(d,p)$ reaction at 300 keV deuteron lab energy. Total errors consist of statistical and systematic errors. Systematic errors are assumed to be 4%.

	E_d=300 keV			
θ_{Lab} (degree)	θ_{cm} (degree)	$\frac{d\sigma_{cm}(\theta_{cm})}{d\Omega_{cm}}$ (mb)	statistical error (mb)	total error (mb)
25	25.8	0.0862	0.0028	0.0045
35	36.1	0.0960	0.0031	0.0050
50	51.5	0.1314	0.0045	0.0069
60	61.7	0.1440	0.0048	0.0075
70	71.8	0.1605	0.0055	0.0085
90	91.9	0.1807	0.0057	0.0092
100	101.9	0.1845	0.0062	0.0097
110	111.8	0.1783	0.0061	0.0094
120	121.7	0.1820	0.0061	0.0095
130	131.5	0.1836	0.0062	0.0096
140	141.2	0.1747	0.0055	0.0089
150	151.0	0.1763	0.0060	0.0092
160	160.7	0.1652	0.0055	0.0086

APPENDIX B

DESCRIPTION OF ELECTRONICS NIM MODULES

B.1 Charge Sensitive Preamplifier

The basic function of a preamplifier is to amplify weak signals from a detector and to drive it though the cable that connects the preamplifier with the rest of the electronics. At the same time, it must add the least amount of noise possible. Since the input signal at the preamplifier is generally weak, preamplifiers are normally mounted as close as possible to the detector so as to minimize cable length. In this way, pickup of stray electromagnetic fields is reduced and cable capacitance, which decreases the signal-to-noise ratio, is minimized.[18] Preamplifiers can be of either voltage sensitive or charge sensitive type. If the input capacitance of the detector is constant, a voltage sensitive preamplifier is used with it. On the other hand, if the input capacitance of the detector varies with the operation parameter of the detector, which is the case for SSB detector, a charged sensitive preamplifier is required for the detector.[17]

B.2 Spectroscopy Amplifier

The main function of the spectroscopy amplifier is to shape the input

signal to a convenient form for further processing, and amplify it linearly without losing pulse height information. The selectable pulse shaping time of the amplifier allows to reduce the pile up effects due to addition of two pulses following each other within the selected pulse shaping time. Pulse shaping also optimize signal to noise ratio. For a given noise spectrum there usually exist an optimum pulse shaping time for which signal is least disturbed by the noise.[18]

B.3 Single Channel Analyzer

The single channel analyzer is a device which sorts incoming analog signal according to their amplitudes. It contains a lower level threshold below which signals are blocked. In addition, there is also an upper level threshold above which signals are rejected. Thus only signals which fall between these two levels generate a standard positive logic signal at the output of the single channel analyzer.

B.4 Gate and Delay Generator

A gate and delay generator generates variable width gate pulses of microsecond duration. The duration desired can be chosen by a front panel helipot. Gate generators can be triggered by an input logic signal. Another helipot on the front panel allows the delay of the output gate signal by microsecond delay. The output gate signal can be used either to gate a linear signal or can be used for counting by a scaler.[18]

B.5 Digital Current Integrator

The digital current integrator is designed to accurately measured dc or the average value of the pulse current.[19] It digitizes the input current by producing an output pulse of specific values of input charge. A front panel switch permits the selection of three different amounts of charge 10^{-10}, 10^{-8} or 10^{-6} coulomb required to produce an output pulse. The instrument has a digitizing rate from 0-10 kHz to provide wide dynamic range on each setting and high resolution read out without meter interpolation.

APPENDIX C

Listing of Data Acquisition Codes

JALAL.COM COM FILE

```
$ PUT 2
$ DMEM ALL
$ AMEM 1 1024 I*4 1D DET 1
$ AMEM 2 1024 I*4 1D DET 2
$ AMEM 3 1024 I*4 1D DET 3
$ AMEM 4 1024 I*4 1D DET 4
$ AMEM 5 1024 I*4 1D
$ AMEM 6 1024 I*4 1D
$ AMEM 10 1024 R*4 1D
$ AMEM 88 256 I*4 1D DTC_DEF
$ GATE NEW
$ GATE 1 5
$ GATE 2 5
$ GATE 3 5
$ GATE 4 5
$ CLEAR ALL
$ SCAL NEW
$ SCAL HEAD 1 Det 1. Det 2. Det 3. Det 4. CUR.PRE.
$ SCAL NUMB 1 11 1 2 3 4 LR2551
$ SCAL NUMB 1 12 1 REGISTER
$ EVOP SE DET1
$ EVOP SE DET2
```

```
$ EVOP SE DET3
$ EVOP SE DET4
$ STOP XBOXSP
$ FOR BOXUSR
$ BOXLINK
$ @ BOXSET
$ SCAL CLEAR ALL
$ SCAL READ ALL
$ ! SCLBUFF DEF 4 1 1 2 2 3 3 4 4
$ WRITE SYS$OUTPUT "_______Jalal Dat.aqc.Code RUNNING_______"
```

DET1.DAP DAP file for detector 1

```
DET1
1
100
INIT
1 28 9 26
1 28 8 26
1 30 1 26
1 1 0 16 1024
1 1 0 26
LAM
1 1 0 2
END
```

DET1.EVL EVL flile for detector 1

```
SPEC S1 1
DATA EVSIZ 1
FORMAT FF 1 10 1
GET FF
INC S1
END
```

DET2.DAP DAP file for detector 2

```
DET2
2
1 0 0
INIT
1 3 0 16 1024
1 3 0 26
LAM
1 3 0 2
END
```

DET2.EVL EVL flile for detector 2

```
SPEC S1 2
DATA EVSIZ 1
FORMAT FF 1 10 1
GET FF
INC S1
END
```

DET3.DAP DAP file for detector 3

```
DET3
3
1 0 0
INIT
1 5 0 16 1024
1 5 0 26
LAM
1 5 0 2
END
```

DET3.EVL EVL flile for detector 3

```
SPEC S1 3
DATA EVSIZ 1
FORMAT FF 1 10 1
GET FF
INC S1
END
```

DET4.DAP DAP file for detector 4

```
DET4
3
1 0 0
INIT
1 7 0 16 1024
1 7 0 26
LAM
1 7 0 2
END
```

DET4.EVL EVL flile for detector 4

```
SPEC S1 4
DATA EVSIZ 1
FORMAT FF 1 10 1
GET FF
INC S1
END
```

SCLR.DAP DAP file for preset scalers and the scalers

```
6               ! MBD CHAN TO READ SCALERS
1               ! TIME INTERVAL IN SECONDSTO UPDATE SCALERS
PRESET          ! KEYWORD FOR SCALER PRESET
5               ! NUMBER OF THE PRESET SCALER
1000000         ! INITIAL VALUE OF THE PRESET
3               ! NUMBER OF FUNCTION CODES TO PERFORM AFTER A PRESET
16              ! FUNCTION CODES TO PERFORM
9
25
DTC             ! KEYWORD FOR DEAD TIME CORRECTIONS
1               ! MBD CHAN
1               ! SCALER NUMBER
2
2
3
3
4
4
END
```

BOXUSER.FOR Fortran subroutine

```
C
C     ****************************************************************
C     *                                                              *
C     *                        BOXUSER.FOR                           *
C     *                                                              *
C     ****************************************************************
C
C
C
      SUBROUTINE BOXUSER
      INCLUDE 'XSYSDIR: XCOM.FOR/NORLIST'
      INCLUDE 'XSYSDIR: XERRDEF.FOR/NORLIST'
```

```
      CHARACTER*8     BXLABEL(36),BXCHAR(36)
      CHARACTER*32    BXLMESS(10)
      CHARACTER*4     BXFLAG(32)
      COMMON /BOXSAVE/BXLABEL,BXCHAR,BXMESS,BXFLAG
      REAL*4 RFLAG(32),XX1,XX2,NORM1,NORM2,NORM3,NORM4,NORMO
     REAL*4 AREA1,AREA2,AREA3,AREA4
     INTEGER*4 IFLAG(32),IX1,IX2,IX11,BCI,BEAM
      LOGICAL*4 LFLAG(32)
      BYTE BFLAG(128)
     EQUIVALENCE (BXFLAG(1),BFLAG(1)),(RFLAG(1),BFLAG(1))
     EQUIVALENCE (IFLAG(1),BFLAG(1)),(LFLAG(1),BFLAG(1))
      REAL AREA(36),ERROR(36),NETAREA(36)
      INTEGER ICHAN(2,36)
      CHARACTER COND*8
      DATA IAREA,ILOOPS,IHAVE/100,0,0/
      DATA IRT_IN,IRT_OUT,ILT_IN,ILT_OUT,IMON_IN/11,12,1,2,21
      SAVE ILOOPS,IHAVE
      SAVE ART_IN,ALT_IN,AMON_IN
     DO 10 K=1,4
     IX11=X_DIR(X_LOW,K+2)
     IX1=X_GATES(1,IX11)+1
     IX2=X_GATES(2,IX11)+1
     XX2=IX2/1000.
     XX1=IX1
     XX1=XX1+XX2
     IF(XX1.LT.0.)XX1=0.
     IF(K.EQ.1)CALL BOXREAL (17,XX1)
     IF(K.EQ.2)CALL BOXREAL (18,XX1)
     IF(K.EQ.3)CALL BOXREAL (19,XX1)
     IF(K.EQ.4)CALL BOXREAL (20,XX1)
10     CONTINUE
     BCI=PRESET-SCLREAD(5)
     BEAM=SCLREAD(5)-SCL_OLD(5,2)
     CALL SHORTSUM(1,1,AREA1)
     CALL SHORTSUM(2,1,AREA2)
     CALL SHORTSUM(3,1,AREA3)
```

```
      CALL SHORTSUM(4 , 1 , AREA4)
      CALL BOXINTEG(6 , PRESET)
      CALL BOXREAL(9 , AREA1)
      CALL BOXREAL(10 , AREA2)
      CALL BOXREAL(11 , AREA3)
      CALL BOXREAL(12 , AREA4)
      CALL BOXINTEG(13 , BCI)
      NORMO=BCI
      IF(NORMO.EQ.0.)GOTO11
      NORM1=(AREA1*PRESET)/NORMO
      NORM2=(AREA2*PRESET)/NORMO
      NORM3=(AREA3*PRESET)/NORMO
      NORM4=(AREA4*PRESET)/NORMO
      GOTO 12
11    NORM1=0.
      NORM2=0.
      NORM3=0.
      NORM4=0.
12    CALL BOXREAL(21 , NORM1)
      CALL BOXREAL(22 , NORM2)
      CALL BOXREAL(23 , NORM3)
      CALL BOXREAL(24 , NORM4)
      CALL BOXREAL(25 , DTC(2))
      CALL BOXREAL(26 , DTC(3))
      CALL BOXREAL(27 , DTC(4))
      CALL BOXREAL(28 , DTC(5))
      CALL BOXINTEG(29 , SCL_OLD(5 , 1))
      CALL BOXINTEG(30 , SCL_OLD(5 , 2))
      CALL BOXINTEG(31 , SCL_OLD(5 , 3))
      CALL BOXINTEG(32 , SCL_OLD(5 , 4))
      CALL BOXINTEG(14 , SCLREAD(5))
      IF (DATAON.EQ.0) CALL BOXMESS (1 , '___DATA ACQ. OFF___')
      IF (DATAON.EQ.1) CALL BOXMESS (1 , '___DATA ACQ. ON___')
       RETURN
       END
```

APPENDIX D

KINEMATICS OF $^{12}C(d,p)$ AND D(d,p) REACTIONS

Table D.1. Lab energies of proton from $^{12}C(d,p)$ and D(d,p) reactions.

$\theta_{l,ab}$	E_d=200 keV		E_d=220 keV		E_d=250 keV		E_d=280 keV		E_d=300 keV	
	E_p(MeV) from $^{12}C(d,p)$	D(d,p)	E_p(MeV) from $^{12}C(d,p)$	D(d,p)	E_p(MeV) from $^{12}C(d,p)$	D(d,p)	E_p(MeV) from $^{12}C(d,p)$	D(d,p)	E_p(MeV) from $^{12}C(d,p)$	D(d,p)
20	2.826	3.639	2.850	3.675	2.884	2.726	2.918	3.775	2.941	3.807
40	2.799	3.527	2.821	3.556	2.853	3.598	2.885	3.639	2.907	3.665
60	2.758	3.362	2.778	3.382	2.807	3.411	2.836	3.439	2.855	3.457
80	2.709	3.169	2.726	3.179	2.751	3.194	2.776	3.208	2.793	3.217
100	2.657	2.977	2.671	2.977	2.693	2.978	2.715	2.979	2.729	2.980
120	2.609	2.806	2.621	2.799	2.639	2.788	2.658	2.779	2.670	2.773
140	2.571	2.675	2.581	2.661	2.596	2.643	2.612	2.626	2.623	2.616
160	2.546	2.592	2.555	2.576	2.569	2.552	2.583	2.531	2.592	2.518

APPENDIX E

ENERGY LOSS CALCULATIONS

The average total energy loss ΔE of incident particles within a material may be calculated using the following expression

$$\Delta E = \int \frac{dE}{dx}\, dx \qquad \text{(E-1)}$$

where $\frac{dE}{dx}$ is the specific energy loss of the incident particle within the material . x is the distance incident particles travel in material. The values of $\frac{dE}{dx}$ are calculated using the energy loss calculation computer code TRIM-87. This code uses the corrected Bethe-Bloch formula to calculate the specific energy loss. The integral in eq. E.1 was calculated using a C program listed below. Over a small energy interval, the calculated values of $\frac{dE}{dx}$ can be fitted nicely to a polynomial equation of a second order. In our program, a polynomial equation of a second order which fits the calculated values of $\frac{dE}{dx}$ was used to calculate ΔE. Fitted equations for specific energy loss of deuterons in carbon and alpha particles in aluminum are shown in fig.

D.1 to D.3. In our calculation, we divided the thickness of the foil to many equal divisions and we assumed that the specific energy loss was constant over each division. The energy loss in one division was calculated by multiplying the specific energy loss by the thickness of this division. The specific energy loss at each division was calculated at energy equals to the incident energy on the foil minus the energy loss in the previous divisions. The total energy loss was obtained by adding the energy loss in all divisions.

C Program to Calculate Energy Loss in a Thin Foil

```
#include < math.h >
#include < stdio.h >
main ( )
{
      register long int i; / * i = loop index * /
      double ein , dee , des , ddxx , thck , divd ; / * ein = incident energy -
specific energy loss , des = energy difference , ddxx = divsison thickness ,
thck = thickness of the material , divd = number of division. * /
      double a , b , c ; / * coefficient of the polynomial * /
      printf ( " Enter Thickness & Number of Division : " ) ;
      scanf ( " %lf %lf " , &thck , &divd ) ;
      ddxx = thck / divd ; / * calculate division thickness * /
      printf ( " Enter the incident energy : " ) ;
      scanf ( " %lf " , &ein ) ;
      printf ( " Enter poly. coeff.  a  b  c  : " ) ;
      scanf ( " %lf %lf %lf " , &a , &b , &c) ;
            des = 0 ;
```

```
for( i = 1 ; i < = divd; i + + )
        {
        dee = ( a + ein * ( b + c * ein ) ) * ddxx ;
        ein - = dee ;
        des + = dee ;
        }
printf( " The Energy Loss is % .5f " , des ) ;
```

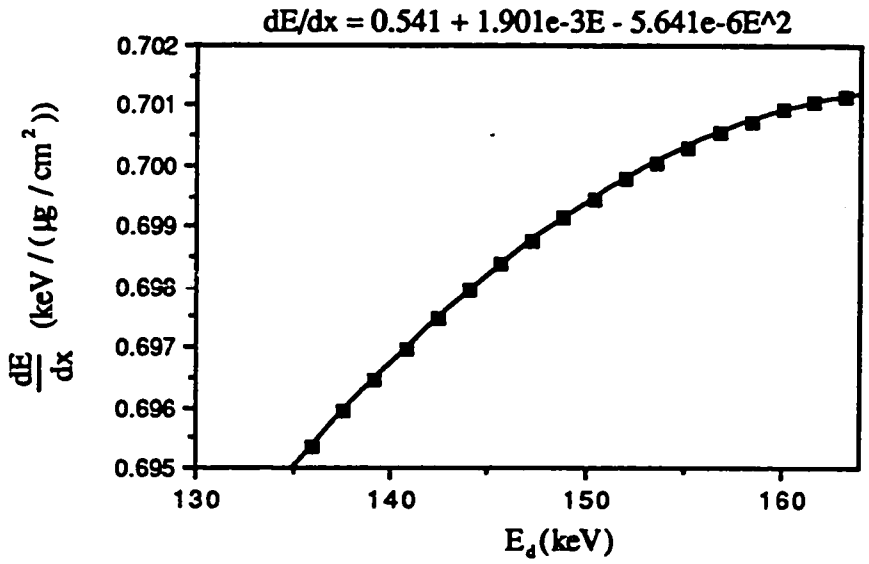

Fig. D.1. Calculated specific energy loss of deuterons in carbon about E_d = 160 keV fitted to a polynomial of a second order.

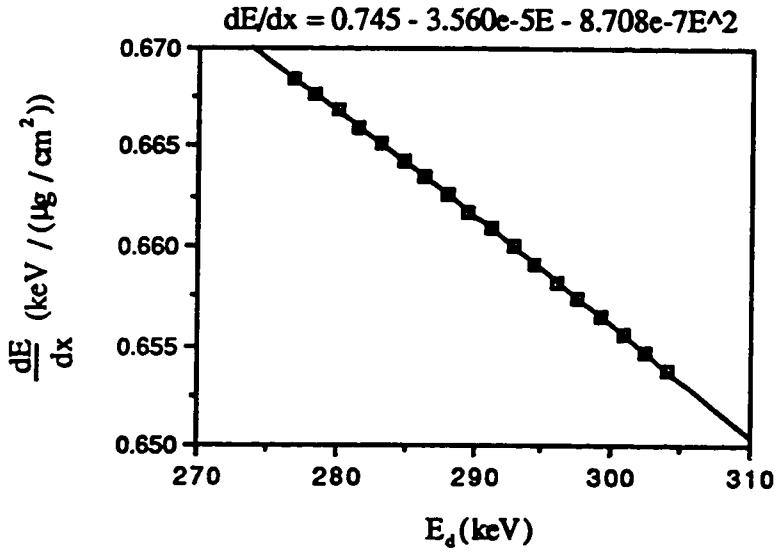

Fig. D.2. Calculated specific energy loss of deuterons in carbon about E_d = 300 keV fitted to a polynomial of a second order.

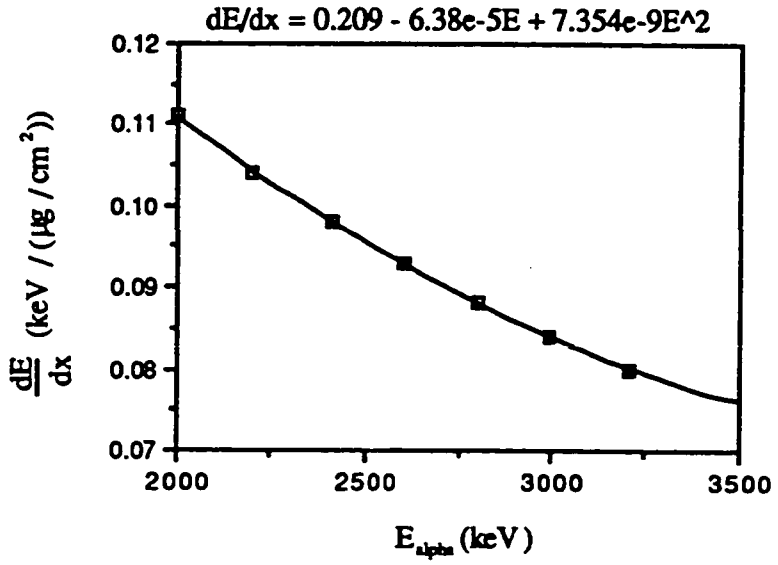

Fig. D.3. Calculated specific energy loss of alpha particles in aluminum about E_{alpha}=0.3 MeV fitted to a polynomial of a second order.

REFERENCES

1 D. F. Jackson, **Nuclear Reaction**, Chapman and Hall, London (1975).

2 N. Austern, **Direct Nuclear Reaction Theories**, Wiley-Interescince, Jonhn Wiley and Sons, New York (1970).

3 G. R. Sathcler, **Introduction to Nuclear Reaction**, John Wiley And Sons, New York (1980).

4 P. E. Hodgson, **Nuclear Reaction and Nuclear Structure**, Clarendon Press, Oxford (1971)

5 J. R. Oppenheimer and M. Pillips, **Phys. Rev.** 48 (1935) 500.

6 S. T. Butler, **Phys. Rev.** 80 (1950) 1095.

7 B. L. Cohen, **Concepts of Nuclear Physics**, McGraw-Hill Book Compony, New York 1971.

8 G. D. Putt, **Nucl. Phys.** A161 (1971) 547-564.

9 F. Ajzenberg-Selove, **Nucl. Phys.** A 360 (1981) 1.

10 G. C. Phillips, **Phys. Rev.** 80 (1950) 164.

11 H. D. Holmgren, J. M. Blair, B. E. Simmions, T. F. Stratton and R. V. Stuart, **Phys. Rev.** 95 (1954) 1544.

12 M. T. McEllistren, K. W. Jones, R. Chiba, R. A. Douglus, D. F. Herring and E. A. Silverstein, **Phys Rev.** 104 (1956) 1008.

13 J. H. Willamson, **Nucl. Phys.** 69 (1965) 481.

14 H. Al-Juwair, G. Blume,R. J. Jaarsma,C. R. Meitzler and K. H. Purser, **Nucl. Instr. and Meth.** B24/25 (1987) 810-812.

15 General Ionex Corporation, **Instruction Manual**, M1243750, June 06,1987.

16 H. Enge, **Introduction to Nuclear Physics,** Addison-Wesley Publishng Company, 1979.

17 G. F. Knoll, **Radiation Detection and Measurement,** John Wiley & Sons, Inc., 1979.

18 W. R. Leo, **Techniques for Nuclear and Particle Physics Experiments,** Springer-Verlag, Berlin, Heidelberg 1987.

19 EG&G Ortec, **Nuclear Instruments and Systems,** 86/87.

20 EG&G Ortec, **Silicon Charged Particle Radiation Detectors Instruction manual.**

21 T. W. Bonner, J. T. Eisinger, A.A. Krius, Jr., J. B. Marion, **Phys. Rev.** 101(1956) 209.

22 H. A. AL-Juwair and R. E. Abdal-AaL, **IEEE Tran. Nucl. Sci.** NS36, pp, 611, 1989.

23 R. E. Abdal-AaL and H. A. AL-Juwair, **IEEE Tran. Nucl. Sci.** NS36, pp. 687, 1989.

24 R. E. Abdal-AaL and H. A. AL-Juwair, **IEEE Tran. Nucl. Sci.** NS36, pp. 692, 1989.

25 **XSYS Reference Manual**-6th edition(1987), Triangle Universities Nuclear Lab, Duke University, Durham, N. C., USA.

26 R. Timmermann, H. W. Becker, C. Rolfs, U. Schrouder,and H. P. Trautvetter, **Nucl. Phys.** A477(1988) 105.

27 D. L. Smith, R. G. Polk and T. G. Miller, **Nucl. Instr. and Meth.** 64(1968) 157-166.

28 C. M. Lederev and V. Shirley, **Table of Isotopes,** Lawrence Berkeley Laboratory.

29 K. U. Ketlner, H. Lorenz-Wirzba and C. Rolfs, **Z. Physik A-Atoms and Nuclei** 298 (1980) 65-75.

30 A. M. Nathan, A. M. Sandrofi, T. J. Bowles, **Phys. Rev. C** 24(1981) 932.

31 W. E. Burcham, **Nuclear Physics**, Longman, London 1979.

32 D. G. Sargood and G. D. Putt, **Aust. J. Phys.** 18 (1965) 491-6.

33 Nagarajen M. A. and Banerjee M. K., **Communs. Congr. Intern. Physique Nucleaire**, Paris, p.506 (1959).

34 G. R. Harrison, G. D. Schmidt and C. D. Curtis, **Phys. Rev.** 117 (1960) 532.

35 M. K. Juric, **Physica** 22 (1956) 1154.

36 J. P. F. Sellschop, **Ph.D. Thesis**, University of Cambridge 1957.